RIG-I agonists as effective anti-viral prophylaxis and treatment in a mouse model of severe SARS-CoV-2 infection

Doctoral thesis

to obtain a doctorate (PhD)

from the Faculty of Medicine

of the University of Bonn

Samira Alina Marx
from Frankfurt am Main, Germany
2022

Written with authorization of

the Faculty of Medicine of the University of Bonn

First reviewer: Prof. Dr. med. Gunther Hartmann

Second reviewer: Prof. Dr. Stefan Bauer

Day of oral examination: 14.06.2022

From the Institute of Clinical Chemistry and Clinical Pharmacology

Director: Prof. Dr. med. Gunther Hartmann

Table of contents

List of abbreviations

Abbreviation	Full name
3pRNA	5’ triphosphate short uncapped dsRNA (RIG-I agonist)
7-methylguanylate cap	7mG cap
ACE2	angiotensin- converting enzyme II
AIM2	absent in melanoma 2
AM	alveolar macrophage
ANOVA	Analysis of Variance
APC	antigen-presenting cells
ARDS	acute respiratory distress syndrome
ATP	adenosine triphosphate
BMDC	bone-marrow derived dendritic cells
bp	base pair
CARD	caspase activation and recruitment domains
CCL	CC chemokine ligand
CCR	CC chemokine receptor
CD	Cluster of differentiation
cGAS	cyclic GMP-AMP synthase
COVID-19	coronavirus disease 2019
CpG	deoxycytidyl-phosphate-deoxyguanosine
CTD	C-terminal domain
ctrl	control
CXCL	CXC chemokine ligand
CXCR	CXC chemokine receptor
DAMP	damage-associated molecular patterns
DC	dendritic cell
DDX58	DExD/H-box helicase 58
DMEM	Dulbecco’s Modified Eagle's Medium
DMV	double-membrane vesicle
DNA	Deoxyribonucleic acid
dpi	days post infection
dsRNA	double-stranded RNA
ELISA	enzyme-linked immunosorbent assay
ER	endoplasmatic reticulum
ERGIC	endoplasmatic reticulum- Golgi intermediate compartment
FCS	Fetal bovine serum
FSC	forward scatter
GAPDH	glyceraldehyde-3-phosphate dehydrogenase
hpi	hours post infection
hrs	hours
i.n.	intranasal
i.v.	intravenous
IAV	Influenza A virus
IFIH1	interferon induced with helicase C domain 1
IFN	interferon
IFNAR	IFNα/β receptor
IFNLR	IFNλ receptor

IgG	immunoglobulin G
IKKε	inhibitor of NF-κB kinase epsilon
IL	interleukin
IM	interstitial macrophage
IRF	Interferon regulatory factor
ISG	interferon-stimulated genes
ISGF3	interferon-stimulated response element-3
ISRE	IFN-stimulated response elements
IκB	Inhibitor of κB
JAK1	Janus kinase 1
kb	kilobases
LGP2	laboratory of genetics and physiology 2
MAVS	mitochondrial antiviral signaling protein
MDA5	melanoma differentiation associated gene 5
MERS	Middle East respiratory syndrome
MHC	major histocompatibility complex
MOI	Multiplicity of infection
mRNA	Messenger RNA
MX1	MX dynamin like GTPase 1
NEMO	NF-Kappa-B essential modulator
NeutraLISA	Neutralization linked immunosorbent assay
NF-κB	nuclear factor kappa-light-chain-enhancer of activated B cells
NK cell	Natural killer cell
NLR	NOD-like receptors
NOD	nucleotide-binding oligomerization domain
NSAID	nonsteroidal anti-inflammatory drug
nsp	Non-structural proteins
ORF	Open reading frames
PAMP	pathogen-associated molecular patterns
PBMCs	peripheral blood mononuclear cell
PD1	programmed cell death protein 1
PDL-1	Programmed death-ligand 1
PEG	Polyethylenglycol
PEI	polyethyleneimine
PFU	plaque-forming unit
PRR	pattern recognition receptors
qPCR	quantitative polymerase chain reaction
RD	repressor domain
RdRp	RNA-dependent RNA polymerase
RIG-I	Retinoic acid inducible gene-I
RLR	RIG-I-like receptor
RNA	Ribonucleic acid
RPMI	Roswell Park Memorial Institute (medium)
RSAD2	radical S-adenosyl methionine domain containing 2
RSV	Respiratory Syncytial Virus
RTC	replication and transcription complex
SARS	severe acute respiratory syndrome
SARS-CoV-2	severe acute respiratory syndrome coronavirus 2

SD	standard deviation
SEM	standard error of the mean
siRNA	small interfering RNA
SSC	side scatter
ssRNA	single-stranded RNA
STAT	signal transducer and activator of transcription
STING	stimulator of interferon genes
TBK1	TANK-binding kinase 1
TLR	Toll-like receptor
TMPRSS2	Transmembrane protease, serine 2
TNF	Tumor necrosis factor
TRIM25	Tripartite motif-containing protein 25
TYK2	Non-receptor tyrosine-protein kinase
Unc93b	Unc-93 homolog B1
UTR	untranslated region
WHO	World Health Organization
WT	wild-type

1. Introduction

Emerging and re-emerging viral infections as currently presented with the severe acute respiratory syndrome coronavirus 2 (SARS-CoV-2) pandemic pose a major threat for global health and economics. Despite the fact that vaccinations are most effective in controlling coronavirus disease 2019 (COVID-19) spread, frequent vaccine breakthrough infections and the emergence of new vaccine-escape variants highlight the importance of effective therapeutic interventions to treat COVID-19 patients and to contain this pandemic. As of now, therapeutic treatments mainly rely on the repurposing of small-molecule anti-viral drugs restricting viral replication with only moderate efficacy.

Detection and clearance of viruses and pathogens are mediated by different layers of a strong and highly sophisticated host defense system, the immune system. Central for the immune detection of virus-infected cells is the sensing of viral nucleic acids by innate immune receptors present in the cytosol and the endolysosomal compartments. Engagement of these receptors culminates in the establishment of a robust early cellular anti-viral resistance and of subsequent efficient anti-viral immune responses leading to the clearance of the infection. Targeted activation of innate immune receptors by synthetic ligands has been shown to induce anti-viral cellular resistance and to boost immune responses even in the absence of an infection, and thus may be employed independently of the genetic background of a virus. Conclusively, in contrast to ‘classical’ anti-viral agents that interfere with essential proteins in the life cycle of a given virus, this potent pharmacological intervention may serve as a novel broad-spectrum anti-viral approach that would allow for its rapid application to constrain the spread of newly emerging viruses in the future.

1.1. A short introduction into the immune system

1.1.1. Innate immunity

The first line of defense against pathogens consists of predetermined mechanisms of innate immunity. The innate immune system is an evolutionary ancient system that is found in vertebrates, invertebrates and even in plants (Jones and Dangl, 2006; Nyholm and Graf, 2012). Several layers of innate immunity mainly serve as a barrier to prevent pathogen entry and as a first immune response to counteract the pathogen. Natural

barriers include the anatomical compositions of the skin and epithelial surfaces, the production of antimicrobial proteins, mucus, surfactant or saliva and low pH in the stomach rendering the barrier sites almost impermeable for the pathogen (Chaplin, 2010). Moreover, the proteolytic cascade of proteins of the complement system in the plasma mediates inflammation by opsonizing pathogens for the degradation by phagocytes, triggering direct cytolysis of the pathogen, neutralizing immune complexes and by chemotaxis (Dunkelberger and Song, 2010). The cellular arm of innate immunity includes effector cells, such as natural killer (NK) cells, granulocytes (neutrophils, basophils, eosinophils) and phagocytic cells (myeloid cells: macrophages, dendritic cells (DCs)). Macrophages are abundantly present in tissues and are specialized in the recognition of microorganisms and (e.g., complement-coated) particles resulting in their subsequent rapid phagocytosis and lysosomal degradation. Together with DCs, they form the group of professional antigen-presenting cells (APCs), since they can present antigens derived from the engulfed pathogen on their surface to the effector cells of the second arm of immunity, the adaptive system. This interaction enables the crucial crosstalk between the innate and adaptive immune system as discussed below (Bonilla and Oettgen, 2010; Chaplin, 2010).

Central for innate immune recognition on a single cell level is the expression of the germline-encoded pattern recognition receptors (PRRs) (Janeway and Medzhitov, 2002). Their activation is typically triggered by molecules indicating microbial infections and culminates in the induction of an innate immune response. Since PRRs can be expressed by both immune cells and somatic cells, almost every cell is equipped to sense infections and to initiate an immune response. PRRs have distinct expression patterns, cellular localizations, ligand specificities and unique but converging downstream signaling cascades leading to the secretion of cytokines. Microbial molecules that are recognized by a given PRR are called pathogen-associated molecular patterns (PAMPs). They typically comprise of microbe-specific structural components that are highly conserved and essential for microbial propagation (e.g. carbohydrates, peptides, peptidoglycans and lipoproteins) or microbial nucleic acids (Janeway and Medzhitov, 2002). Furthermore, endogenous molecules that are released or re-localized from a damaged cell can trigger PRRs as well and thereby serve as stress/danger signals leading to non-infectious

inflammation. These so-called damage-associated molecular patterns (DAMPs) are for example uric acid crystals and extracellular ATP (Vénéreau et al., 2015). The engagement of a PRR with its cognate ligand triggers the secretion of inflammatory cytokines including type I interferons (IFNs) and chemokines and/or antimicrobial peptides that recruit and activate immune cells, alarm the neighboring cells, have antimicrobial activities and mediate the activation and maturation of the APCs (Janeway and Medzhitov, 2002).

1.1.2. Adaptive immunity

While the innate immune system acts immediately with pre-existing mechanisms, adaptive immunity mainly relies on the recognition of specific antigens and is characterized by high specificity and adaptability by generating highly effective *de novo* responses against pathogens (Janeway and Medzhitov, 2002). However, it requires more time to develop than innate immunity. After clearance of infection, the developed adaptive response persists as a long-lasting immunological memory allowing for faster, stronger and more effective immune responses upon re-exposure to the same pathogen.

Adaptive immune cells include T and B lymphocytes that are generated in the thymus and bone marrow, respectively, and mainly reside in secondary lymphoid organs namely lymph nodes and spleen in their naïve states (Bonilla and Oettgen, 2010). Matured APCs migrate to the draining lymph node and present the previously encountered antigens to naïve T and B cells. Naïve T cells require three signals from the APC to get fully activated (Goral, 2011): First, the interaction of the antigen-specific T cell receptor and the cognate antigen presented on the APC leads to the initial activation of the T cell; second, co-stimulatory signals (CD28/CD80 or CD86) are required for clonal expansion and maintain peripheral tolerance; and third, cytokines mediate the proliferation and differentiation into specific subtypes of effector cells. For B cell activation, the interaction of its B cell receptor with the antigen presented on the APC and co-stimulatory signals from T cells are needed (Goral, 2011).

Since every adaptive immune cell expresses a unique antigen-specific receptor, only the interaction with the cognate T and B cell leads to its activation and clonal expansion inducing a specific adaptive immune response. The activated, differentiated and clonally expanded effector cell then migrates to the site of infection and exerts its functions. T cells represent the cellular arm of adaptive immunity and eliminate infected and transformed

cells directly via cytotoxic killing mechanisms (cytotoxic T cells) or indirectly by activating macrophages and B cells (helper T cells). B cells are the main cells of the humoral adaptive immune response by producing antibodies against the presented to neutralize the pathogen (Bonilla and Oettgen, 2010).

1.2. Nucleic acid recognition by innate immunity

As mentioned before, immune recognition of nucleic acids by PRRs plays a key role in the defense against invading intracellular pathogens and viruses. The self- vs. non-self-discrimination of nucleic acids is a major challenge for the immune system, since nucleic acids are universal from viruses over plants to vertebrates with minimal occurrence of species-/pathogen-specific characteristics. Self-recognition may have detrimental effects on the host resulting in autoimmunity and autoinflammation (Marshak-Rothstein, 2006). Several strategies have evolved that prevent self-recognition under steady-state conditions and determine the favored immune sensing of foreign or altered self over endogenous nucleic acids by innate nucleic acid sensors; including ligand structure, localization and local concentration (Bartok and Hartmann, 2020). Via posttranscriptional modifications, endogenous nucleic acids are marked as self to circumvent aberrant immune activation. Distinct patterns in microbial nucleic acids that are absent or suppressed in host nucleic acids further render immune specificity against non-self nucleic acids and prevent immune self-recognition by PRRs. For example, while species-specific unmethylated deoxycytidyl-phosphate-deoxyguanosine (CpG) dinucleotide motifs are predominantly found in prokaryotic DNA and induce strong immune activation, CpG-rich sequences in mammalian DNA are non-immunostimulatory owing to lower frequency as well as to methylation and inhibitory motifs within its DNA (Bauer et al., 2001; Hemmi et al., 2000; Stacey et al., 2003). Moreover, compartmentalization of nucleic acid sensors to the endolysosomal compartments and the cytosol minimizes the contact to host nucleic acids, as host nucleic acids are exclusively located in the nucleus and cytosol. Constitutively active nucleases prevent the accumulation of potentially stimulatory nucleic acids in- and outside of the cell keeping them below a threshold limit under physiological conditions (Bartok and Hartmann, 2020). However, accumulation of viral nucleic acids in the cytosol upon viral infection exceeds this threshold and thus can trigger PRR stimulation.

The group of nucleic acid immune sensors includes several members of the Toll-like receptor (TLR) family, the RIG-I-like receptors (RLRs), members of the NOD-like receptors (NLRs), the cyclic GMP-AMP synthase (cGAS)-stimulator of interferon genes (STING) axis and the absent in melanoma 2 (AIM2) inflammasome (Bartok and Hartmann, 2020). Since this study focusses on RIG-I and its anti-viral potency against viral infections, RLR signaling will be introduced in more detail in the next sections.

1.2.1. RIG-I like receptors

Members of the RLR family are specialized in recognizing viral RNA intermediates that accumulate in the cytosol leading to the induction of strong anti-viral innate immune responses (Yoneyama et al., 2004). The family comprises three members: Retinoic acid inducible gene-I (RIG-I), melanoma differentiation associated gene 5 (MDA5) and laboratory of genetics and physiology 2 (LGP2) (Bartok and Hartmann, 2020). These cytosolic PRRs are broadly expressed in almost every somatic cell and induce a potent type I IFN-mediated response to a variety of viruses. Usually expressed at low levels in a resting state, these receptors are highly induced upon viral infections or IFN stimulation (Kang et al., 2004; Yoneyama et al., 2004, 2005). Structurally, all three RLR members contain a highly conserved central DExD/H box helicase domain with ATPase activity and a C-terminal repressor domain (RD) within the C-terminal domain (CTD) that is involved in autoregulation (**Figure 1, Figure 2**) (Rehwinkel and Gack, 2020). RIG-I and MDA5 further share two N-terminal caspase activation and recruitment domains (CARDs) in tandem that are required for downstream signaling and are missing in LGP2 (Jiang et al., 2011; Kowalinski et al., 2011; Luo et al., 2011; Yoneyama et al., 2005).

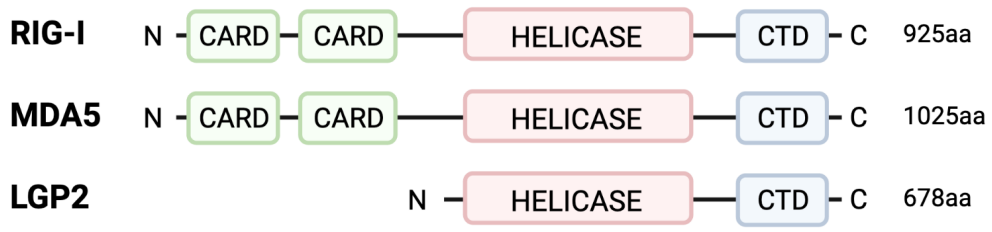

Figure 1: Schematic domain organization of RLRs. All three members comprise a conserved helicase domain with ATPase activity and a C-terminal domain (CTD) with auto-inhibitory capacity. RIG-I and MDA5 further share two N-terminal caspase activation and recruitment (CARD) domains enabling downstream signaling with mitochondrial antiviral-signaling protein (MAVS). On the right side the length of the RLRs is shown in number of amino acids (aa).

RIG-I has been identified to detect negative-strand RNA viruses such as *orthomyxoviridae* (Influenza A viruses (IAV)), *pneumoviridae* (Respiratory Syncytial Virus (RSV)), *paramyxoviridae* (Sendai Virus) and *rhabdoviridae* (Vesicular Stomatitis Virus) (Kato et al., 2005; Loo et al., 2008; Yoneyama et al., 2005) as well as to detect RNA polymerase III-derived transcripts of DNA viruses (Ablasser et al., 2009; Chiu et al., 2009). Several groups have already deciphered the structural minimal motif required to activate RIG-I: RIG-I ligands are typically composed of short blunt-end 5‘ triphosphate uncapped double-stranded RNA (dsRNA) with a panhandle structure (Hornung et al., 2006; Pichlmair et al., 2006; Schlee et al., 2009). dsRNA with 5’ diphosphate ends, as found in reoviral genomes, is also sufficient to activate RIG-I increasing the number of viruses detected by RIG-I (Goubau et al., 2015). To evade aberrant RIG-I stimulation, additional posttranscriptional backbone modifications of the host endogenous mRNA are required to be marked as ‘self’. Most prominently, all vertebrate mRNAs carry a 5’ triphosphate-linked 7-methylguanylate cap (7mG cap) that is required for translation initiation and mRNA stability. Contrary to initial beliefs (Hornung et al., 2006), the 7mG cap alone does not prevent RNA recognition by RIG-I, yet the cap1-specific 2’O-methylation at the N1 position sterically hinders the binding of host mRNA to RIG-I and thus efficiently prevents recognition of eukaryotic mRNA (Devarkar et al., 2016; Schuberth-Wagner et al., 2015). Nonetheless, viruses have evolved several strategies to circumvent RLR recognition by mimicking host mRNA. For instance, expression of the coronaviral non-structural proteins nsp14 and nsp16 enable 5’ capping and 2’O-methylation of viral RNA, thereby mimicking host mRNA (Chen et al., 2009; Menachery et al., 2014; Schuberth-Wagner et al., 2015).

MDA5 is a cytosolic receptor that senses high molecular weight long dsRNA independently of its terminal moieties in a length-dependent manner (Kato et al., 2008). It has been shown to detect *picornaviridae* such as the Encephalomyocarditis Virus (Kato et al., 2005, 2006). Overlapping recognition by RIG-I and MDA5 has been demonstrated for *flaviviridae* (e.g. Japanese Encephalitis Virus or Dengue Virus) and reoviruses (Kato et al., 2006, 2008; Loo et al., 2008). The optimal dsRNA length ranges from 1-7 kilobases (kb) that exceeds the typical length of endogenous dsRNAs (Kato et al., 2008). The binding is rather mediated by the cooperative interaction of MDA5 with the stem region of

long dsRNA species than by specific sequence requirements (Berke and Modis, 2012; Peisley et al., 2011, 2012; Pichlmair et al., 2009; Wu et al., 2013).
In spite of homologies to RIG-I and MDA5 and of high binding affinities to dsRNA, the lack of CARD domains in LGP2 required for the interaction with the mitochondrial antiviral signaling protein (MAVS) hinders the initiation of downstream signaling upon activation (Rothenfusser et al., 2005; Takahasi et al., 2009). LGP2 serves as a negative regulator for RIG-I by sequestering viral dsRNA, inhibiting oligomerization and preventing ubiquitylation of RIG-I (Quicke et al., 2019; Rothenfusser et al., 2005; Saito et al., 2007; Yoneyama et al., 2005). However, LGP2 has also been shown to enhance MDA5-mediated anti-viral immune responses. For instance, mice lacking LGP2 are more susceptible to Encephalomyocarditis virus infections, a virus recognized by MDA5 rather than by RIG-I (Kato et al., 2006; Venkataraman et al., 2007). Moreover, LGP2 facilitates MDA5 signaling by increasing MDA5/RNA interactions (Bruns et al., 2014; Uchikawa et al., 2016).

Of all RLRs, the mechanism of RIG-I signaling on a single-protein level is best understood (**Figure 2**). Without a ligand present, the monomeric RIG-I molecule is in an auto-repressed state in which the C-terminal RD masks the CARD domains (‘closed’ conformation, autoinhibition) (Rehwinkel and Gack, 2020; Saito et al., 2007). Upon binding of the cognate dsRNA to the CTD, conformational changes lead to the release and exposure of the CARDs and of the helicase domain for ATP binding (‘open’ conformation) (Kowalinski et al., 2011). This enables the interaction with the ubiquitin ligase TRIM25 in an ATPase-dependent manner and triggers the subsequent K63-linked polyubiquitylation inducing the activated state of the RIG-I molecule. Immune signaling is mediated by the oligomerization of RIG-I molecules with the CARD-containing adaptor protein MAVS via homotypic CARD-CARD interactions (Hou et al., 2011; Rehwinkel and Gack, 2020). For MDA5, the cooperative binding of long dsRNA with MDA5 serves as a scaffold to facilitate the assembly of several MDA5 molecules into long polymers and to expose the CARD domains to MAVS (Berke and Modis, 2012; Peisley et al., 2011, 2012). Since MAVS is associated with mitochondrial and peroxisomal membranes (Dixit et al., 2010; Seth et al., 2005), the RIG-I/MAVS or MDA5/MAVS complex is re-located to these organelles and the oligomerization of MAVS provides a signaling scaffold for the recruitment of downstream

signaling molecules of two different branches. Phosphorylation of the transcription factors interferon regulator factor (IRF)-3 and IRF-7 by the TANK-binding kinase 1 (TBK1) and the inhibitor of NF-κB kinase epsilon (IKKε) leads to their activation and nuclear translocation culminating in the production of type I and III IFNs (Paz et al., 2006; Rehwinkel and Gack, 2020; Yoneyama et al., 2004). In addition, via the activation of the IKKα/β/NEMO complex, the proteasomal degradation of IκB releases NF-κB and enables its nuclear translocation resulting in the induction of pro-inflammatory cytokines (Bartok and Hartmann, 2020).

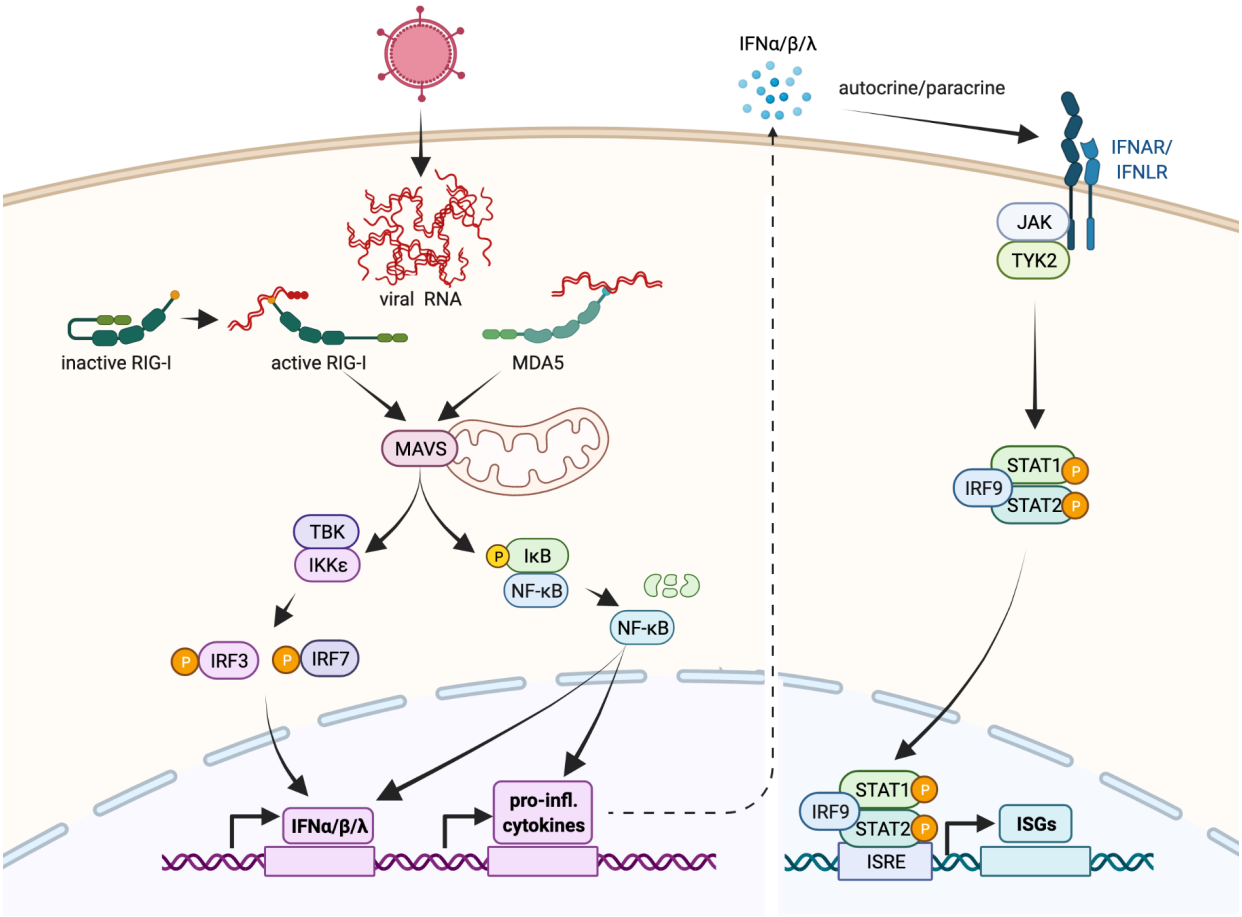

Figure 2: RLR signaling leads to the induction of IFNs and IFN-stimulated genes. Viral dsRNAs of different length are recognized by RIG-I and MDA5 in the cytosol, leading to the oligomerization with MAVS. Eventually, signaling cascades result in the nuclear translocation of IRF-3, IRF-7 and NF-κB, inducing type I and III IFNs as well as pro-inflammatory cytokines. Via autocrine or paracrine action, IFN signaling leads to the induction of several IFN-stimulated genes (ISGs) and cytokines establishing an anti-viral state in the cell.

1.2.2. RLR-induced cytokine responses

Engagement of RIG-I and MDA5 leads to the activation of IRFs and NF-κB resulting in the induction of two anti-viral programs characterized by the release of distinct cytokines. Since these molecules can act on the cell itself (autocrine action), on neighboring cells (paracrine action) or on distant cells (endocrine action), they are crucially involved in the induction, shaping and regulation of innate and adaptive immune responses both in the local environment and systemically.

The first line of anti-viral immunity is mediated by the induction of type I and III IFNs. These multifunctional cytokines account for the establishment of a powerful cell-intrinsic state of viral resistance by upregulating hundreds of anti-viral proteins called interferon-stimulated genes (ISGs) (Schneider et al., 2014). Type I IFNs include IFNβ and 14 closely related isotypes of IFNα (Weerd and Nguyen, 2012). Once synthesized and secreted, all isotypes of type I IFNs bind to a common receptor, the ubiquitously expressed heterodimer IFNα/β receptor (IFNAR1/2). Type III IFNs that include IFNλ1 to IFNλ4 are non-redundant to type I IFNs and bind to the heterodimeric receptor IFNLR1/IL10R2 that is mainly expressed at epithelial barrier sites (Lazear et al., 2015; Weerd and Nguyen, 2012). Despite engaging distinct receptors, both type I and III IFNs have a common signal transduction cascade and induce overlapping sets of genes. Heterodimerization of the IFNAR or the IFNLR renders the activation of the associated Janus protein tyrosine kinases TYK2 and JAK1 that concert the phosphorylation of signal transducer and activator of transcription (STAT) 1 and 2 (**Figure 2**) (Kotenko et al., 2003; Weerd and Nguyen, 2012). Phosphorylated STAT1 and STAT2 together with IRF9 form the heterotrimeric transcription factor complex ISGF3 which translocates to the nucleus and binds to IFN-stimulated response elements (ISREs) resulting in the induction of hundreds of ISGs. The establishment of an anti-viral state by ISG induction mainly results in the inhibition of viral spread by interfering with different stages of the virus life cycle by targeting viral transcription, translation or replication, but also in the apoptosis induction of the infected cell (Schneider et al., 2014). In a positive feedback loop, many of the molecules that have initially driven the IFN signaling cascade (e.g. PRRs, IRFs, members of the JAK-STAT pathway) are themselves regulated by IFNs allowing the amplification of these pathways in the virus-infected cell (Schneider et al., 2014). Via paracrine actions and owing to the ubiquitous expression of IFNAR1/2, the anti-viral state is also established

in neighboring not-yet infected cells. In addition, since immune cells are highly responsive to IFNs, IFN signaling is involved in the enhancement of both innate and adaptive immunity as well (González-Navajas et al., 2012; Weerd and Nguyen, 2012). This includes the improvement of antigen presentation and maturation of APCs, the production of chemokines and cytokines, maturation of B cells and the direct or indirect activation of other immune cells including NK and T cells.

Type I IFNs belong to the first line of defense and induce a great panel of ISGs that peaks early upon infection, however rapidly declines due to negative feedback mechanisms (Bolen et al., 2014; Kohli et al., 2012; Marcello et al., 2006). Meanwhile, type III IFN signaling appears to be the first-line defense against viral infections at barrier sites (Davidson et al., 2016; Galani et al., 2017). Additionally, while both type I and III IFNs limit viral replication in the lungs, only type III IFNs confer protection in the upper respiratory tract (Klinkhammer et al., 2018). Type III IFN responses are generally of lower magnitude and potency compared to type I IFNs and the ISGs induced are a subset of those induced by type I IFNs. Yet, type III IFNs are less inflammatory and thus confer less collateral tissue damage (Crotta et al., 2013; Galani et al., 2017; Lazear et al., 2015; Marcello et al., 2006; Zhou et al., 2007).

As mentioned before, the strong induction of type I IFNs by both somatic and immune cells increases the resistance of uninfected cells towards the viral infection and directly modulates NK cell activity and activates APCs as well. These cells then rapidly secrete pro-inflammatory cytokines and shape the subsequent innate and adaptive immune response forming the second arm of the innate anti-viral immune response (Chaplin, 2010; Vivier et al., 2008). Besides induced as a second wave upon type I IFN signaling, RLR activation results in the production of pro-inflammatory cytokines as well (Bartok and Hartmann, 2020). Via different JAK-STAT signaling pathways, binding of the cytokine to its receptor leads to the cell-intrinsic synthesis of new cellular proteins (Chaplin, 2010). Their main functions include orchestrating cell proliferation, survival, activation and differentiation processes (Fajgenbaum and June, 2020). Multiple cytokines are induced upon viral infections. Among them, IFNγ produced by NK cells and macrophages enhances the anti-viral functions of CD8+ T cells and is involved in shaping the anti-viral response of helper T cells (Vivier et al., 2008). IL-6 has pleiotropic pro- and anti-

inflammatory effects including the differentiation of naïve helper T cells that act on the maturation of B cells, but can cause substantial tissue damage as well (Hunter and Jones, 2015). Chemokines are crucially involved in attracting immune cells to the site of infection and inflammation, in mediating homeostatic migration of lymphocytes and in enhancing immune effector cell functions (Ward et al., 1998). For example, while some chemokine receptors are expressed in naïve T cells orchestrating development and differentiation processes, the induction of certain chemokine receptors upon T cell activation enables the recruitment of the T cell towards the chemokine gradient to the site of infection in a spatiotemporal fashion (Ward et al., 1998). Chemokines are mainly produced by immune cells, fibroblasts, epithelial or endothelial cells in response to pathogens or damage. One of the most important chemokines in the anti-viral response against respiratory tract infections is the IFN-inducible chemokine CXCL10 that binds to CXCR3 present on activated T cells (Lindell et al., 2008; Loetscher et al., 1996). Additionally, virus-specific induction of key chemokines including CXCL8, CCL2, CCL3 and CCL5 leads to the rapid recruitment of neutrophils, macrophages and monocytes to the infected site (Bonville et al., 1999; Dawson et al., 2000; Haeberle et al., 2001; Henriquez et al., 2015).

While pro-inflammatory cytokines and IFNs are predominantly beneficial for the host to fight against viral infections, their dysregulation may have detrimental effects. For instance, mutations in nucleic acid sensing molecules and downstream signaling molecules are associated with several autoimmune diseases and type I interferonopathies that are characterized by a strong inflammatory signature and collateral tissue damage (González-Navajas et al., 2012; Rodero and Crow, 2016). Additionally, the sustained or unbalanced production of pro-inflammatory cytokines often propagates an increased inflammation-associated cytokine secretion and immune cell recruitment, commonly characterized as *cytokine storm*, further driving immunopathology that is seen upon viral infections or in autoimmune diseases (Fajgenbaum and June, 2020; Tisoncik et al., 2012). Thus, a tight regulation of RLR signaling and cytokine responses is required to keep tissue homeostasis and reduce tissue immunopathology.

1.2.3. Clinical potential of RIG-I agonists

Synthetic agonists of nucleic-acid sensing PRRs have been discussed as therapeutic targets for several years (Junt and Barchet, 2015; Yong and Luo, 2018a). Among them, RIG-I is particularly suitable as therapeutic target owing to the defined minimal activating motif, the production of potent agonists by solid phase synthesis (Goldeck et al., 2014) and its ubiquitous expression in nucleated cells including tumor cells. RIG-I agonists have been tested in tumor mouse models (Engel et al., 2017; Jiang et al., 2019; Poeck et al., 2008) and in phase I/II clinical studies against solid tumors (NCT03739138, NCT0306502)(Middleton et al., 2018). While conferring direct anti-tumoral effects via intrinsic or extrinsic apoptosis and inflammasome-induced pyroptosis, its activation also induces IFN-I-mediated activation of innate and adaptive immunity and potent NK cell responses further driving the antitumoral immune response (Besch et al., 2009; Daßler-Plenker et al., 2019; Elion and Cook, 2018; Poeck et al., 2008). Besides its application in tumor immunotherapy, systemic administration of RIG-I agonists shows high efficacy in protecting mice from lethal IAV infections as well, that is not seen by the activation of endolysosomal nucleic acid sensors (Chiang et al., 2015; Coch et al., 2017; Goulet et al., 2013). Its potency is mainly attributed to the RIG-I induced antiviral program that exceeds the response induced by administration of recombinant type I IFN alone (Goulet et al., 2013). Conclusively, specific RIG-I agonists may be a suitable strategy as broadband pan-antiviral agents and vaccine adjuvants against emerging viral outbreaks. Additionally, bifunctional double-stranded siRNAs enabling both the activation of RIG-I and the silencing of a specific gene have already been tested in tumor and virus infection models and highlight a novel possibility to further increase anti-viral activity of immunostimulatory RNA (Ebert et al., 2011; Lin et al., 2012; Poeck et al., 2008).

1.3. SARS-CoV-2

1.3.1. SARS-CoV-2 biology

The recent COVID-19 outbreak is caused by the novel SARS-CoV-2 virus that was first detected in Wuhan, China in December 2019 and rapidly spread world-wide (Zhou et al., 2020b). The World Health Organization (WHO) has declared the COVID-19 outbreak a pandemic on March 11th 2020. As of January 2022, more than 364 million confirmed cases

and over 5.63 million SARS-CoV-2 related deaths worldwide have been reported (https://COVID19.who.int/, status: 28 January 2022).

Endemic human coronaviruses are circulating for years and cause only mild to moderate respiratory symptoms of a 'common cold' with a seasonal pattern (Kesheh et al., 2021). In contrast, the ongoing pandemic is preceded by two coronaviral epidemics of zoonotic origins with high case fatality rates, namely SARS in 2002/2003 (Drosten et al., 2003) and Middle East respiratory syndrome (MERS) since 2012 (Cui et al., 2019; Zaki et al., 2012). All three viruses belong to the group of *beta-coronaviridae*, are enveloped positive-sense single-stranded RNA (ssRNA) viruses exclusively infecting mammalian species and lead to the frequent development of lower respiratory tract infections with poor clinical outcomes in individuals of advanced age and with comorbidities (Hartenian et al., 2020; Renu et al., 2020). With a genome size of approx. 30 kb, they belong to the largest of all RNA viruses. At the 5' end, the open reading frames ORF1a and ORF1b encode for 16 nonstructural proteins that are required for RNA replication, followed by ORFs encoding for the structural proteins spike (S), envelope (E), membrane (M) and nucleocapsid (N) that are required for building the viral membrane and encoding for accessory proteins involved in immune evasion (**Figure 3**) (Hartenian et al., 2020).

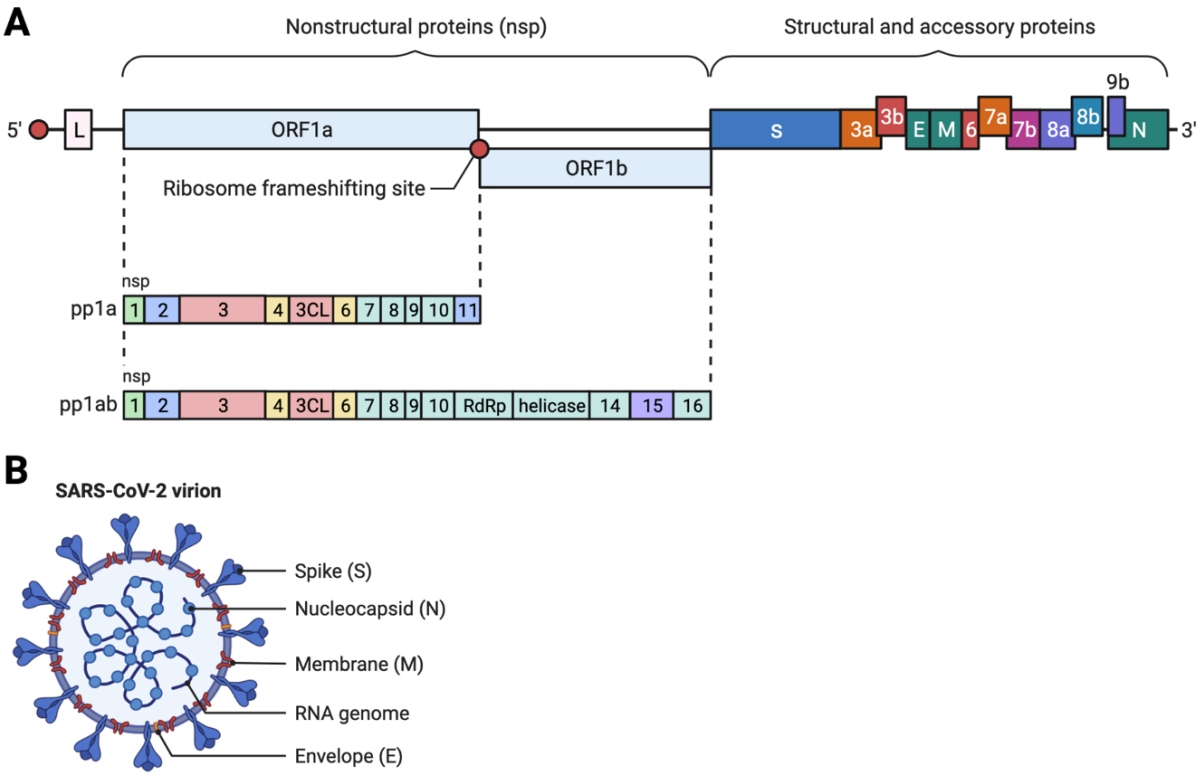

Figure 3: Genome and virion organization of SARS-CoV-2. (A) Two ORFs at the 5' end of the RNA genome encode 15 nonstructural proteins (nsps) required for viral replication, followed by ORFs encoding for structural and accessory proteins. (B) Schematic presentation of the SARS-CoV-2 virion. Modified from (Hartenian et al., 2020).

Cell entry of SARS-CoV-2 requires binding of the viral spike protein to the human cell surface receptor angiotensin-converting enzyme II (ACE2), an important enzyme involved in maintaining fluid and salt balance as well as blood pressure homeostasis (Gheblawi et al., 2020). ACE2 is widely expressed in human organs with most abundant expression in the intestinal tract, the upper respiratory tract, the kidneys, and the male reproductive tract (Hikmet et al., 2020). Upon binding to ACE2, the viral spike protein is cleaved and activated by the host serine protease TMPRSS2 (Hartenian et al., 2020; Hoffmann et al., 2020). This leads to the fusion with the plasma membrane and the SARS-CoV-2 virus enters the cell via endocytosis and releases its content into the cytosol (**Figure 4**, step 1). Immediate translation and proteolytic processing of the open reading frames ORF1a and ORF1b leads to the expression of non-structural proteins that form the viral replication and transcription complexes (RTCs) (**Figure 4**, steps 2 and 3). These RTCs are compartmentalized in double-membrane vesicles (DMVs) derived from the endoplasmatic reticulum (ER) membrane preventing the recognition of viral RNA and its intermediates by innate nucleic acid sensors in the cytosol (Snijder et al., 2020; Stertz et al., 2007). The RTC mediates both the RNA replication of genomic RNA as well as the transcription of subgenomic RNA for subsequent translation (Hartenian et al., 2020): First, the RNA-dependent RNA polymerase (RdRp) initiates the synthesis of full-length negative-sense genomic RNA that is used as a template for the synthesis of full-length positive-sense RNA (**Figure 4**, step 4). Secondly, discontinuous transcription from the full-length positive-sense RNA enables the production of subgenomic mRNA that subsequently can be translated to viral structural and accessory proteins (**Figure 4,** steps 5 and 6). Protein synthesis finally leads to the assembly and packaging of new virions that are eventually secreted from the infected cell via exocytosis (**Figure 4**, steps 7 to 9) (Hartenian et al., 2020).

Since the initial discovery of SARS-CoV-2, several viral variants of concern variant have emerged with increased transmissibility and pathogenicity compared to the initial virus

owing to mutations in the spike protein that enhance its binding affinity to ACE2 (Kumar et al., 2021; Mistry et al., 2022).

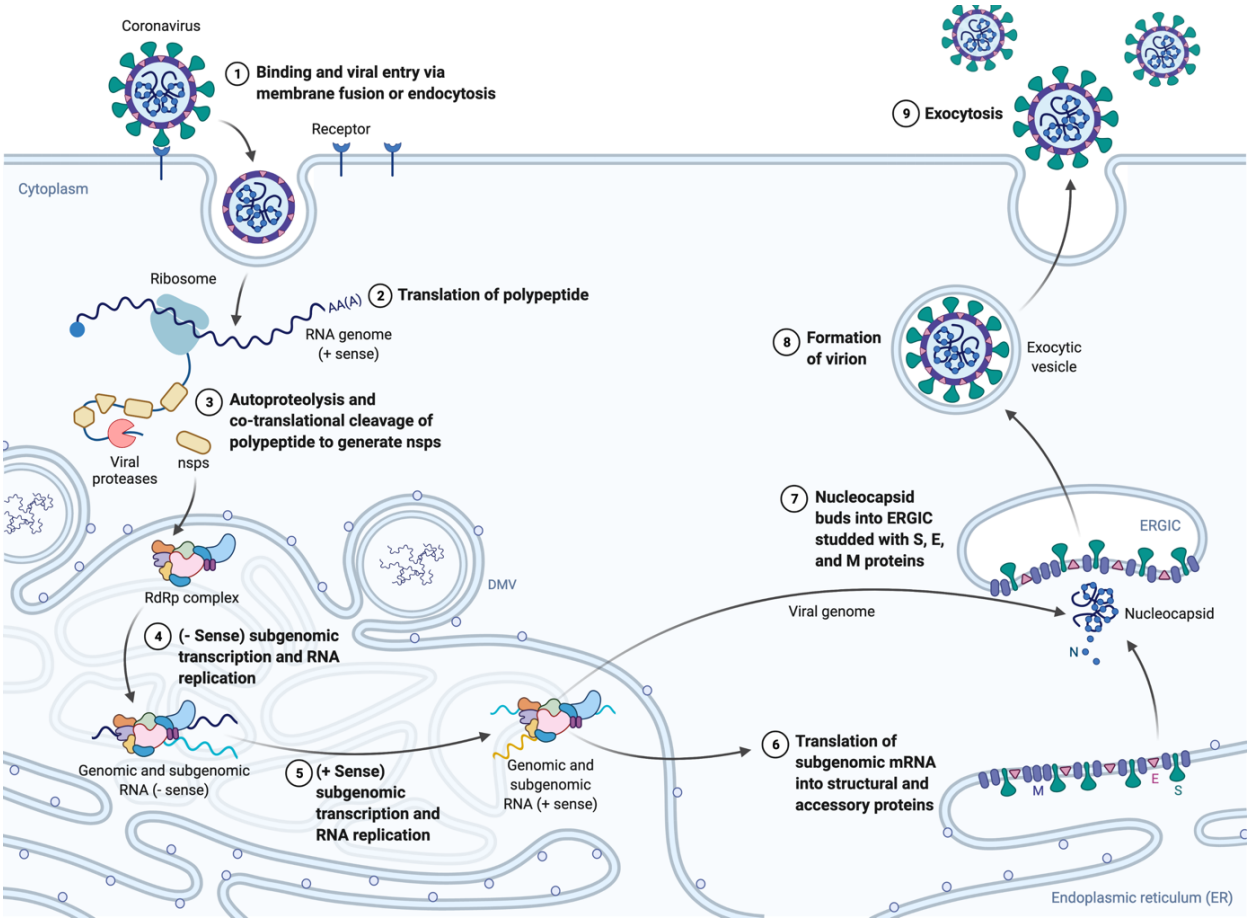

Figure 4: Life cycle of SARS-CoV-2. Engagement of the SARS-CoV-2 spike protein with host ACE2 and TMPRSS2 leads to viral entry and the release of their RNA genome into the host cytoplasm (1). Translation of the viral polypeptide (2) and proteolytic processing generates nsps for the assembly of the RdRp complex (3). The RdRp complex located in DMVs synthesizes (-) sense genomic and subgenomic RNA that in turn are used as a template for the synthesis of (+) sense full-length and subgenomic mRNAs (4+5). The subgenomic RNAs are translated into structural and accessory proteins (6) and new viral virions are assembled (7+8) and exocytosed (9). ERGIC = endoplasmatic reticulum- Golgi intermediate compartment. The figure is modified from (Hartenian et al., 2020).

1.3.2. COVID-19 disease

COVID-19 causes both upper and lower respiratory tract infections with a variety of symptoms and heterogeneous disease severity. In the majority of cases, SARS-CoV-2-infected individuals experience fever, coughing, shortness of breath and fatigue for several days, but infection can also manifest in extrapulmonary organs (Gupta et al., 2020;

Huang et al., 2020; Zhou et al., 2020b). Around 35 % of SARS-CoV-2 infections are reportedly asymptomatic, with higher proportions among children and individuals with no underlying comorbidities (Sah et al., 2021). Both asymptomatic and symptomatic COVID-19 patients mount a highly effective immune response against SARS-CoV-2 as shown by high neutralizing anti-SARS-CoV-2 IgG antibody titers (Le Bert et al., 2021; Long et al., 2020). Despite the fact that most SARS-CoV-2-infected patients are presented with mild symptoms and infection largely remains restricted to the upper respiratory tract, around 14 % of patients require hospitalization due to the development of a severe respiratory disease of the lower respiratory tract and 5 % of patients have developed critical illness with progressive respiratory failure (Wu and McGoogan, 2020). One of the major causes for systemic multi-organ failure and COVID-19-related death has been shown to be severe lung damage upon the progression of viral pneumonia to the acute respiratory distress syndrome (ARDS) (Grasselli et al., 2020; Huang et al., 2020; Tian et al., 2020; Xu et al., 2020). Furthermore, thrombotic complications contribute to severe COVID-19 disease and are associated with poor outcome (Bikdeli et al., 2020). Indeed, post-mortem histological examination of lungs of SARS-CoV-2 patients reveals the presence of diffuse alveolar damage, accumulation of mononuclear immune infiltrates and substantial fibrin deposition in pulmonary microvasculature, indicating the presence of ARDS with high similarities to hallmarks of interstitial pulmonary fibrosis (Tian et al., 2020; Wendisch et al., 2021). Advanced age, immunosuppressive conditions and comorbidities such as diabetes, obesity, hypertension, pulmonary or heart disease are associated with altered expression and functions of ACE2 (Gheblawi et al., 2020) and are identified as risk factors for developing critical COVID-19 (Elezkurtaj et al., 2021; Wu and McGoogan, 2020).

Although recovered from the active infection, many SARS-CoV-2 patients continue to experience at least one long-term symptom summarized as *post-COVID-19 syndrome*. Most common symptoms are fatigue, headache, respiratory symptoms, attention disorder, hair loss and dyspnea that last from weeks to months after recovery (Lopez-Leon et al., 2021; Sanchez-Ramirez et al., 2021). Notably, the majority of people has been healthy prior to infection and has shown only mild COVID-19 symptoms (Spudich and Nath, 2022). The underlying mechanism for these symptoms is still largely unknown.

1.3.3. Imbalanced host immune responses contribute to SARS-CoV-2 pathology

In spite of predominantly mild COVID-19 courses, some individuals develop severe COVID-19 disease without prior at-risk medical indications. This heterogeneity of COVID-19 manifestation highlights the requirement for a deeper knowledge about the host-virus interactions including viral entry and viral immune evasion as well as the subsequent host immune responses. Coronaviruses including SARS-CoV-2 have evolved several strategies to evade host antiviral responses. For instance, they replicate within DMVs to circumvent RLR recognition (Snijder et al., 2020; Stertz et al., 2007). Expression of several non-structural and accessory proteins also allow for immune evasion of SARS-CoV-2 by inhibiting RLR signaling (e.g., nsp3, nsp5, N, M), mimicking host mRNA (e.g., nsp14, nsp16) and antagonizing type I IFN signaling at various steps (e.g. nsp1, nsp5, ORF6) (Beyer and Forero, 2021; Lei et al., 2020; Schuberth-Wagner et al., 2015; Wang et al., 2020b).

Analogous to SARS and MERS (Cameron et al., 2007; Channappanavar et al., 2016, 2019), severe COVID-19 disease has been associated with a dysregulated host immune response. In the early stage of infection, the majority of later-critically infected COVID-19 patients have presented mild symptoms that have worsened in the later stages of disease or in the process of recovery. The rapid development of ARDS and multi-organ failure often results in death within a short time. The time line of disease aggravation suggests that the key driver of disease is not the viral infection itself, but the failure to mount a regulated host immune response causing immunopathology (**Figure 5**).

As mentioned before, central for a potent anti-viral defense is the induction of IFNs and the initial establishment of an anti-viral state that interferes with viral replication. In line with this, severely SARS-CoV-2-infected patients are presented with a highly impaired type I IFN response as indicated by the low or delayed type I IFN production and the limited induction of ISGs which is in contrast to common respiratory viral infections (Blanco-Melo et al., 2020; Hadjadj et al., 2020). Underlining the critical role of nucleic acid sensors and IFNs for controlling SARS-CoV-2 infections, genetic analysis of fatally infected SARS-CoV-2 patients reveals a higher risk for individuals with missense mutations in molecules involved in nucleic acid sensor signaling (*TLR3*, *UNC93B*, *IRF7*) or IFN signaling (*TYK2, OAS* and *IFNAR2*) (Pairo-Castineira et al., 2021; Zhang et al., 2020b). Conclusively, the early IFN response against SARS-CoV-2 infection seems to be

critical for the establishment of a potent anti-viral innate and adaptive immune response and viral clearance. Furthermore, neutralizing autoantibodies against type I IFNs are detected in >10 % of critically ill SARS-CoV-2 patients, while being absent in patients with mild or asymptomatic disease (Bastard et al., 2020).

Dysregulation of the early IFN response is characterized by a strong induction of chemokines and cytokines (Blanco-Melo et al., 2020; Hadjadj et al., 2020) that likely aggravates the disease development and tissue pathology, even after the active viral infection has been cleared. Critically ill COVID-19 patients experience a stronger and prolonged pro-inflammatory cytokine and chemokine response than patients with mild or moderate disease (Mulchandani et al., 2021; Zhou et al., 2020a). Elevated levels of the monocyte chemoattractants CCL2 and CCL8 as well as of the neutrophil chemoattractant IL-8 indicate the recruitment of these immune cells to the lungs, which may contribute to tissue damage and further exacerbate the increased cytokine production (Blanco-Melo et al., 2020). This is supported by studies reporting a significantly higher blood neutrophil-to-lymphocyte ratio and lymphopenia in severely infected COVID-19 patients (Chen et al., 2020; Zhang et al., 2020a). Moreover, the presence of high IL-6, IL-8, IL-10, TNFα and CXCL10 serum levels correlate with poor disease progression and outcome (Huang et al., 2020; Laing et al., 2020; Liu et al., 2020; Mulchandani et al., 2021). The excessive inflammation, the recruitment of macrophages and neutrophils together with endothelial activation and injury mainly drives the immunothrombosis observed in severely-infected COVID-19 patients (Shaw et al., 2021; Wendisch et al., 2021).

Collectively, the lack or delayed onset of a robust early type I IFN response is likely responsible for high viral titers observed in SARS-CoV-2 infected patients. The subsequent hypercytokinemia is proposed to be a significant contributor to COVID-19-related ARDS and mortality. Thus, key to combat SARS-CoV-2 infections appears to be the fine-tuning of the early IFN response limiting both the viral spread and the subsequent hyperinflammation.

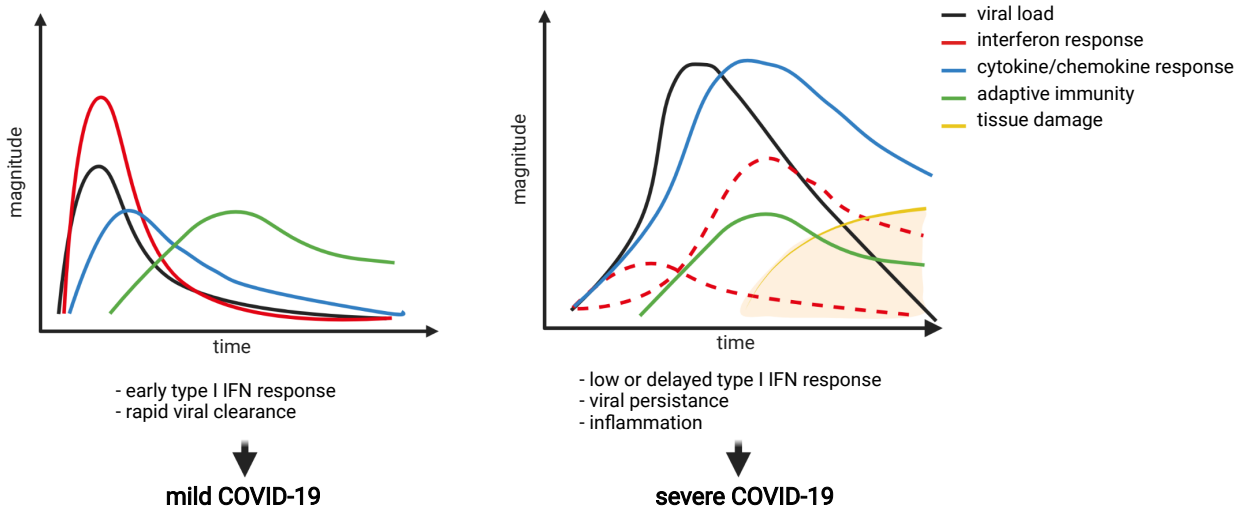

Figure 5: Schematic relationship of SARS-CoV-2 disease development with immune response. Mild COVID-19 disease is associated with a robust type I and III IFN response and a moderate cytokine/chemokine induction leading to the efficient clearance of viral infection and the establishment of adaptive immunity. In contrast, severely ill COVID-19 patients lack a robust IFN response, but show a strong, dysregulated cytokine/chemokine response causing hyperinflammation and tissue damage.

1.3.4. Current COVID-19 vaccines and treatment options

Tremendous efforts have been made in the development of vaccines against SARS-CoV-2 to limit viral transmission, prevent symptomatic infections and eventually reach herd immunity to allow the transition from a pandemic to an endemic. So far, multiple vaccines aiming to generate neutralizing antibodies against the SARS-CoV-2 spike protein have been approved and show high protection in the overall population against hospitalization and death (Dagan et al., 2021; Haas et al., 2021; Mistry et al., 2022). However, vaccine breakthrough infections are frequent, the limited availability of vaccines in some areas reduces the potential of the indirect protection mediated by herd immunity and immunocompromised individuals may not get full protection upon vaccination. Additionally, newly emerged SARS-CoV-2 viral variants, including the delta (B.1.617.2) and omicron (B.1.1.529) variant, have shown increased immune evasion (Collie et al., 2021; Mistry et al., 2022; Saban et al., 2022). They have already been shown to moderately reducing vaccine efficacies in the prevention of infection, albeit remaining high in the prevention of severe disease and death (Collie et al., 2021; Mistry et al., 2022; Saban et al., 2022). This is likely owing to the increased occurrence of genomic alterations in the viral spike coding regions (Kumar et al., 2021; Mistry et al., 2022). Hence, the

development of effective anti-viral drugs that have a broad therapeutic spectrum against viruses is crucial to fill the niche of missing therapeutics against newly emerging viruses, until effective virus-specific therapies become available, as currently seen with SARS-CoV-2.

So far, standard care of COVID-19 patients mainly includes the treatment of associated symptoms. For instance, administration of glucocorticoids, like dexamethasone and hydrocortisone, appears to be moderately beneficial to reduce hyperinflammation in hospitalized severely ill COVID-19 patients (Angus et al., 2020; RECOVERY Collaborative Group et al., 2021). Anti-coagulant drugs are administered to hospitalized at-risk COVID-19 patients to prevent thrombotic events and multi-organ failure (Bradbury and McQuilten, 2022; Shaw et al., 2021).

Until now, only a limited number of anti-viral drugs is available for the treatment of COVID-19 infection and mainly target essential mechanisms in the life cycle of a virus. Early research in drug repurposing has helped to identify potential therapeutics against SARS-CoV-2. For example, the high conservation poses the viral RdRp as a promising broad-band treatment target against several RNA viruses including SARS-CoV-2. The RdRp inhibitor remdesivir (Veklury®) shorten the time of recovery of hospitalized COVID-19 patients (Beigel et al., 2020), yet the intravenous injection limits its administration to hospitalized patients. In contrast, the orally active low-cost RdRp inhibitor molnupiravir allows for the treatment of non-hospitalized at high-risk COVID-19 patients. In a phase III clinical study, early intervention with molnupiravir (Lagevrio®) has significantly reduced the risk for hospitalization and death in at-risk COVID-19 patients by 50 % (Jayk Bernal et al., 2021). Recently, a 5-day treatment regimen early upon symptom onset with the 3CL protease inhibitor nirmatrelvir/ritonavir (Paxlovid®) has been reported to reduce the risk of hospitalization or death even by 89 % (Mahase, 2021). However, major limitation of these selective drugs is the potential emergence of mutations in the targeted viral protein that may compromise the treatment efficacy.

1.3.5. Available mouse models for studying SARS-CoV-2 infections

Animal models including mice, hamsters, non-human primates and ferrets are used to investigate the pathogenesis of SARS-CoV-2 infections and to evaluate therapeutic countermeasures and vaccines against COVID-19 (Muñoz-Fontela et al., 2020). Yet, none

of them completely recapitulate the course of COVID-19 disease in humans (Muñoz-Fontela et al., 2020). Main limitation of mouse models is the low binding affinity between the SARS-CoV-2 spike protein and the murine ACE2 protein (Zhou et al., 2020b) that render WT mice naturally not susceptible to SARS-CoV-2 infections (Bao et al., 2020; Oladunni et al., 2020). Hence, mouse models require either the adaptation of the SARS-CoV-2 virus to mice or the transgenic introduction of human ACE2 mice to be permissive to SARS-CoV-2 infections (Muñoz-Fontela et al., 2020). Most common transgenic mouse models include the expression of human ACE2 under the control of a tissue-specific promoter or of the endogenous mouse *Ace2* promoter as well as by adenoviral transduction (Muñoz-Fontela et al., 2020).

The K18-hACE2 transgenic mouse model is one of the most used laboratory animal models so far for evaluating medical countermeasures against COVID-19. Initially generated to investigate SARS-CoV infections, human ACE2 is introduced under the control of the murine *Cytokeratin-18* promotor leading to supraphysiological expression of *ACE2* in the lungs and gastro-intestinal tract, and lower expression in the brain, small intestines, spleen, kidney, liver and heart (McCray et al., 2007; Perlman and McCray). They are reportedly highly susceptible to the intranasal (i.n.) inoculation with SARS-CoV-2 virus leading to the development of a severe respiratory disease with high viral lung titers, pulmonary inflammation, significant weight loss and anosmia that resemble key symptoms of human COVID-19 disease (Winkler et al., 2020; Yinda et al., 2021; Zheng et al., 2021). Other transgenic mouse models rely on the insertion of *ACE2* under control of the endogenous murine *Ace*2 promoter (Bao et al., 2020; Winkler et al., 2021). This leads to more physiological expression patterns and levels of *ACE2* with high expression in nasal turbinates and lung and low expression in extra-pulmonary organs (Sun et al., 2020; Zhou et al., 2021). Infection with SARS-CoV-2 induces a mild sublethal disease in these mice presented by a modest weight loss and limited lung inflammation as well as by high viral titers that are restricted to the lungs (Bao et al., 2020; Israelow et al., 2020; Winkler et al., 2021). Adenoviral transduction of *ACE2* further enables the investigating SARS-CoV-2 in mice with diverse genetic backgrounds in relatively short time (Israelow et al., 2020).

1.4. Aim of the study

The novel coronavirus SARS-CoV-2 emerged in late 2019 and led to the ongoing COVID-19 pandemic with substantial consequences for daily life and economies worldwide. COVID-19 disease ranges from mild symptoms to severe lower respiratory tract infections. Dysregulation of the early type I IFN response and a subsequent exaggerated immune responses to SARS-CoV-2 infection are associated with the progression to severe COVID-19 manifestation. Therefore, the induction of an early anti-viral immune response via immunostimulatory agents may be a promising approach to provide anti-viral protection against SARS-CoV-2. Targeted stimulation of the cytosolic RNA sensor RIG-I induces a strong type I IFN response that should provide immediate cellular resistance against SARS-CoV-2 infection and support the development of a sustained adaptive antiviral immune response. The broad expression of RIG-I enables almost all nucleated cells to sense viral infection and to induce an antiviral state in neighboring cells via type I IFN production. Antiviral protection conferred by RIG-I ligands has already been extensively studied in IAV mouse models (Chiang et al., 2015; Coch et al., 2017; Goulet et al., 2013). Therefore, the early intervention with RIG-I ligands may be a suitable treatment option to prevent serious COVID-19 disease. Due to the host-based approach, RIG-I stimulation may serve as a rapidly applicable and broadly-active prophylactic against emerging viruses, until virus-specific therapies and vaccines become available.

In this study, the anti-viral potency of RIG-I agonists against SARS-CoV-2 is evaluated and compared to the potency of recombinant type I IFN *in vitro* and *in vivo*. Furthermore, the immediate effects of RIG-I stimulation on lung tissue is examined *in vivo* and the prophylactic and therapeutic efficacy of systemic, selective RIG-I activation is explored in a severe mouse model of SARS-CoV-2 infection in regards to disease development and survival, the viral burden and inflammation in the lungs and brain as well as to the induction of subsequent adaptive anti-viral immunity.

2. Material and Methods

2.1. Materials

2.1.1. Consumables

Name	Company
1 ml syringes Injekt-F	B. Braun Melsungen AG
1.5 and 2 ml reaction tubes	Greiner Bio-One
15 and 50 ml falcons	Greiner Bio-One
384-well qPCR plate, laser marked	BIOplastics
5, 10 and 25 ml disposable pipettes	Corning
96-well Half Area Clear Flat Bottom Polystyrene High Bind Microplate	Corning
96-well High Binding Standard ELISA Microplates	Greiner Bio-One
96U-well plate	Greiner Bio-One
Cell counting slides for TC20™	Bio-Rad
Cell culture flasks T25, T75 and T175	Sarstedt
Cell culture plates (6,12,24,96F-well)	TPP
Cell strainer 70 µm	Sarstedt
Ceramic spheres (Ø 6,35 mm)	MP Biomedicals
Microlance cannula 27G 3/4 0,4x19 mm	VWR
Microlance cannula 30G 0,3x13 mm	VWR
OneComp eBeads	Life Technologies
sterile filter 0.22 µm	Labomedic
Tips (10 µl, 200 µl, 1000 µl)	Mettler Toledo
UTM® 360C oral swabs with UTM	Coran
VWR® SuperClear™ Screw Cap Microcentrifuge Tubes	VWR
Zirconia pellets (Ø2 mm)	BioSpec

Table 1: List of consumables used in this study.

2.1.2. Media and buffers for cell culture

Buffer	Company	Order number
0,05 % trypsin/EDTA	Thermo Fisher Scientific	25300096
1 M HEPES	Thermo Fisher Scientific	15630056
100 mM Sodium Pyruvate	Thermo Fisher Scientific	11360088
200 mM L-Glutamine	Thermo Fisher Scientific	25030123
DMEM (high glucose)	Thermo Fisher Scientific	41965062
Fetal Bovine Serum (FCS)	Thermo Fisher Scientific	10270106
NaCl 0.9 %	B. Braun Melsungen AG	3570160
non-essential amino acids	Thermo Fisher Scientific	11-140-050
OptiMEM® I Serum reduced medium	Thermo Fisher Scientific	31985047
Penicillin-Streptomycin (10,000 U/mL)	Thermo Fisher Scientific	15140122
Phosphate buffered Saline (PBS)	Thermo Fisher Scientific	14190169
RPMI 1640 (+L-glutamine)	Thermo Fisher Scientific	21875091
Trypsin, TPCK-treated	Sigma-Aldrich	4370285-1KT
Water Ampuwa	Fresenius Kabi	30201763

Table 2: Media and buffers for cell culture used in this study.

2.1.3. Kits and enzymes

Kit/enzyme	Company	Order number
5x EvaGreen QPCR-Mix II (ROX)	Biobudget	80-5820000
Anti-mouse IFNα, Rabbit Serum	PBL Assay Science	32100-1
Polyclonal Goat anti-rabbit antibody (Biotin)	Dako	E0432
Anti-SARS-CoV-2-QuantiVac-ELISA (IgG)	Euroimmun	EI 2s606-9601-10 G
Collagenase	Sigma-Aldrich	C5138
Dako REAL™ Detection System, Alkaline Phosphatase	Agilent Technologies	K500511-2
DNase I, RNase-free	Thermo Fisher Scientific	EN0521
goat anti-rabbit IgG-HRP conjugate	Bio-Rad	170-6515
Human IFNα ELISA	Life Technologies GmbH	BMS216
LEGENDplex™ Mouse Anti-Virus Response Panel (13-plex)	BioLegend	740622
Murine IFNα coating antibody	PBL Assay Science	#22100-1
normal goat serum (10 %)	Thermo Fisher Scientific	50062Z
NucleoSpin RNA Virus, Mini kit for viral RNA from cell-free fluids	Macherey-Nagel	740956.50
Rabbit SARS-CoV-2 nucleocapsid antibody	Biozol	SIN-40143-R019
RevertAID reverse transcriptase	Thermo Fisher Scientific	EP0442
RiboLock	Thermo Fisher Scientific	EO0382
SARS-CoV-2 Antigen ELISA	Euroimmun	EQ 2606-9601
SARS-CoV-2 NeutraLISA	Euroimmun	EI 2606-9601-4

Table 3: Kits and enzymes used in this study.

2.1.4. Chemicals and Reagents

Reagent	Company	Order number
10X Reaction Buffer with MgCl2 for DNase I	Thermo Fisher Scientific	B43
2-Propanol ≥99,5 %	Carl Roth	9866.6
37 % Formalin solution	Carl Roth	4979.1
BD Pharm lyse solution	Becton Dickinson	5559899
Chloroform	Carl Roth	3313.1
dNTP kit	Carl Roth	K039.2
Ethanol, Ph.Eur., ≥99,5 % pure	Carl Roth	5054.4
Ficoll-Paque Plus	VWR	17-1440-03
G418 Sulfate	Carl Roth	0239.4
In vivo-JetPEI	Polyplus	201-50G
Lipofectamine 2000	Thermo Fisher Scientific	11668019
Random hexamers	IDT	51-01-18-26
TMB Substrate Reagent Set	Becton Dickinson	555214

TransIT®-LT1 Transfection Reagent	Mirus Bio	MIR2306
TriZOL	Invitrogen	15596018
Tween®20	Carl Roth	9127.1

Table 4: Chemicals and Reagents used in this study.

2.1.5. Machines

Name	Company
AperioSlideScanner	Leica Biosystems
Attune NXT	ThermoFisherScientific
Centrifuge 5430	Eppendorf
Centrifuge 5810R	Eppendorf
Epoch Microplate Spectrophotometer	BioTek Instruments
FastPrep™-24 Classic	MP Biologicals
CO_2 Incubator	PHC Holdings Corporation
Invert phase contrast microscope DMi1	Leica Biosystems
NanoDrop 8000	ThermoFisherScientific
TC20® Automated Cell counter	Bio-Rad
Thermocycler PeqSTAR	VWR Peqlab
Thermomixer® C	Eppendorf

Table 5: Machines used in this study.

2.1.6. Programs

Name	Company
Prism 9	GraphPad
Office 16	Microsoft
Legendplex Data Analysis Software	Biolegend
NanoDrop 8000 Operating Software	ThermoFisherScientific
FlowJo 10.7.1	FlowJo
Mendeley Desktop 1.19.8	Mendeley Ltd.
Aperio Imagescope 12.1	Leica Biosystems
Gen5™ Microplate Reader and Imager Software 2.09	BioTek Instruments

Table 6: Programs used in this study.

2.2. Cell culture

2.2.1. Cell culture

VeroE6 cells were a kind gift from PD Beate Kümmerer (Institute of Virology, University Hospital Bonn) and were cultured in DMEM medium supplemented with 10 % heat-inactivated FCS, 1 mM sodium pyruvate and 100 U/ml Pen/Strep (= complete DMEM). MDCK cells were cultured in RPMI medium supplemented with 10 % heat-inactivated FCS, 2 mM glutamine, 10 mM HEPES and 100 U/ml Pen/Strep. A549 and A549 cells expressing hACE2 and hTMPRSS2 (A549*, kindly provided from Lara Schwab, Institute

of Clinical Chemistry and Clinical Pharmacology, University Hospital Bonn) were cultured in complete DMEM. Cells were cultured according to standard cell culture techniques.

2.2.2. PBMC isolation

PBMCs were purified from heparinized fresh blood of healthy human donors. Blood was carefully pipetted onto a Ficoll layer and centrifuged at 800 x g for 20 min (brake 1, RT). The PBMC layer was collected and washed with NaCl 0.9 % and pelleted at 400 x g for 10 min before erythrocytes were lysed using 5 ml 1x Pharm lyse for 5 min at RT. Reaction was stopped by adding FCS-containing RPMI medium and cells were centrifuged at 400 x g for 10 min. PBMCs were resuspended in RPMI containing 100 U/mL Pen/Strep, non-essential amino acids, sodium pyruvate and 10 % heat-inactivated FCS. Cells were counted with the TC20 automated cell counter and $4x10^5$ cells in 100 µl were seeded in a 96F- well plate to be used for *in vitro* stimulation assays.

2.2.3. Generation of GMCSF- conditioned medium from J55811 cells

J55811 cells were cultured in RPMI medium supplemented with 10 % heat-inactivated FCS; 100 U/ml Pen/Strep; 1 % non-essential amino acids; 2mM L-Glutamine, 1mM sodium pyruvate and 1 mg/ml G418 for selection. For the production of GMCSF, $2x10^6$ J55811 cells plated in a T175 cell culture flask were cultured in 100 ml complete RPMI without G418. After 10 days, supernatant was harvested and sterile-filtered using a 0.22 µM sterile filter.

2.2.4. Murine BMDC generation

Bone marrow of naïve C57BL6/j WT, RIG-I$^{-/-}$ and MDA5$^{-/-}$ mice was used as a primary source of murine DCs. Mice were euthanized by cervical dislocation, femurs and tibias were separated and surrounding muscle tissue was removed. Under sterile conditions, the intact bones were cut at both ends and bone marrow was flushed with PBS using a 27 G 3/4 cannula. Cells were centrifuged at 300 x g for 5 min, before resuspended in 2 ml 1x Pharm lyse for 5 min at RT. Erythrocyte lysis was stopped by adding 10 ml FCS-containing RPMI medium followed by a 2nd centrifugation step for 5 min at 300 x g at RT. The cell pellet was resuspended in RPMI medium supplemented with 10 % heat-inactivated FCS, 1x non-essential amino acids, 100 U/ml Pen/Strep and 3 % J55811

conditioned medium. $10x10^6$ primary cells per 10 cm tissue culture dish were seeded and allowed to differentiate for 6 days. On day 4, 2/3 of the medium was gently replaced with fresh medium containing GM-CSF, while the non-adherent cells were pelleted and returned to culture as well. For harvesting cells on day 6, cells were washed twice with PBS, before incubated with 2 mM EDTA in PBS for 15 min at 37 °C to detach the adherent cells. Afterwards, remaining adherent cells were dislodged by gently tapping and gentle pipetting up and down. Harvested cells were seeded at $2x10^5$ cells per 96F-well plate in 100 µl of RPMI medium supplemented with 10 % heat-inactivated FCS, 1x non-essential amino acids, 100 U/ml Pen/Strep.

2.2.5. 3pRNA synthesis

Synthetic 3pRNA with a published sequence (3pGFP2) (Wang et al., 2010) was chemically synthesized by solid-phase synthesis as described before (Goldeck et al., 2014). Control RNA (CA21, 5'-CACACACACACACACACACAC-3') was synthesized by Biomers (Ulm, Germany).

2.2.6. *In vitro* cytosolic transfection with RNA

Human PBMCs and murine BMDCs were stimulated in duplicates with total RNA or oligonucleotides (100 ng/ 96-well) complexed to 0.25 µl Lipofectamine 2000 in 25 µl OptiMEM according to the manufacturer's instructions. 100 ng p(I:C) was complexed to 0.3 µl TransIT®-LT1 in 25 µl OptiMEM. Supernatants were collected 18-24 h after transfection.

A549* cells were stimulated in 24-well plates ($1.5x10^5$ cells in 500 µl) with 200 ng/ml 3pRNA or control RNA complexed to 1 µl/ml Lipofectamine 2000 in 50 µl OptiMEM according to the manufacturer's instructions. Universal human recombinant IFNα(A/D) was used at 10^4 U/ml. Supernatants were taken 16-24 h after stimulation.
All experiments were repeated at least three times and data of mean values are shown in the figures.

2.2.7. Virus stocks

The SARS-CoV-2 virus stock was kindly provided by PD Beate Kümmerer (Institute of Virology, Bonn) and was isolated from a throat swab isolate of a SARS-CoV-2-infected patient at the University of Bonn, Germany in March 2020 (SARS-CoV-2/human/Germany/Heinsberg-01/2020). The virus was passaged in VeroE6 cells and the viral titers were determined using a plaque assay as described in (Koenig et al., 2021).

The Influenza A strain A/Perth/265/2009(H1N1) (pdm09, IAV) and the Respiratory Syncytial Virus strain RSV Long virus stock were kindly provided by Lara Schwab (Institute of Clinical Chemistry and Clinical Pharmacology, University Hospital Bonn).

2.2.8. *In vitro* viral infections

80 % confluent VeroE6 cells in T75 flasks were pulse-infected with RSV or SARS-CoV-2 with an MOI of 0.01 in serum-free medium for 1 h at 37 °C with gentle shaking. 80 % confluent MDCK cells were pulse-infected with IAV with an MOI of 0.01 in serum-free medium for 1 h at 37 °C with gentle shaking. After removal of virus inoculum, cells were washed twice with PBS and were incubated in growth medium with 1 % FCS at 37 °C and 5 % CO_2. 0.5 µg/ml TPCK-trypsin was added to the medium of IAV-infected cells to allow multiple rounds of IAV replication. After 6, 12 or 24 h supernatants from SARS-CoV-2 infected cells were discarded and cells were washed twice with PBS, before 5 ml TriZOL was added to lyse the cells for total RNA isolation. RSV- and IAV- challenged cells were incubated only 12 h prior lysis. Mock-treated cells were used as control.

A549* cells plated in 24-well plates ($1.5x10^5$ cells in 500 µl) were pulse-infected with SARS-CoV-2 (MOI of 0.1) in serum-free medium for 1 h at 37 °C. After removal of virus inoculum, cells were washed twice with PBS and were incubated in complete DMEM medium for 24 h. Cells and supernatants were harvested for downstream analysis.

2.3. *In vivo* experiments

2.3.1. Mice

7-16-week-old C57Bl6j mice were purchased from Charles River and kept at in-house facilities in Bonn (Germany) under specified pathogen free (SPF) conditions.

B6.Cg-Tg(K18-ACE2)2Prlmn/J (K18-hACE2) mice were purchased from Jackson Laboratories and bred in-house at the University Hospital Bonn. After genotyping by qPCR, 8-20-week-old K18-hACE2$^{tg/wt}$ mice of both sexes were used for the SARS-CoV-2 infection experiments that were conducted in the mouse Biosafety Level 3 (BSL3) facility at the University Hospital Bonn. All mice were housed in individually ventilated cage (IVC) cages in groups of up to five individuals per cage and maintained on a 12-hour light/dark cycle at 22-25 °C temperature and 40-70 % relative humidity under specific-pathogen free conditions. All mice were fed with regular rodent chow and sterilized water ad libitum. All procedures were performed according to ethical protocols approved by the responsible animal welfare authority (81-02.04.2019.A433, 81-02.04.2021.A267 LANUV NRW).

2.3.2. *In vivo* stimulation

3pRNA or CA21 (20 µg or 6,25 µg as indicated) was complexed to *in vivo*-JetPEI (N/P ratio 6 or 8) according to the manufacturer's instructions. In short, RNA and *in vivo*-JetPEI were prepared separately in 5 % glucose before mixed together and incubated for 15 min at room temperature. Complexes were diluted with 5 % glucose to reach a total injection volume of 100 µl per mouse. Mice were injected intravenously (i.v.) into the tail vein with 100 µl RNA complexes at indicated time points and dosage.

Universal recombinant IFNα (A/D) was administered i.v. at 2x10^5 U /mouse in 100 µl PBS.

2.3.3. *In vivo* infections with SARS-CoV-2 virus

K18-hACE2$^{wt/tg}$ mice were anesthetized with 90 mg/kg Ketamin/ 5 mg/kg Xylazin intraperitoneally and exposed intranasally to 5x10^4 PFU SARS-CoV-2 virus in 40 µl PBS. Mice were watched until woken up from the narcosis.

SARS-CoV-2-infected mice were scored and weighed once to twice a day. Abnormalities in the spontaneous activity and responses to external stimuli were recorded including reduced activity, weakness, lethargy or higher respiratory rates. In the survival experiments, endpoint parameters were weight loss of ≥20 % and signs of lethargy or comparable signs of poor condition and led to the immediate sacrifice by cervical dislocation. Mice that survived the SARS-CoV-2 infection were sacrificed by cervical dislocation on day 13 post infection.

2.3.4. Organ sampling

For lung and brain histopathology, parts of the organ were fixed in 6 % naturally buffered formalin for 48 h before paraffin embedding and sectioning. Lung, brain, spleen, intestine, colon, heart and liver tissue was transferred to 1 ml TriZOL and stored at -80 °C until downstream RNA isolation. Serum was collected from the *vena facialis* at indicated time points for LEGENDplex analysis and ELISA. Lungs, axillary lymph nodes and spleen were collected for flow cytometric analysis.

2.3.5. Oropharyngeal swabs

Oropharyngeal swab material was collected using flexible Minitip flocked swabs. These were gently rubbed in the mouth of infected mice on day 1 to day 3 post infection for approximately 5 seconds and transferred to 1 ml UTM medium. After an incubation time of 30 min at RT, tubes were stored at -80 °C until further analysis.

2.4. Biochemical methods

2.4.1. ELISA and LEGENDplex

Human IFNα ELISA was performed according to the manufacturer's instructions. For the murine IFNα ELISA, 96-well half-area plates were coated overnight with rat anti-mouse IFNα antibody diluted in coating buffer (90 mM Na_2HPO_4, 130 mM NaH_2PO_4, pH 6.5) to a final concentration of 2.5 µg/ml. Cytokine detection was performed with a rabbit anti-mouse IFNα antibody (80 NU/ml final concentration) for 3 h at RT followed by goat anti-rabbit IgG-HRP conjugate (1:5000).

Mouse anti-virus response LEGENDplex analysis was performed according to the manufacturer's instructions. Serum samples were diluted 1:2 or 1:100 and Matrix A was added to the standard as recommended by manufacturer for serum samples. The plates were measured on an Attune NXT flow cytometer and analyzed with the Legendplex software.

Serum of SARS-CoV-2-infected mice was tested for the presence of neutralizing anti-SARS-CoV-2 specific IgG antibodies using the anti-SARS-CoV-2 QuantiVac-ELISA (IgG) and the pseudo antibody neutralization assay (SARS-CoV-2 NeutraLISA). Both ELISAs were performed according to the manufacturer's instructions, with the exception that the anti-human anti-IgG antibody in the QuantiVac-ELISA kit was exchanged for a goat anti-

mouse IgG-HRP conjugate (1:5000). The presence of SARS-CoV-2 specific antigens in oropharyngeal swab material as well as in the supernatants of SARS-CoV-2 challenged A549* cells was tested using the SARS-CoV-2 antigen ELISA according to the manufacturer's instructions.

2.4.2. Immunohistological staining and scoring

Half of the lungs and one mid sagittal cut half of the brain were fixed in 6% neutral buffered formalin for at least 48 h. Tissues were embedded in paraffin. For SARS-CoV-2 antigen immunohistochemistry, slides were incubated with blocking reagent (10% normal goat serum) followed by rabbit monoclonal antibody against SARS-CoV-2 nucleocapsid protein (1:20000). The secondary antibody (polyclonal goat anti-rabbit antibody, Biotin) and the chromogen from the Dako REAL detection system were used for the staining according to the manufacturer's protocol. Tissue sections were visualized using an Aperio SlideScanner CS2 and the Aperio Imagescope 12.4 software. Three scientists scored the sections in a blinded fashion as follows: 0 no staining; 1 weak staining, <5 % brain area or <10 % of lung area; 2 strong staining, 5-33 % brain area or 10-50 % of lung area; 3 strong staining >33 % of brain area or >50 % lung area.

2.4.3. RNA isolation and cDNA synthesis

Organs were homogenized in 1 ml TriZOL reagent with the addition of ceramic beads (4-5x Ø 2 mm beads and 1x Ø 6.35 mm beads) using a bench-top homogenizer (2x 20 sec, 6.5 m/s). RNA was isolated according to the manufacturer's instructions and resuspended in 20-200 µl RNase-free water depending on the size of the pellet. Total cell RNA from cells was isolated using TriZOL (5 ml/T75 flask; 1 ml/24-well) and RNA was resuspended in 20-100 µl RNase-free water. RNA from oropharyngeal swabs was isolated using the NucleoSpin RNA Virus MiniKit according to the manufacturer's protocol. RNA was eluted in 20 µl RNase-free water.

RNA was stored at -80 °C and RNA concentration was measured using a NanoDrop. For cDNA synthesis, 300 ng of RNA was treated with DNase I for 30 min at 37 °C before inactivated by adding EDTA for 10 min at 65 °C. Afterwards, cDNA was prepared in a 10 µl reaction using the supplier's instructions at 42 °C for 1 h followed by heat inactivation at 70 °C for 10 min. cDNA was diluted 1:10 and stored at -20 °C.

2.4.4. Quantitative PCR

The resulting cDNA was used for amplification of genes of interest by qPCR using EvaGreen QPCR-mix II (ROX) in a 10 µl reaction according to the manufacturer's instructions. Target gene expression was calculated using the comparative method for relative quantification upon normalization to *gapdh* gene expression and average values from duplicates were shown as $2^{-\Delta Cq}$. SARS-CoV-2 Spike RNA expression in oropharyngeal swab material was determined using the commercial E.Sarbeco primer sets and presented as mean C_q values for each mouse. All primers were ordered from IDT.

Primer	**Sequence (5' → 3')**
hsACE2 fwd	CAGCTCAGGGGCTTTGGAAT
hsACE2 rev	CGGCGTTCTTCACTCCAGAT
hsCXCL10 fwd	CCACGTGTTGAGATCATTGCT
hsCXCL10 rev	TGCATCGATTTTGCTCCCCT
hsGAPDH fwd	CATCTTCCAGGAGCGAGATCCCC
hsGAPDH rev	TTCAGACCCATGACGAACAT
hsIL6 fwd	GGTACATCCTCGACGGCATCT
hsIL6 rev	GTGCCTCTTTGCTGCTTTCAC
hsMX1 fwd	CAGCTCAGGGGCTTTGGAAT
hsMX1 rev	CGGCGTTCTTCACTCCAGAT
hsRSAD2 fwd	CCTGTCCGCTGGAAAGTGTT
hsRSAD2 rev	GACACTTCTTTGTGGCGCTC
hsTMPRSS2 fwd	TAGGGGATACAAGCTGGGGT
hsTMPRSS2 rev	GGATTAGCCGTCTGCCCTC
mmCCL2 fwd	CAC TCA CCT GCT GCT ACT CA
mmCCL2 rev	GCT TGG TGA CAA AAA CTA CAG C
mmCXCL10 fwd	CCCACGTGTTGAGATCATTGCC
mmCXCL10 rev	GTGTGTGCGTGGCTTCACTC
mmDDX58 fwd	GAA GAT TCT GGA CCC CAC CTA
mmDDX58 rev	TGA ATG TAC TGC ACC TCA
mmGAPDH fwd	CTG CCC AGA ACA TCA TCC CT
mmGAPDH rev	TCA TAC TTG GCA GGT TTC TCC A
mmIL6 fwd	TGTGACATCAAGGACCTGCC
mmIL6 rev	CTGAGTCACCTGCTACACGC
mmRSAD2 fwd	AACCCCCGTGAGTGTCAACTA
mmRSAD2 rev	AACCAGCCTGTTTGAGCAGAA
SARS-CoV-2 E_Sarbeco fwd	ACAGGTACGTTAATAGTTAATAGCGT
SARS-CoV-2 E_Sarbeco rev	ATATTGCAGCAGTACGCACACA

Table 7: Primers used for quantitative qPCR.

2.4.5. FACS analysis

For FACS analysis of organs, spleen and lungs were cut into smaller pieces and digested with collagenase D and DNase I for 15-30 min at 37 °C. Homogenates were filtered through 70 µm cell strainers to get single cell suspensions. Lymph nodes were directly filtered through 70 µm cell strainers. Pharm lysis was performed to get rid of erythrocytes for 5 min at RT. Single cells suspensions were collected in 96U well plates. First, cells were stained with a life/dead marker for 20 min in PBS on ice in the dark. After washing with FACS buffer, surface staining was added in 30 µl FACS buffer/well and incubated for 20 min on ice in the dark. After two washing steps, cells were directly measured in the Attune NXT flow cytometer. Compensation was performed with single staining of OneCompBeads. FACS data were analyzed with FlowJo 10.

Antigen	Fluorochrome	Clone	Company	Dilution
CD11b	BV650	M1/70	Biolegend	1:200
CD19	PE	6D5	Biolegend	1:200
CD25	BV421	PC61	Biolegend	1:200
CD4	PE-Cy7	GK1.5	eBioscience	1:200
CD45	PerCP	30-F11	Biolegend	1:200
CD64	BV421	10.1	Biolegend	1:200
CD69	PE	H1.2F3	Biolegend	1:200
CD69	AF647	H1.2F3	Biolegend	1:200
CD8	FITC	53-6.7	Biolegend	1:200
CD86	BV785	GL-1	Biolegend	1:200
F4/80	FITC	BM8	eBioscience	1:200
Fixable Viability Kit	Zombie Aqua		Biolegend	1:1000
Ly6A/E	BV785	D7	Biolegend	1:200
Ly6C	AF647	HK1.4	Biolegend	1:200
Ly6G	APC-Fire 750	1A8	Biolegend	1:200
NK1.1	BV650	PK136	Biolegend	1:200
PD1	APC-Fire750	29F.1A12	Biolegend	1:200
PDL1	PE-Cy7	10F.9G2	Biolegend	1:200

Table 8: Antibodies used to detect immune cell populations by flow cytometry

2.4.6. Statistical analysis

All statistical tests were calculated using Prism 9. A p-value of <0.05 was considered statistically significant. Survival curves were analyzed using the log rank Mantel-Cox test. Analysis of weight change was determined by two-way analysis of variance (ANOVA). All results were expressed as mean ± SEM and were corrected for multiple comparisons. Data were checked for log-normal distribution with the Shapiro-Wilk test. Log-normally

distributed data was analyzed using a one-way ANOVA or two-way ANOVA and other data was analyzed using a non-parametric Kruskal-Wallis test as indicated in the figure legends.

All graphics were designed on Biorender.com.

3. Results

3.1. Total RNA from SARS-CoV-2-infected cells has low immunostimulatory potential to activate RLR receptors *in vitro*

RIG-I and MDA5 are two potential innate immune receptors that are able to sense the presence of SARS-CoV-2 infection within a cell. The contributions of these cytosolic receptors in other cells than epithelial cells still remain to be determined (Kouwaki et al., 2021; Yin et al., 2021). Several viral proteins of SARS-CoV-2 have been shown to antagonize RLR and IFN signaling at various steps (Beyer and Forero, 2021; Lei et al., 2020; Wang et al., 2020b) that might interfere with the evaluation of the role of these receptors in directly SARS-CoV-2-infected cells. Therefore, in order to more precisely evaluate the role of RIG-I and MDA5 in the innate immune recognition of SARS-CoV-2, total RNA from SARS-CoV-2-infected cells was extracted and transfected into the cytosol of naïve immune cells. Thereby, RIG-I and MDA5 were directly confronted to preformed viral replication intermediates in the absence of the potential viral RLR and IFN antagonists. Total RNA was isolated from VeroE6 cells either 6, 12 and 24 hours (hrs) after SARS-CoV-2 infection or left uninfected and transfected into human peripheral blood mononuclear cells (PBMCs) using Lipofectamine 2000. Longer infection times than 24 hrs led to cytopathic effects (data not shown). To assess the full immunostimulatory potency of SARS-CoV-2 total RNA, immune sensing of SARS-CoV-2 was compared to that of Influenza A virus (IAV) and Respiratory Syncytial virus (RSV), since both present important respiratory viruses but belong to different families (*orthomyxoviridae* and *pneumoviridae*). For this, total RNA extracted from VeroE6 cells infected for 12 hrs with RSV and from MDCK cells infected with IAV for 12 hrs were transfected using Lipofectamine 2000. The production and release of IFNα into the supernatants after overnight incubation was measured as a readout for RLR stimulation.

As shown in **Figure 6**, total RNA from uninfected cells led to negligible IFNα responses in PBMCs, as did RNA from cells infected with SARS-CoV-2 for 6 or 12 hrs, indicating the low presence of RLR agonists in these RNA preparations. Total RNA from 24-hr SARS-CoV-2-infected cells still led to a low, but significantly increased IFNα response, while total RNA from RSV and IAV infected cells induced a high IFNα release in PBMCs. In vitro-transcribed 5’ triphosphate dsRNA (IVT4) served as a positive control for RIG-I stimulation and p(I:C) for MDA5 activation.

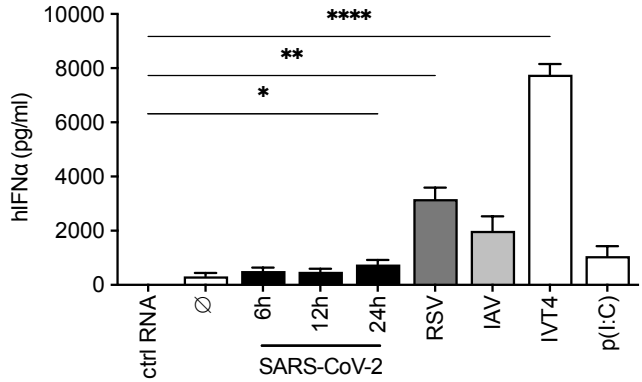

Figure 6: Total RNA of SARS-CoV-2-infected cells results in low type I IFN production in human immune cells. Total RNA was isolated from uninfected (∅), SARS-CoV-2- or RSV-infected VeroE6 cells and from IAV- infected MDCK cells after 12 hrs of infection, if not stated otherwise. RNA was transfected to the cytosol of. After overnight incubation, supernatants were collected and assessed for IFNα production by ELISA. Data are shown as mean + SEM (n=6 donors). Statistical analysis was calculated by one-way ANOVA (Welch) and Dunn's multiple testing. * $p<0.05$, ** $p<0.01$, *** $p<0.001$, **** $p<0.0001$.

Additionally, the immunostimulatory potency of SARS-CoV-2 total RNA was evaluated in murine bone-marrow derived dendritic cells (BMDCs). A crucial advantage of murine over human immune cells is the option to generate BMDCs with different genetic backgrounds to decipher the individual involvement of RIG-I and MDA5 in the immune sensing of viral immunostimulatory RNA. Furthermore, the role of RLRs in the immune sensing of total RNA form virus-infected cells has not been shown before in murine cells, but is important when using mouse models of SARS-CoV-2 infection. Therefore, BMDCs from wild-type (WT), MDA5$^{-/-}$ and RIG-I$^{-/-}$ mice were generated and stimulated with the aforementioned total RNA preparations. Murine IFNα secretion into the supernatants after overnight incubation was used as a readout for RIG-I and MDA5 activation.

Comparable to human PBMCs, total genomic RNA extracted from uninfected cells led to negligible IFNα production in murine BMDCs (**Figure 7A**). The IFNα response to RNA isolated from cells 6 and 12 hrs after SARS-CoV-2 infection was indistinguishable from uninfected total cell RNA, which showed a weak immune activation dependent on MDA5. However, RNA isolated 24 hrs after SARS-CoV-2 infection significantly induced IFNα production when transfected into WT BMDCs (**Figure 7A**). More importantly, recognition was independent of RIG-I and dependent on MDA5 as evidenced by the detectable IFNα levels measured in WT and RIG-I$^{-/-}$ BMDC supernatants that were absent in MDA5$^{-/-}$BMDC

supernatants (**Figure 7B**). In direct comparison, RSV and IAV total genomic cell RNA induced higher immune stimulation than SARS-CoV-2 (**Figure 7A**) and sensing was predominantly dependent on RIG-I, as indicated by the significantly lower IFNα production in RIG-I$^{-/-}$ BMDCs (**Figure 7B**). IVT4 and p(I:C) were used as control stimuli for RIG-I and MDA5, respectively.

Collectively, the RLR-dependent IFNα response to total RNA isolated from SARS-CoV-2-infected cells was completely MDA5-dependent, albeit lower than the – predominantly RIG-I dependent – response to total RNA from IAV or RSV-infected cells.

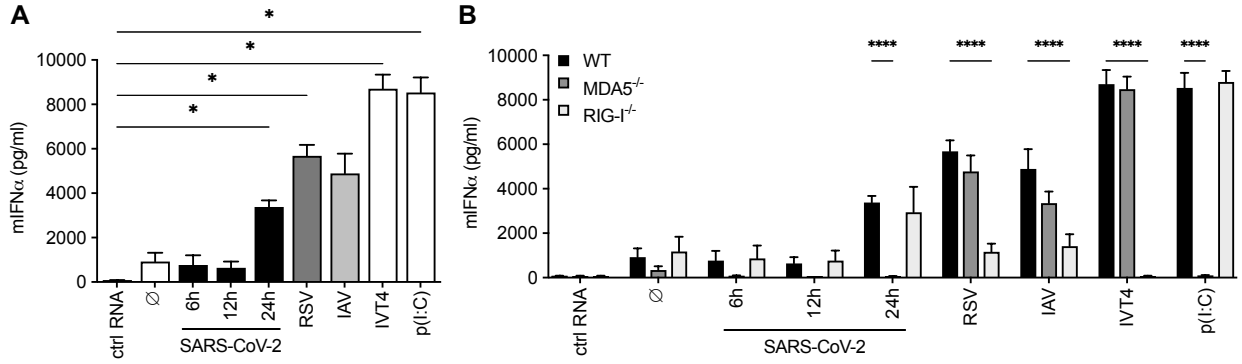

Figure 7: Total RNA of SARS-CoV-2-infected cells activates MDA5 in murine dendritic cells. Total RNA was isolated from uninfected (∅), SARS-CoV-2- and RSV-infected VeroE6 cells and from IAV- infected MDCK cells after 12 hr infection, if not stated otherwise. RNA was transfected to murine BMDCs generated from WT mice (A) or from WT, MDA5$^{-/-}$ and RIG-I$^{-/-}$ mice (B). mIFNα production into the supernatants was measured after overnight incubation by ELISA. Data are shown as mean + SEM (n=3). Statistical significance was calculated by one-way ANOVA (Welch) with Dunn's multiple testing (A) and by two-way ANOVA with Dunnett's multiple testing (B). * $p<0.05$, ** $p<0.01$, *** $p<0.001$, **** $p<0.0001$.

3.2. RIG-I agonists potently inhibit SARS-CoV-2 viral replication *in vitro*

The relatively weak stimulation of RLRs by SARS-CoV-2 total RNA suggested that the pharmacological activation of these receptors by administering selective agonists may help to overcome the limited immune response against SARS-CoV-2 and to reduce viral replication. First, the potency of the RIG-I stimulation by RIG-I agonists on the inhibition of SARS-CoV-2 viral replication was evaluated in SARS-CoV-2-permissive target cells *in vitro*. The commonly used human lung epithelial cell line A549 expressed only low endogenous levels of ACE2 and TMPRRS2 (**Figure 8A**), the two target proteins of the SARS-CoV-2 spike protein required for viral entry into cells. Therefore, plasmids encoding human ACE2 and TMPRSS2 were stably introduced into A549 cells via lentiviral

transduction to allow for stable protein expression and efficient SARS-CoV-2 entry into the cells. High transcript levels of both *ACE2* and *TMPRSS2* in ACE2-TMPRSS2-A549 (A549*) cells were confirmed by qPCR (**Figure 8A**). Subsequently, cells were stimulated with a synthetic RIG-I agonist (5' triphosphate 24 bp long blunt-ended dsRNA, 3pRNA), universal recombinant IFNα(A/D) (IFNα) or ctrl RNA and harvested 6 hrs after stimulation to assess expression of IFN-inducible genes upon efficient RIG-I and IFNAR stimulation. Both 3pRNA and IFNα stimulation led to the strong upregulation of the IFN-inducible anti-viral proteins *MX1* and *RSAD2* and of the IFN-inducible chemokine *CXCL10* in A549* cells (**Figure 8B**). While *MX1* and *RSAD2* transcript levels were comparable between the two treatments, *CXCL10* induction was significantly higher upon 3pRNA treatment compared to IFNα stimulation. Likewise, the pro-inflammatory cytokine *IL6* was significantly induced upon RIG-I ligand stimulation, but only a similar trend, yet non-significant, was observed upon IFNα and ctrl RNA treatment.

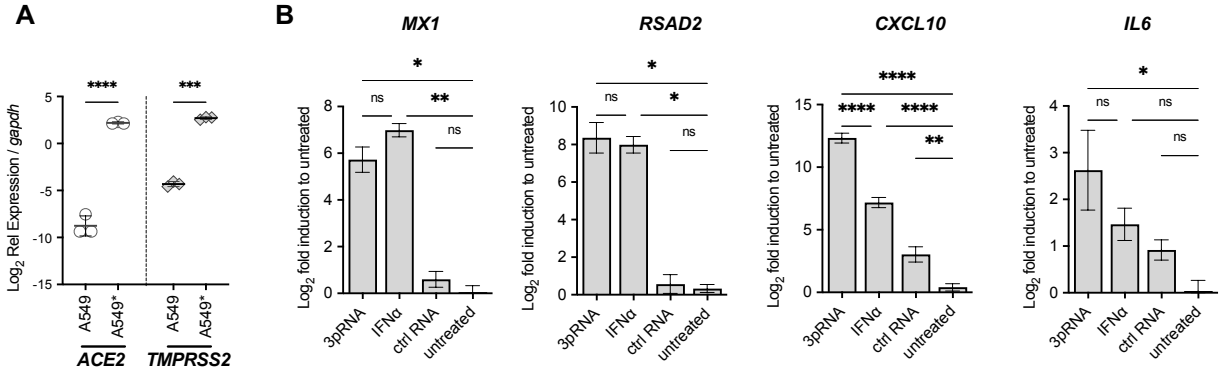

Figure 8: RIG-I and IFNα stimulation potently induces transcription of anti-viral proteins and cytokines in human lung epithelial cells *in vitro*. (A) *ACE2* and *TMPRSS2* gene expression was measured by qPCR in A549 and A549* cells relative to *GAPDH* expression. Data are shown as mean ± SD (n=3). Statistical significance was calculated by two-way ANOVA with Sidak's multiple comparisons post-hoc test. (B) 3pRNA or ctrl RNA was transfected to A549* cells or stimulated with recombinant universal IFNα(A/D). 6 hrs after stimulation, gene expression of anti-viral proteins and cytokines were measured by qPCR and normalized to *GAPDH* expression. Data are presented as fold induction to untreated cells (mean ± SEM (n=3)). Statistical significance was calculated by two-way ANOVA with Dunnett's multiple testing (A) and by one-way ANOVA (Welch) with Dunn's multiple testing (B), when the data were lognormally distributed and otherwise a non-parametric Kruskal-Wallis test with Dunn's multiple testing was applied. * p<0.05, ** p<0.01, *** p<0.001, **** p<0.0001.

In order to assess the inhibition of viral replication by RIG-I activation *in vitro*, A549* cells were treated with 3pRNA or IFNα and, 24 hrs later, pulse-infected with SARS-COV-2 at

an MOI of 0.1 (**Figure 9A**). After 1 hr of inoculation, cells were washed twice with PBS to remove any residual viral particles from the original infection, before fresh medium was added and cells were incubated for further 24 hrs. Viral replication was assessed by quantification of SARS-CoV-2 genomic RNA in challenged cells by qPCR and viral release was quantified by determining the levels of SARS-CoV-2 antigen in the supernatants by ELISA (**Figure 9B** and **Figure 9C**). Cells directly harvested after the 1 hr pulse-infection served as a negative control (neg ctrl). SARS-CoV-2 replication was detectable in untreated cells as indicated by the presence high levels of SARS-CoV-2 RNA in the infected cells (**Figure 9B**) and of SARS-CoV-2 antigens in the supernatants (**Figure 9C)**. In contrast, both RIG-I and IFNα stimulation resulted in a significant reduction of viral titers in A549* cells measured by the low presence of genomic viral transcripts in the cells (**Figure 9B**) as well as by low levels of SARS-CoV-2 antigen in the supernatants (**Figure 9C**). A pronounced anti-viral immune response to SARS-CoV-2 infection was still seen in 3pRNA- treated cells as indicated by the significant upregulation of ISGs (*MX1*, *RSAD2*) and cytokines (*CXCL10*, *IL6*) compared to untreated SARS-CoV-2-challenged cells (**Figure 9D**). 3pRNA showed superior gene induction of anti-viral molecules compared to IFNα upon SARS-CoV-2 infection (**Figure 4D**). It has to be noted that even untreated cells showed low induction of anti-viral proteins and cytokines compared to neg ctrl.

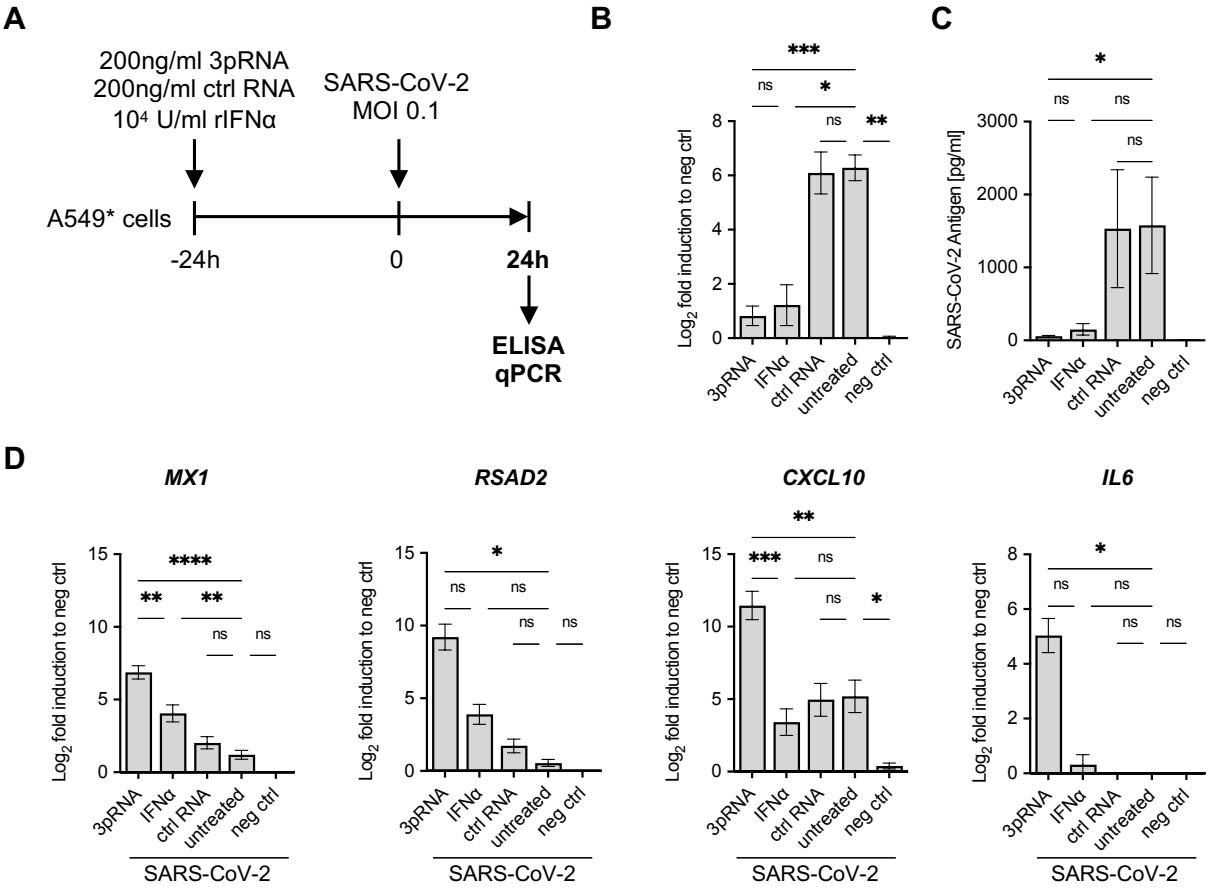

Figure 9: RIG-I and IFNα stimulation inhibits SARS-CoV-2 viral replication and viral release *in vitro*. A549* cells were stimulated with 3pRNA, ctrl RNA or recombinant universal IFNα(A/D) and incubated for 24 hours. Cells were pulse-infected with SARS-CoV-2 (MOI 0.1) for 1 hr, washed and incubated for further 24 hrs. Cells and supernatants were harvested for downstream qPCR analysis and ELISA, respectively. (B) SARS-CoV-2 gene expression was quantified by qPCR, normalized to *GAPDH* and expressed as fold induction to neg ctrl. (C) Quantification of SARS-CoV-2 antigen in the supernatants of SARS-CoV-2-infected cells by ELISA. (D) ISG and cytokine gene expression was quantified by qPCR, normalized to *GAPDH* and expressed as fold induction to neg ctrl. Data are shown as mean ± SEM (n=3-4). Statistical significance was calculated by one-way ANOVA (Welch) with Dunnett's T3 multiple testing, when the data were lognormally distributed and otherwise a non-parametric Kruskal-Wallis test with Dunn's multiple testing was applied. * p<0.05, ** p<0.01, *** p<0.001, **** p<0.0001.

3.3. Systemic RIG-I administration induces potent anti-viral resistance in the lungs of C57BL/6j mice *in vivo*

3.3.1. Induction of cytokines and anti-viral proteins in peripheral organs upon systemic RIG-I agonist injection in C57BL/6j mice *in vivo*

Considering that RIG-I stimulation leads to a robust cytokine and anti-viral protein induction and to a potent inhibition of SARS-CoV-2 replication *in vitro*, application of RIG-I agonists has been suggested to be protective against SARS-CoV-2 *in vivo* as well and hence builds the main rationale of this study. Nonetheless, prior to the evaluation of the potency of RIG-I ligands in the protection from SARS-CoV-2 infection in a mouse model, the immediate immune effects of systemic RIG-I stimulation *in vivo* were assessed by quantification of serum cytokines. Accordingly, 6.25 µg of 3pRNA or ctrl RNA was complexed in the transfection reagent *in vivo*-JetPEI and intravenously (i.v.) injected into the tail vein of naïve C57BL/6j mice (**Figure 10A**). After 6 hrs, serum was collected and the cytokine profile in the sera of 3pRNA-exposed animals was analyzed in a LEGENDplex-based anti-virus response assay (**Figure 10B**). As expected, 3pRNA led to the secretion of type I IFNs (IFNα and IFNß). Secretion of the type II IFN, namely IFNγ, as well as of the pro-inflammatory cytokine IL-6 were also significantly induced upon 3pRNA stimulation (**Figure 10B**). Besides cytokine secretion, significant amounts of inflammatory chemokines were detected in the sera of 3pRNA-treated animals, as observed strongly for CXCL10, CCL2 and CCL5, but also CXCL1. In contrast, ctrl RNA stimulation did not result in detectable IFN or cytokine production and was comparable to that seen in PBS-treated mice (**Figure 10B**). Furthermore, no differences in the secretion of IL-10, IL-1b, IL-12p70 and GM-CSF was detectable in the treated groups (data not shown).

Type I IFN production into the sera was shown to be dose-dependent. Systemic administration of 20 µg 3pRNA revealed 720-fold higher levels of IFNα and 91-fold higher levels of IFNβ in the sera of mice at 4 hrs after administration compared to the levels upon 6.25 µg 3pRNA administration (**Figure 10D**). IL-6 production was moderately increased (16-fold) upon 20 µg 3pRNA administration. In contrast, indistinguishable levels (1.2-fold) of CXCL10 were secreted into the sera upon the low (**Figure 10B**) or high dose administration (**Figure 10D**) of 3pRNA.

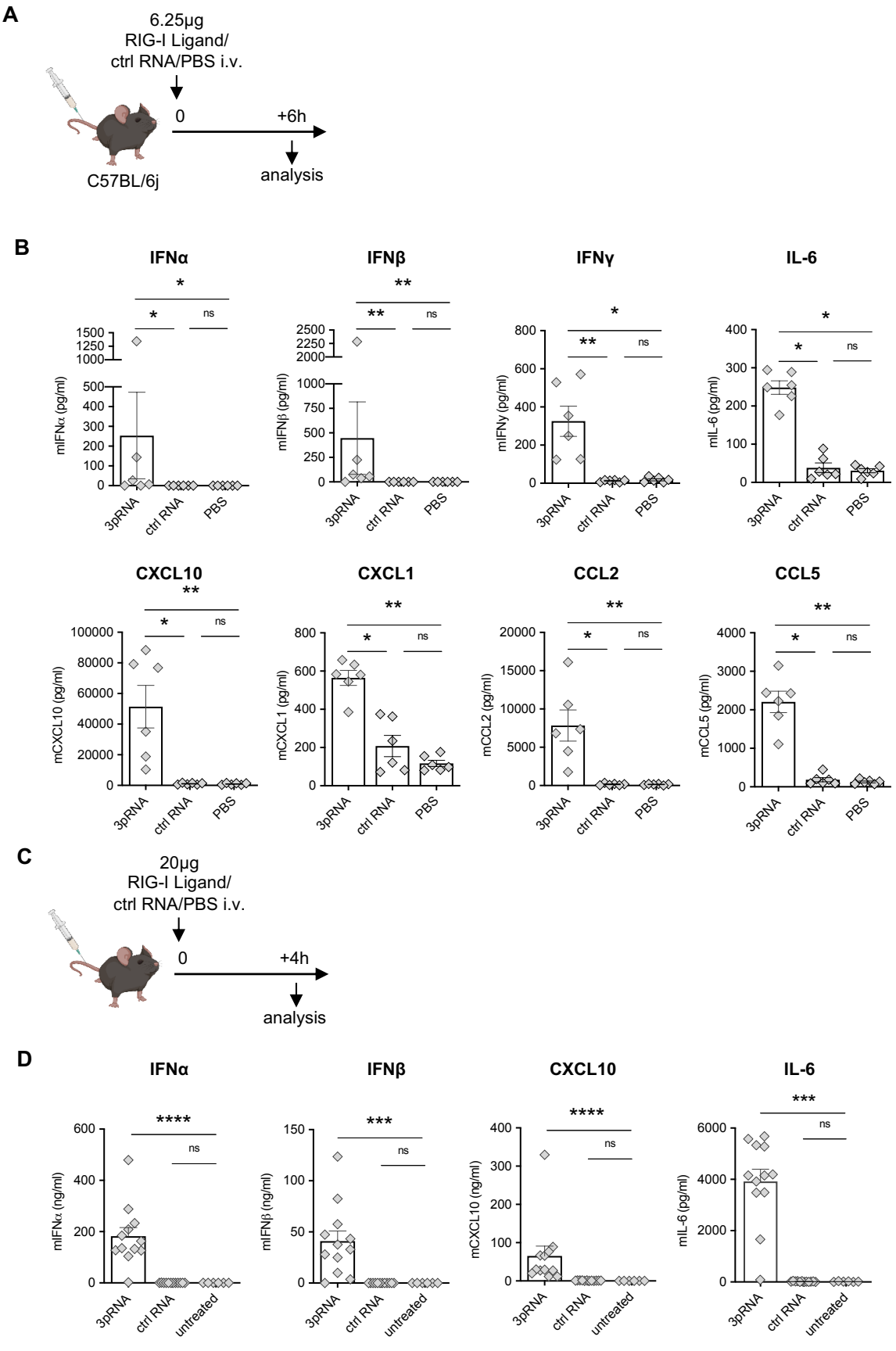
A
6.25µg
RIG-I Ligand/
ctrl RNA/PBS i.v.
0
+6h
analysis
C57BL/6j
B
IFNα
IFNβ
IFNγ
IL-6
mIFNα (pg/ml)
mIFNβ (pg/ml)
mIFNγ (pg/ml)
mIL-6 (pg/ml)
CXCL10
CXCL1
CCL2
CCL5
mCXCL10 (pg/ml)
mCXCL1 (pg/ml)
mCCL2 (pg/ml)
mCCL5 (pg/ml)
3pRNA
ctrl RNA
PBS
ns
C
20µg
RIG-I Ligand/
ctrl RNA/PBS i.v.
0
+4h
analysis
D
IFNα
IFNβ
CXCL10
IL-6
mIFNα (ng/ml)
mIFNβ (ng/ml)
mCXCL10 (ng/ml)
mIL-6 (pg/ml)
3pRNA
ctrl RNA
untreated
ns

Figure 10: Systemic 3pRNA administration results in high cytokine production in sera of naïve mice *in vivo*. (A) Experimental setup. C57BL/6j mice were i.v. injected with 6.25 µg 3pRNA or ctrl RNA complexed to *in vivo*-JetPEI. After 6 hrs, serum was collected. (B) LEGENDplex data from sera of 3pRNA-, ctrl RNA- and PBS- treated mice (n=6, pooled from two experiments). (C) Experimental setup. C57BL/6j mice were i.v. injected with 20 µg 3pRNA or ctrl RNA complexed to *in vivo*-JetPEI. After 4 hrs, serum was collected. (D) LEGENDplex data from sera of 3pRNA-, ctrl RNA- and PBS- treated mice (3pRNA and ctrl RNA n=12, untreated n=6). Data are shown as mean ± SEM (n=12). Statistical significance was calculated by Kruskal−Wallis test and Dunn's multiple testing. * $p<0.05$, ** $p<0.01$, *** $p<0.001$, **** $p<0.0001$.

Besides analyzing the cytokine and chemokine response in sera, the effects of RIG-I stimulation on the lungs as the main target organ of respiratory virus infections were examined in regard to the establishment of an anti-viral transcriptional state and activation of organ-resident immune cells. 6 hrs after 6.25 µg 3pRNA administration the liver, lungs and spleen were collected for downstream gene expression analysis. Expression of pro-inflammatory cytokines and IFN-inducible anti-viral proteins were measured by qPCR, normalized to murine *Gapdh* and were presented as fold induction to the PBS group (**Figure 11**). Indeed, in the lungs, spleen and the liver, 3pRNA led to the significant induction of the transcript of *Ddx58*, the coding gene for RIG-I (*Ddx58*) (**Figure 11**). Furthermore, the proinflammatory mediators *Il6* and *Ccl2* as well as the ISG *Cxcl10* were significantly upregulated in all three organs analyzed upon RIG-I ligand administration. Besides the upregulation of transcripts encoding cytokines, RIG-I activation also strongly induced transcription of the anti-viral protein *Rsad2.* In contrast to 3pRNA, ctrl RNA did not induce the analyzed genes compared to the PBS administration, indicating that RIG-I agonists indeed possess a RIG-I specific stimulation.

Collectively, RIG-I activation induced an anti-viral immune response *in vivo* as indicated by the production of type I IFNs and pro-inflammatory cytokines as well as by the induction of prominent ISGs in the lungs, liver and spleen.

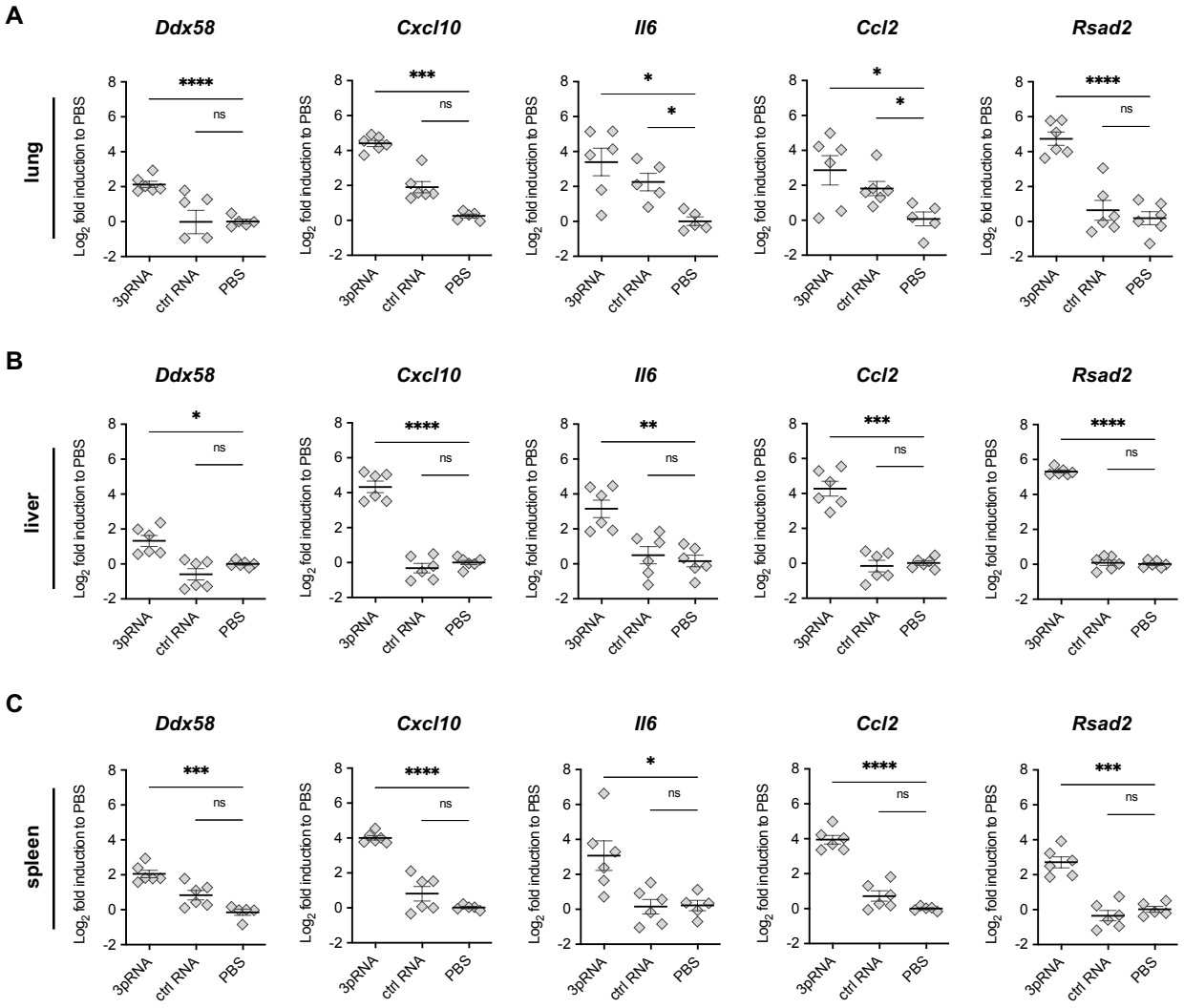

Figure 11: Systemic RIG-I ligand administration strongly induces transcription of cytokines and anti-viral proteins in peripheral organs of C57BL/6j mice. Organs were collected from the mice 6 hrs after 6.25 µg 3pRNA or ctrl RNA i.v. injection. Cytokine and ISG gene expression in the lungs (A), liver (B) and spleen (C) were measured by qPCR, normalized to *Gapdh* and presented as fold induction to the PBS group. Data are shown as mean ± SEM (n=6, pooled data from 2 independent experiments). Statistical significance was calculated by one-way ANOVA (Welch) with Dunnett's T3 multiple testing, when the data were lognormally distributed, and otherwise a non-parametric Kruskal-Wallis test with Dunn's multiple testing was applied. * $p<0.05$, ** $p<0.01$, *** $p<0.001$, **** $p<0.0001$.

3.3.2. Activation of innate and adaptive effector immune cells in the lungs upon RIG-I stimulation

Next, the immune cell composition and activation of the lungs on a single-cell level was evaluated by flow cytometry upon 6.25 µg 3pRNA i.v. administration (**Figure 12**). Single-cell suspensions of lung tissue was stained for the most abundant immune cells. Cell frequencies of the effector cells of innate and adaptive immunity, namely T cells ($CD4^+$ or $CD8^+CD45^+$ cells), B cells ($CD19^+CD45^+$ cells) and NK cells ($NK1.1^+CD45^+$ cells), relative to all CD45+ immune cells were quantified.

The frequencies of $CD4^+$ T cells and B cells were each decreased by two thirds in the 3pRNA-treated group compared to the PBS group which was accompanied by a strong influx of NK cells from 8 % to 19 % of $CD45^+$ cells (**Figure 12A**). Ctrl RNA treatment did not influence the immune cellular composition in the lungs compared to PBS. In addition, the activation status of these effector immune cells was quantified by measuring the expression of CD69 and PD1. The percentages of $CD69^+$ and $PD1^+$ cells relative to the parental cell population is shown in **Figure 12B** and **Figure 12C**. While in the ctrl RNA and the PBS group negligible numbers of $CD69^+$ $CD4^+$T, $CD8^+$T, B and NK cells were detected, RIG-I stimulation led to the strong upregulation of CD69 expression in these effector cells, leading to 52 % $CD69^+$ T and B cells and 90 % of $CD69^+$ NK cells (**Figure 12B**). In addition, PD1 expression was upregulated in T cells leading to approx. 26 % $PD1^+CD4^+$ and 55 % $PD1^+CD8^+$ T cells, whereas B and NK cells exhibited negligible PD1 frequencies (**Figure 12C**).

It was also interesting to investigate the effects of RIG-I stimulation in peripheral organs beyond the lungs. Hence, the immune composition within the spleen and axillary lymph nodes were analyzed by flow cytometry as well (**Appendix Figure 1**). While in the spleen NK cell numbers decreased from 3 % to 2 % of $CD45^+$ cells and B cell numbers were slightly increased by approx. 10 % (**Appendix Figure 1A**), in the lymph nodes no changes in cell frequencies of $CD4^+$ and $CD8^+$ T, B and NK cells were visible upon RIG-I stimulation (**Appendix Figure 1B**). Nevertheless, CD69 expression was shown on >80 % of NK cells in the spleen and lymph nodes upon RIG-I stimulation, on 40 % of $CD4^+$ and $CD8^+$ T cells in the spleen and on 35 % of B cells in the lymph nodes (**Appendix Figure 1B** and **Appendix Figure 1D**).

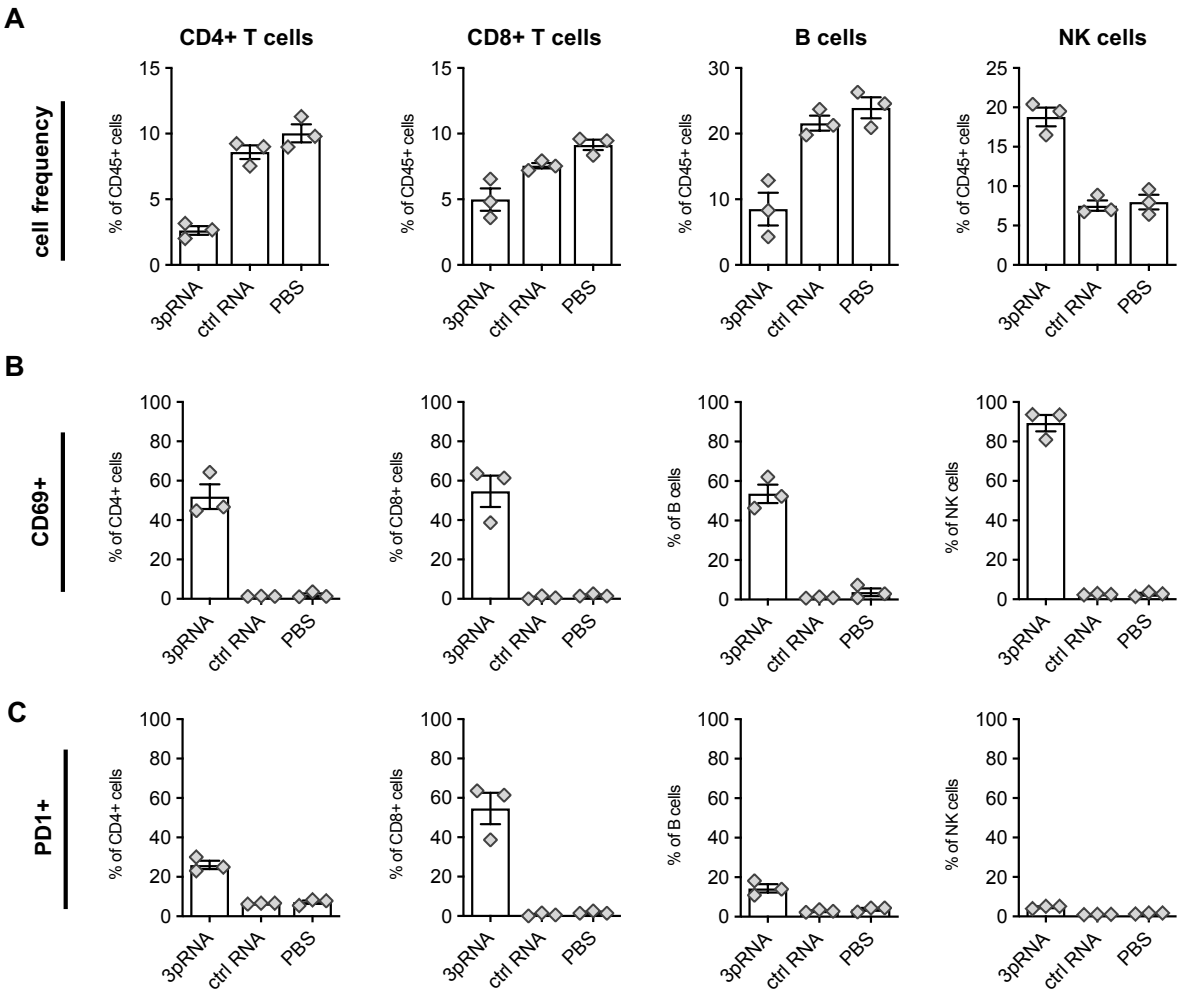

Figure 12: 3pRNA stimulation recruits NK cells to the lungs and leads to broad effector immune cell activation. Lungs were collected for flow cytometry from mice 6 hrs after 6.25 µg 3pRNA or ctrl RNA i.v. injection. Frequencies of immune effector cell populations ($CD4^+$ and $CD8^+$ T cells, B cells, NK cells) in the lungs relative to all $CD45^+$ cells. (B) Frequencies of $CD69^+$ (B) and $PD1^+$ (C) cells compared to parental cell population. Data are shown as mean ± SEM (n=3) and are representative of two independent experiments.

3.3.3. Activation of myeloid cells in the lungs upon systemic RIG-I stimulation

Lung-resident macrophages are crucial in the defense against pathogens and can be subdivided into unique macrophage populations with distinct locations and functions. The gating strategy for the myeloid cells in the lungs is shown in **Appendix Figure 2.** Alveolar macrophages (AMs) were distinctly identified as $CD45^+CD11b^-CD64^+Ly6C^-F4/80^+$ cells. Upon RIG-I stimulation, no changes in the cell numbers or immune activation as measured by the low $CD69^+$ and $CD86^+$ cell frequencies relative to all AMs were visible (**Figure**

13A). Yet, AMs presented constitutive high PDL1 expression even in unstimulated mice. Interstitial macrophages (IMs) form a second group of resident lung-specific macrophages and were gated as $CD45^{+}CD11b^{hi}Ly6G^{-}Ly6C^{-}CD64^{+}$ cells (**Figure 13B**). RIG-I stimulation did not alter the frequency of these cells as well, yet led to the induction of CD69 and PDL1 resulting in high frequency of $CD69^{+}$ and PDL-1^{+} IMs. A third group of myeloid cells are monocytes that were divided into two subpopulations by the differential expression of Ly6C (**Figure 13C** and **Figure 13D**). An influx of inflammatory monocytes (gated as $CD45^{+}CD11b^{+}Ly6G^{-}Ly6C^{hi}$ cells) into the lungs was observed upon RIG-I stimulation doubling the relative number of these cells, and >50 % of cells were activated as shown by the expression of CD69, CD86 and/or PDL-1 (**Figure 13C)**. In contrast, no recruitment or substantial immune cell activation of resident monocytes (gated as $CD45^{+}CD11b^{+}Ly6G^{-}Ly6C^{-}$ cells) was observed (**Figure 13D**). Neutrophils were identified by the high expression of Ly6C and Ly6G. Despite already present in high numbers (18 %) in the naïve lungs, an additional recruitment of neutrophils into the lungs was visible upon RIG-I stimulation (28 %) and showed PDL-1 expression in 58 % of neutrophils (**Figure 13E**). At last, a small population of eosinophils (3 %, gated as $CD45^{+}CD11b^{+}Ly6G^{-}Ly6C^{+}SSC\text{-}A^{hi}$ cells) was observed in the lungs that did not show any signs of activation (**Figure 13F**).

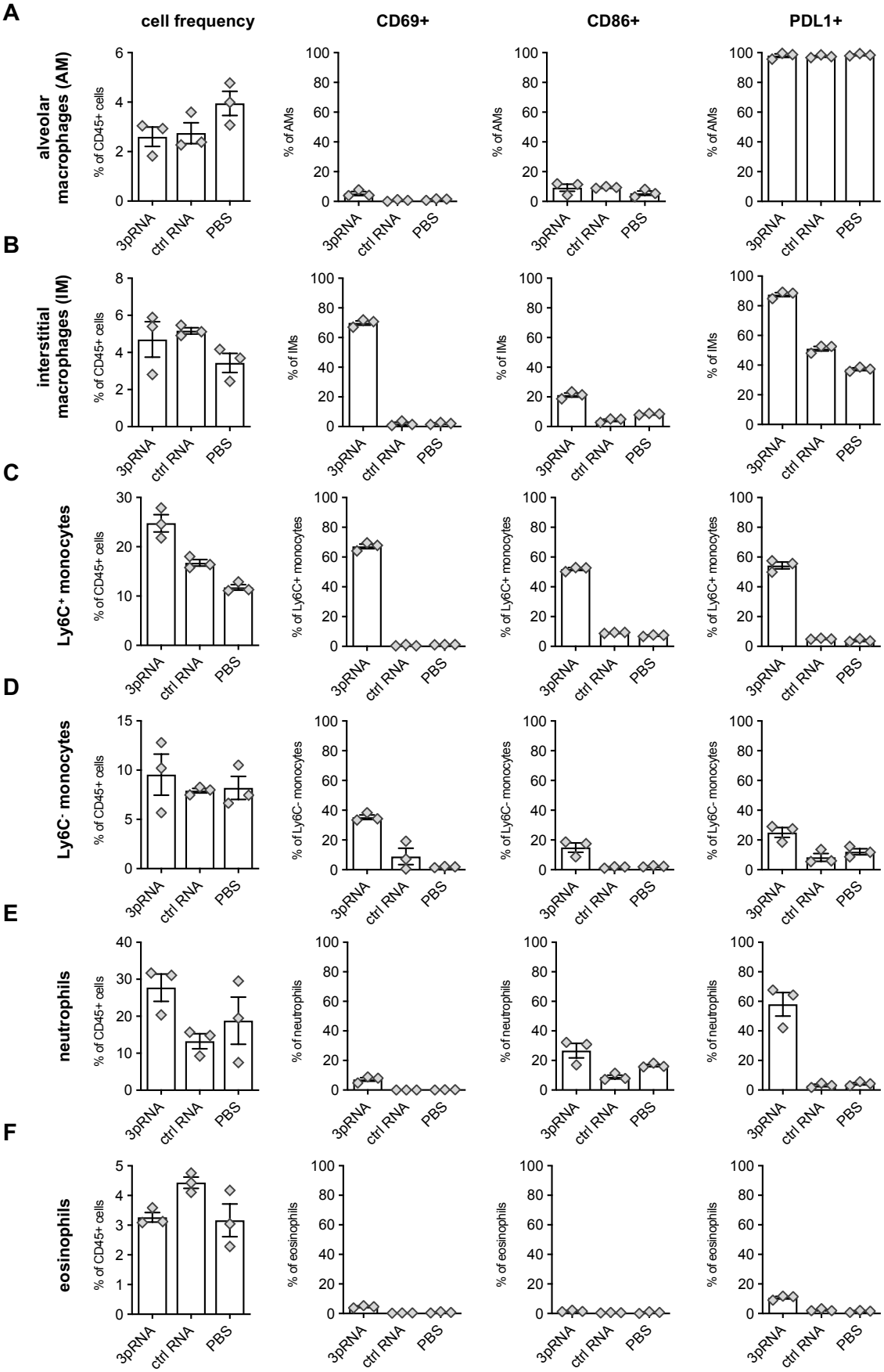
A
B
C
D
E
F
cell frequency
CD69+
CD86+
PDL1+
alveolar macrophages (AM)
interstitial macrophages (IM)
Ly6C+ monocytes
Ly6C- monocytes
neutrophils
eosinophils
% of CD45+ cells
% of AMs
% of IMs
% of Ly6C+ monocytes
% of Ly6C- monocytes
% of neutrophils
% of eosinophils
3pRNA
ctrl RNA
PBS

Figure 13: Inflammatory myeloid cells are recruited to the lungs and activated upon systemic 3pRNA stimulation. Lungs were collected for flow cytometry from mice 6 hrs after 6.25 µg 3pRNA or ctrl RNA i.v. injection. The gating strategy is shown in **Appendix Figure 2**. Frequencies of myeloid cell populations in the lungs relative to all $CD45^+$ cells and frequencies of $CD69^+$, $CD86^+$ and $PDL1^+$ cells compared to parental cell population. Data are shown as mean ± SEM (n=3) and are representative of two independent experiments.

3.4. 3pRNA treatment in K18-hACE2 mice results in a reduction of viral replication and local inflammation in the lungs during active SARS-CoV-2 infection

Reasoning the establishment of viral resistance upon RIG-I activation *in vitro* and *in vivo* as demonstrated in the last chapters, the efficacy of RIG-I agonists was evaluated in a mouse model of severe SARS-CoV-2 infection in the following chapters of this thesis.

K18-hACE2 transgenic mice express the human *ACE2* under the control of the endogenous *Cytokeratin-18* promotor. Gene expression analysis of organs collected from uninfected K18-hACE2 mice demonstrated high expression of *ACE2* in the lungs, colon and intestines and moderate expression in the brain (**Figure 14**). In contrast, *ACE2* expression was completely absent in the organs of WT littermates.

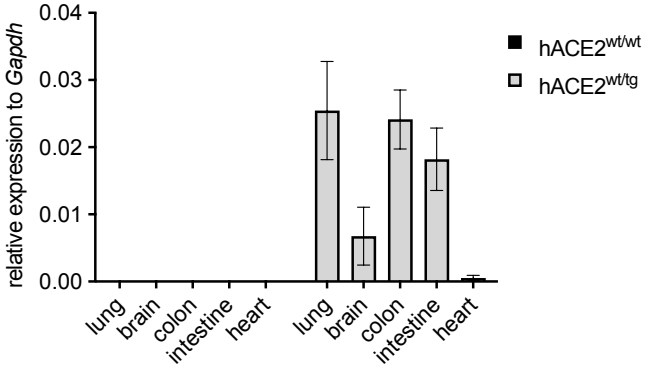

Figure 14: High *ACE2* expression is seen in SARS-CoV-2 target organs of K18-hACE2$^{wt/tg}$ mice. RNA of the lungs, brain, colon, intestines and heart of naïve K18-hACE2$^{wt/tg}$ and WT counterparts were isolated. *ACE2* gene expression was quantified by qPCR and presented as relative expression values to *Gapdh* expression. Data are shown as mean ± SEM (n=3).

3.4.1. Prophylactic and therapeutic 3pRNA administration reduces viral replication in the lungs during active SARS-CoV-2 infection in K18-hACE2 mice

First, the potency of RIG-I stimulation in limiting SARS-CoV-2 viral replication *in vivo* was assessed. Therefore, K18-hACE2 transgenic mice were i.v. injected with a single dose of 20 µg 3pRNA complexed to *in vivo*-JetPEI one day prior (3pRNA d-1) or one day after

(3pRNA d+1) the intranasal (i.n.) challenge with 5x10^4 PFU SARS-CoV-2 (**Figure 15A**). Control mice were either i.v. injected with ctrl RNA complexed to *in vivo*-JetPEI one day prior to the infection or left untreated. All mice were sacrificed 4 days post infection (dpi) and lungs and brain were collected for downstream analysis.

Quantification of SARS-CoV-2 viral RNA by qPCR revealed high viral titers in the lungs of untreated and ctrl RNA- treated animals (**Figure 15B**). In contrast, both 3pRNA prophylactic and therapeutic treatment significantly reduced viral burden compared to untreated animals. Moreover, SARS-CoV-2-infected mice showed an interindividual heterogeneity in the severity of viral burden in the brain as quantified by variable levels of viral RNA (**Figure 15C**). Nevertheless, 3pRNA prophylaxis reduced the viral RNA expression in the brain as well and 5/6 mice presented RNA levels nearly at the detection limit. In contrast, for the therapeutic 3pRNA treatment only a non-significant tendency towards lower viral copy numbers compared to untreated animals was seen.

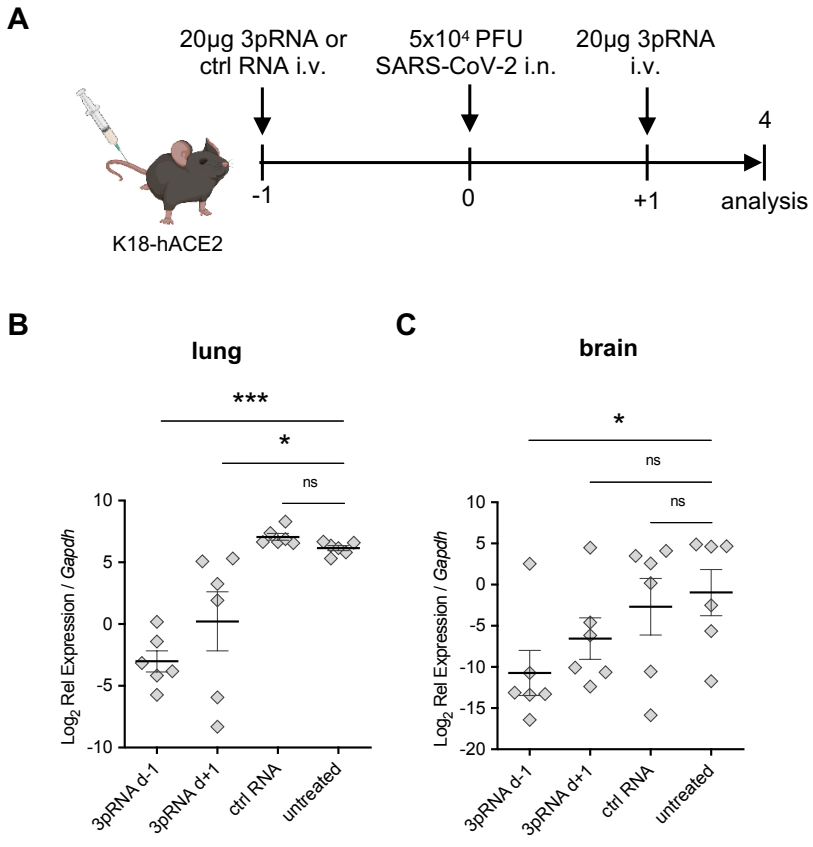

Figure 15: 3pRNA treatment reduces viral transcript levels in the lungs and brain of mice during active SARS-CoV-2 infection. (A) Experimental setup. K18-hACE2 mice were i.v. injected with 20 µg 3pRNA or ctrl RNA complexed to *in vivo*-JetPEI one day prior (3pRNA d-1) or after (3pRNA d+1) infection. Mice were infected i.n. with 5x10^4 PFU SARS-CoV-2 and sacrificed 4 dpi. (B,C) SARS-CoV-2 gene expression in the lungs (B)

and in the brain (C) at 4 dpi was quantified by qPCR relative to murine *Gapdh* expression. Data are presented as mean ± SEM (n=6). Statistical significance was calculated by one-way ANOVA (Welch) with Dunnett's T3 multiple testing, when the data were lognormally distributed and otherwise a non-parametric Kruskal-Wallis test with Dunn's multiple testing was applied. * $p<0.05$, ** $p<0.01$, *** $p<0.001$, **** $p<0.0001$.

Besides quantification of SARS-CoV-2 transcript levels, immunohistochemical staining of SARS-CoV-2 nucleocapsid protein in lung tissue was established to visually assess the effects of the 3pRNA treatment on the viral spread during active SARS-CoV-2 infection. Uninfected organs were used as negative control and showed none to minimal staining in the smooth muscle around bronchioles (data not shown). A clear difference in the staining pattern was observed in SARS-CoV-2-infected lung samples. Representative pictures of SARS-CoV-2 nucleocapsid protein staining are presented in **Figure 16A.** Lung samples from untreated and ctrl RNA-treated mice showed broad positive staining throughout the tissue indicating the large presence of the ongoing SARS-CoV-2 infection on 4 dpi. In contrast, lungs from mice that received a prophylactic or therapeutic dose of 3pRNA only presented a few focal spots of positive staining throughout the lung tissue or around bronchioles. Scoring by three independent scientists in a blinded fashion led to high scores in untreated and ctrl RNA- treated animals, whereas mice pre-treated with 3pRNA one day prior to the viral challenge reached significantly lower scores, suggesting a partial inhibition of viral spread in 3pRNA-treated mice (**Figure 16C).** Therapeutic 3pRNA treatment resulted in a modest but not significant reduction of SARS-CoV-2 spread in the lungs when compared to controls.

Immunohistochemical SARS-COV-2 nucleocapsid staining of brain sections on day 4 post infection indicated that approx. 50 % of untreated animals presented with a strong staining pattern throughout the tissue (**Figure 16B**) suggesting a partial viral manifestation of infection into the central nervous system as seen in the qPCR before (**Figure 15C**). The majority of animals showed only few spots of positive staining that was translated to low scores. Despite a visible trend to low scores, 3pRNA- treatment did not significantly inhibit viral manifestation in the brain (**Figure 16D).** Finally, scores strongly correlated with the viral RNA copy numbers determined in the qPCR analysis in both the lungs and the brain (**Figure 16E** and **Figure 16F**).

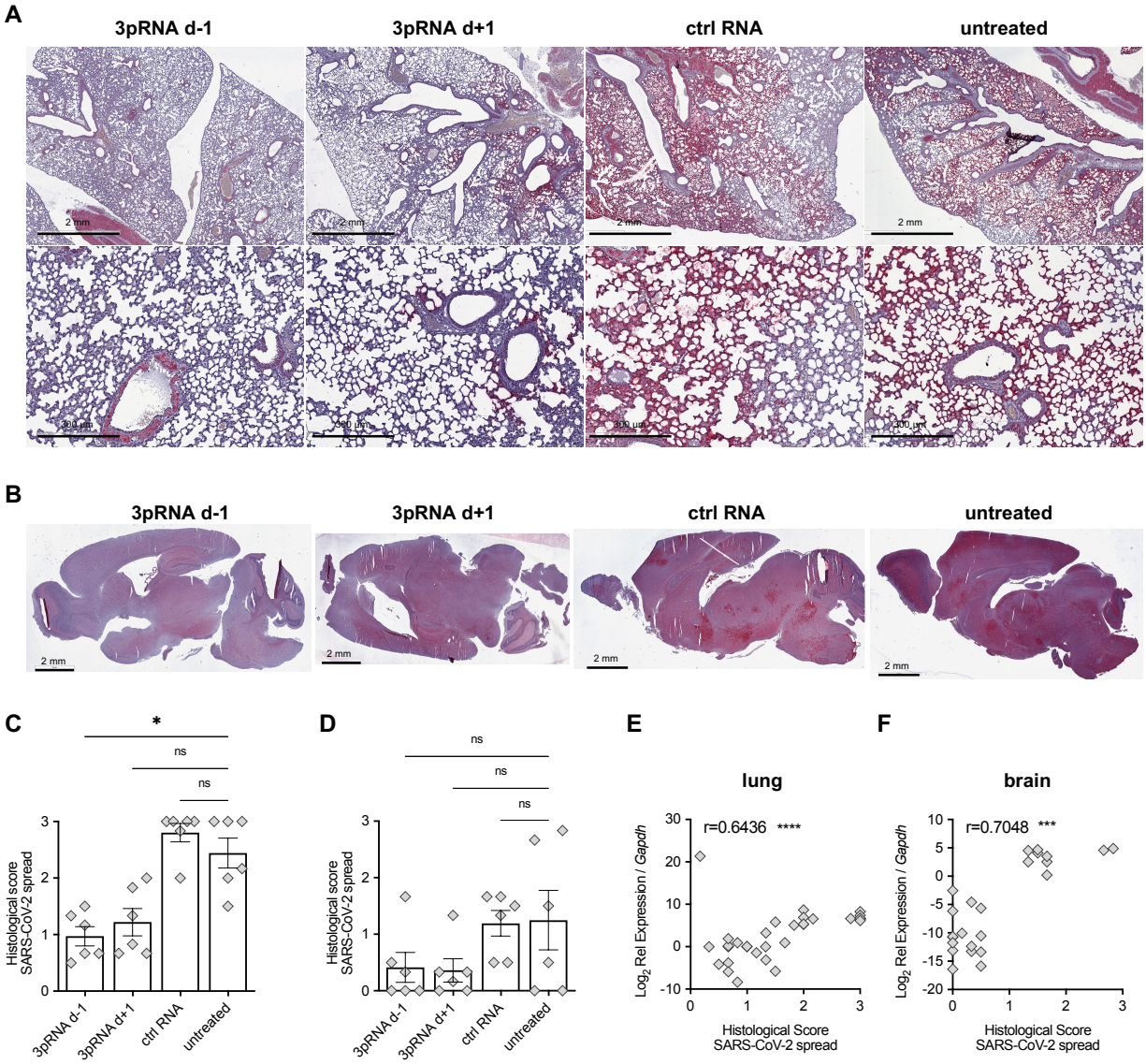

Figure 16: Immunohistochemical analysis of mice during active SARS-CoV-2 infection reveals inhibition of viral spread in the lungs and brain upon prophylactic and therapeutic 3pRNA treatment. Lungs and brain were collected for immunohistochemical analysis from SARS-CoV-2-infected K18-hACE2 mice upon 3pRNA treatment on 4 dpi as shown in **Figure 15**. (A,B) Representative pictures and (C,D) scoring of immunohistochemical staining of SARS-CoV-2 nucleocapsid protein in lung (A,C) and brain (B,D) sections. Data are shown as mean ± SEM (n=6). Statistical significance was calculated by non-parametric Kruskal−Wallis test with Dunn's multiple testing (C,D). (E,F) Correlation between histological scores of SARS-CoV-2 spread (x-axis) and SARS-CoV-2 transcript levels as presented in **Figure 15** (y-axis) in the lungs (E) and brain (F). For statistical analysis the Spearman coefficient was calculated as indicated (n=24). * p<0.05, ** p<0.01, *** p<0.001, **** p<0.0001.

3.4.2. RIG-I stimulation reduces local inflammation in the lungs of SARS-CoV-2-infected K18-hACE2 mice

As demonstrated *in vitro*, RIG-I stimulation induces transcription of pro-inflammatory cytokines and anti-viral proteins in target cells in the absence (**Figure 8B**) or presence (**Figure *9*D**) of SARS-CoV-2 viral infection. Therefore, it was most interesting to investigate whether RIG-I stimulation had an impact on the local anti-viral response and inflammation in SARS-CoV-2-infected K18-hACE2 mice as well. In the lungs, *Il6*, *Cxcl10* and *Ccl2* RNA expression levels were highly induced in untreated and ctrl RNA-treated SARS-CoV-2-infected animals compared to untreated uninfected animals (**Figure 17A**). However, both 3pRNA prophylaxis and therapeutic treatment significantly reduced cytokine expression in the lungs. In the brain, increased expression of *Il6*, *Cxcl10* and *Ccl2* compared to uninfected mice was detectable in SARS-CoV-2-infected mice as well (**Figure 17B**), but the number of transcripts encoding these cytokines was lower than in the lungs. Neither the 3pRNA prophylactic nor the therapeutic administration reduced the local inflammation in the brain as evidenced by nonsignificant lower cytokine RNA levels (**Figure 17B**).

Collectively, systemic administration of RIG-I agonists significantly interfered with SARS-CoV-2 viral replication as indicated by reduced viral burden in the lungs and brain and less inflammation in the lungs during the active course of SARS-CoV-2 infection.

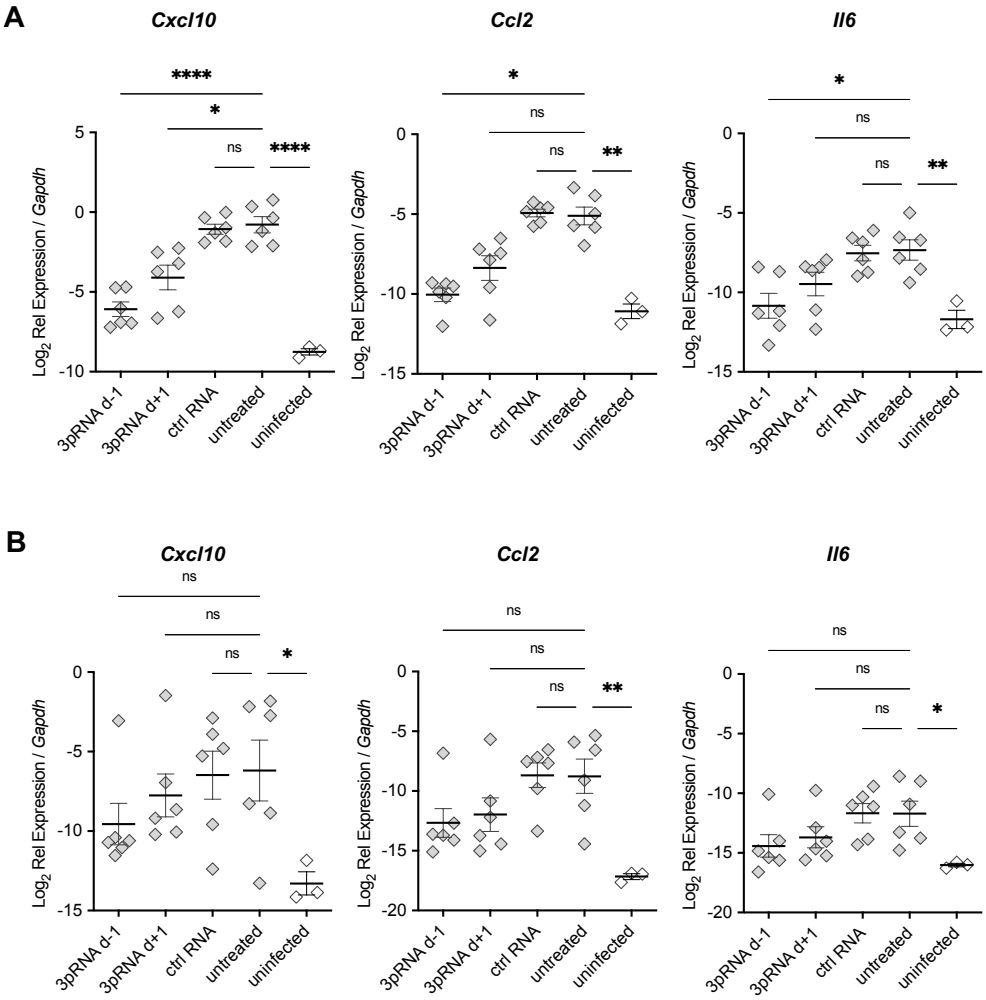

Figure 17: Reduced inflammation in the lungs of 3pRNA-treated K18-hACE2 mice during active SARS-CoV-2 infection. RNA of lungs and brain were isolated from SARS-CoV-2-infected K18-hACE2 mice upon 3pRNA treatment on 4 dpi as shown in **Figure 15**. Cytokine gene expression in the lungs (A) and brain (B) was quantified by qPCR relative to murine G*apdh* expression. Data are presented as mean ± SEM (n=6, uninfected n=3). Statistical significance was calculated by one-way ANOVA (Welch) with Dunnett's T3 multiple testing, when the data were lognormally distributed and otherwise a non-parametric Kruskal-Wallis test with Dunn's multiple testing was applied. * p<0.05, ** p<0.01, *** p<0.001, **** p<0.0001.

3.5. Prophylactic RIG-I activation confers protection from severe SARS-CoV-2 infections in K18-hACE2 mice

3.5.1. RIG-I prophylaxis rescues K18-hACE2 mice from lethal SARS-CoV-2 infections

So far, the impact of systemic prophylactic and therapeutic RIG-I ligand administration on the inhibition of SARS-CoV-2 viral replication and on local inflammation in the lungs and brain has been demonstrated by gene expression analysis and immunohistochemical staining at 4 dpi (**Figure 15**,**Figure 16**,**Figure 17**). To investigate whether this translates into the potent protection from the SARS-CoV-2-associated lethality of this mouse model, survival experiments were performed that included single prophylactic 3pRNA treatments on several days prior to a lethal SARS-CoV-2 infection. K18-hACE2 mice were treated with a single dose of 20 µg 3pRNA seven days (d-7), three days (d-3) or one day (d-1) prior to a lethal i.n. $5x10^4$ PFU SARS-CoV-2 inoculation (**Figure 18A**). Ctrl RNA was only administered one day prior to the lethal infection. Both 3pRNA and ctrl RNA were complexed to *in vivo*-JetPEI and injected systemically via the i.v. route. Weight and appearance of mice was assessed on a daily basis and mice did not show weight loss nor other side effects from the prophylactic 3pRNA treatment prior to the infection (**Figure 18B**). However, a significant weight loss was indicative for the developing COVID-19 infection and was used as surrogate marker for the health state of the mouse. Besides weight loss, the clinical presentation of the mice was daily monitored. Signs of disease occurring during SARS-CoV-2 infections ranged from reduced activity, increased respiration, eye openings clotted by secretion to complete lethargy. When mice reached ≥20 % of weight loss relative to their starting weight at day 0 (day of virus infection) and/or presented overt signs of disease, as stated before, they were sacrificed and organs were collected for downstream analysis. Rarely, an intestinal phenotype with bowel obstructions or neurological signs of disease marked by progressive motor deficits were observed which also mandated immediate euthanasia. Animals that did not reach the endpoint criteria during the observation period of the experiment were sacrificed on day 13 post infection (dpi) (**Figure 18A**).

SARS-CoV-2-infected mice rapidly developed significant weight loss and signs of disease by day 4 post infection (**Figure 18D**). When left untreated, mice reached the euthanasia criteria by day 4 to day 6 post infection, (**Figure 18C-D**, black line). Treatment with ctrl RNA did not confer any protection either (**Figure 18C-D**, black dotted line). In contrast, a

single injection of 3pRNA substantially alleviated disease outcome. The single, prophylactic 3pRNA treatment one day (d-1) prior to the lethal viral infection improved the survival rate from 0 % to 50 % (5/10 animals survived) (**Figure 18C**, red line). Pre-treatment three days (d-3) or seven days (d-7) prior to infection still improved survival by 25-33 % (2/8 and 3/9 animals survived) (**Figure 18C**, green and blue line). Even though a large proportion of the 3pRNA-treated mice (17/27) was not protected from lethality, these mice still showed prolonged survival compared to untreated mice, as indicated by improved survival as indicated on the Kaplan-Meier curve (**Figure 18C**) and by delayed weight loss (**Figure 18E**). Surviving mice were completely protected from substantial weight loss and did not experience any signs of disease throughout the course of the experiment (**Figure 18E**). These results provide evidence for a long-lasting prophylactic effect of the single, selective RIG-I activation against the otherwise lethal SARS-CoV-2 infection and conferred partial protection for up to seven days.

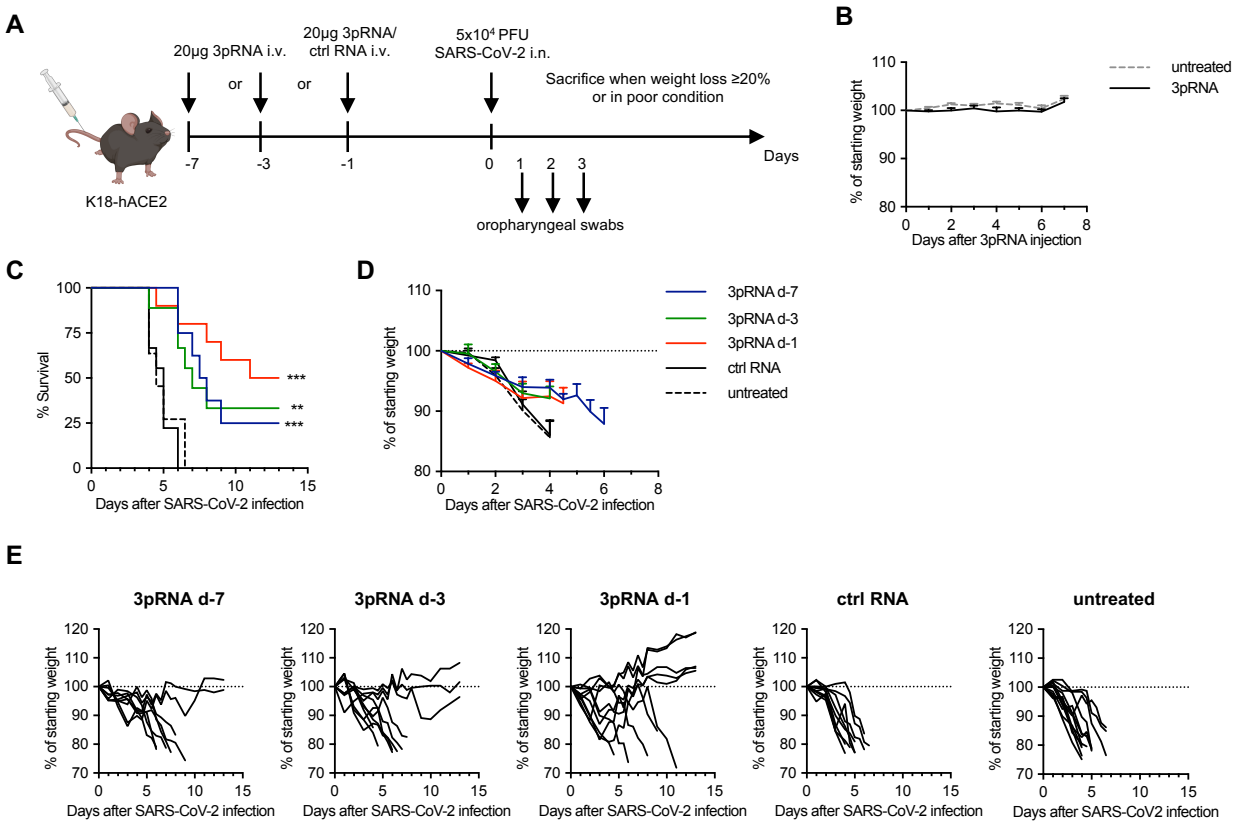

Figure 18: Prophylactic RIG-I ligand treatment provides protection from lethal SARS-CoV-2 infection in K18-hACE2 mice. (A) Experimental setup. K18-hACE2 mice were i.v. injected with 20 µg 3pRNA or ctrl RNA complexed to *in vivo*-JetPEI on indicated days. On day 0, mice were i.n. infected with 5x10^4 PFU SARS-CoV-2 virus. Oropharyngeal swabs were obtained on day 1 to day 3 post infection (dpi). Disease development and

survival were monitored up to twice daily until reaching the endpoint criteria or 13 dpi. (B) Weight development of 3pRNA-treated animals. Data are shown as mean + SEM (3pRNA n=8, untreated n=11). (C) Kaplan-Meier curve and (D) weight loss (pooled) of SARS-CoV-2-infected animals (E) Individual weight loss over time of each SARS-CoV-2-infected mouse until reaching the endpoint criteria or 13 dpi. (C-E) Data are shown as mean + SEM (3pRNA d-7 n=8, 3pRNA d-3 & ctrl RNA n=9, 3pRNA d-1 n=10, untreated n=11). Data are pooled from two independent experiments. Statistical significance was calculated by log-rank Mantel−Cox test (C). * p<0.05, ** p<0.01, *** p<0.001, **** p<0.0001.

Additionally, sera of all animals were collected at the individual time of death or at the end of the experiment course (day 13 post infection, as seen in **Figure 18C**) and tested for the presence of anti-SARS-CoV-2- specific IgG antibodies. All surviving 3pRNA-treated and 4/17 of 3pRNA-treated non-surviving animals generated SARS-CoV-2 specific IgG antibodies leading to significant differences between 3pRNA d-1-treated mice and untreated animals (**Figure 19A**). Detected antibodies were also of neutralizing character, as measured in a competitive binding NeutraLISA assay (**Figure 19B**) that quantifies the inhibitory effects of sera on the interaction between ACE2 and the SARS-CoV-2 spike protein *in vitro*. Of note, untreated and ctrl RNA- treated mice showed comparable IgG antibody titers to uninfected animals.

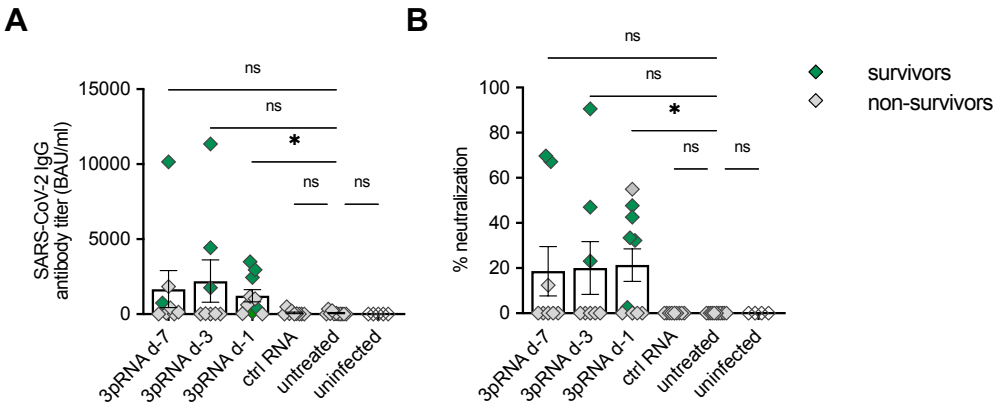

Figure 19: Surviving 3pRNA-treated animals have generated anti-SARS-CoV-2 neutralizing IgG antibodies. Serum was collected from SARS-CoV-2- infected K18-hACE2 mice upon prophylactic 3pRNA treatment on their individual time point of death or 13 dpi as presented in **Figure 18**. (A) Quantification of anti-SARS-CoV-2 specific IgG antibody titers in sera (B) Percent of inhibition of SARS-CoV-2 S1/RBD-hACE2 interaction by sera. Data are shown as mean ± SEM (3pRNA d-7 n=8, 3pRNA d-3 & ctrl RNA n=9, 3pRNA d-1 n=10, untreated n=11, uninfected n=5). Data are pooled from two independent experiments. Statistical significance was calculated by non-parametric Kruskal−Wallis test with Dunn's multiple testing. * p<0.05, ** p<0.01, *** p<0.001, **** p<0.0001.

3.5.2. 3pRNA prophylactic treatment reduces the early viral replication in the upper respiratory tract and inhibits viral transmission into the lungs of K18-hACE2 mice

To monitor viral replication, oropharyngeal swab material in the early phase of the SARS-CoV-2 infection was collected from the SARS-CoV-2-infected mice upon 3pRNA prophylaxis shown in **Figure 18** on day 1 to 3 post infection. The presence of SARS-CoV-2 antigen in the oropharyngeal swab material was determined in an ELISA-based assay (**Figure 20A**) or levels of genomic viral RNA were measured by qPCR (**Figure 20B**). Quantification via both ELISA and qPCR revealed a potent reduction of viral burden on day 1 and 2 post infection in the upper respiratory tract in mice which received prophylactic systemic treatment with 3pRNA (**Figure 20A** and **Figure 20B**). Treatment of mice with 3pRNA three days (d-3) or one day (d-1) prior to the infection resulted in the significant inhibition of viral replication and spread and similar trends were observed, when animals were treated seven days prior to infection, however this was not significant. In contrast, pre-treatment with ctrl RNA did not suppress viral replication. By day three post infection, viral antigens were no longer detected in mice suggesting that the infection had been cleared from the upper respiratory tract when the swabs were taken.

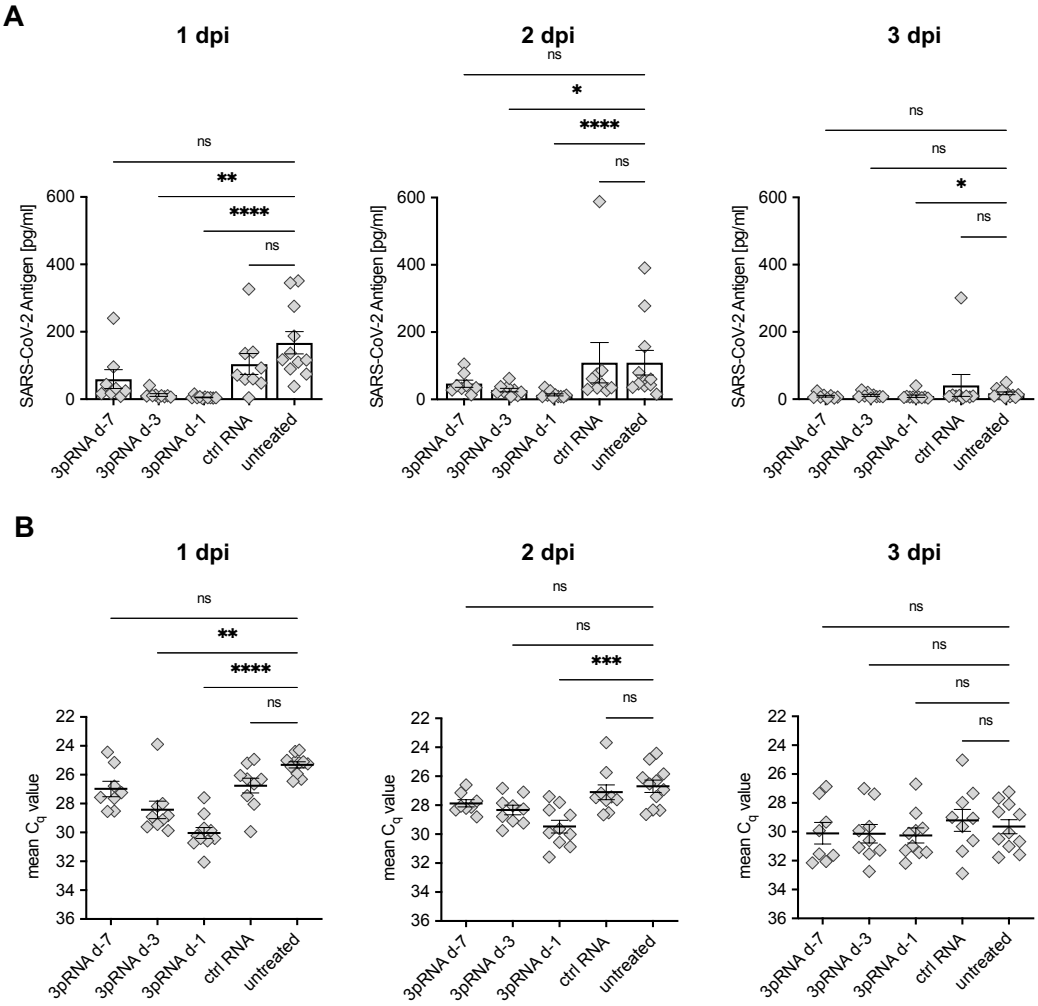

Figure 20: Prophylactic RIG-I ligand treatment inhibits early viral replication in the upper respiratory tract of SARS-CoV-2-infected K18-hACE2 mice. Oropharyngeal swabs were collected on 1-3 dpi from SARS-CoV-2-infected K18-hACE2 mice upon prophylactic 3pRNA treatment as shown in **Figure 18**. (A) SARS-CoV-2 antigen ELISA and (B) expression of SARS-CoV-2 viral RNA by qPCR was assessed in oropharyngeal swab material on 1-3 dpi. Data are shown as mean ± SEM (3pRNA d-7 n=8, 3pRNA d-3 & ctrl RNA n=9, 3pRNA d-1 n=10, untreated n=11). Data are pooled from two independent experiments. Statistical significance was calculated by non-parametric Kruskal−Wallis test and Dunn's multiple testing. * $p<0.05$, ** $p<0.01$, *** $p<0.001$, **** $p<0.0001$.

It is likely that the inhibition of the early viral replication in the upper respiratory tract leads to a diminished viral transmission into the lungs and is responsible for the alleviated disease outcome and survival of 3pRNA-treated mice, as demonstrated in the previous chapter. Therefore, viral burden in the lungs of SARS-CoV-2-infected mice collected at the time point of death or at the end of the observation period (13 dpi) as shown in **Figure 18** was assessed. Of note, owing to the prolonged survival of RIG-I ligand-treated mice, as indicated in the Kaplan-Meier curve (**Figure 18C**), the endpoint and organ collection of

these animals was at a later time point (> 6-13 dpi) than that of control animals (4-6 dpi). qPCR analysis revealed that the 3pRNA pre-treatment uniformly reduced the viral burden in the lungs compared to the untreated group and reached significance in the d-1 group (**Figure 21A**). Despite being non-significant, 3pRNA conferred substantial reduction of viral loads in the lungs of mice treated seven and three days prior to the infection as well. All surviving animals showed negligible levels of viral RNA indicating that these mice showed complete clearance of viral infection within 13 days. Interestingly, when plotted separately from surviving animals, non-surviving animals receiving 3pRNA prophylaxis one day prior to infection presented significantly reduced viral genomic RNA expression compared to untreated animals (**Figure 21B**).

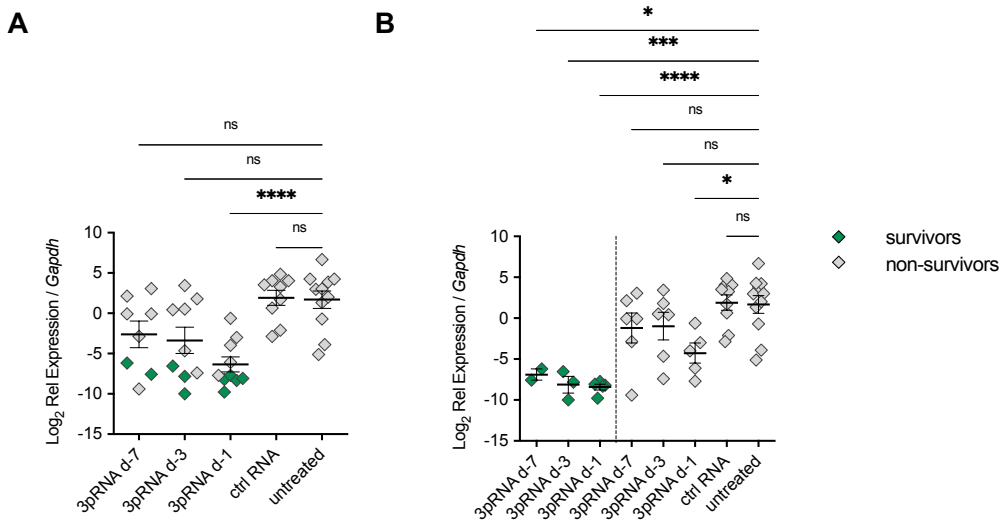

Figure 21: 3pRNA prophylaxis significantly reduces viral transcript levels in the lungs of SARS-CoV-2-infected mice at the time point of death. RNA was isolated from the lungs of SARS-CoV-2-infected K18-hACE2 mice upon 3pRNA prophylactic treatment as presented in **Figure 18** at the time point of death or on 13 dpi. SARS-CoV-2 gene expression in the lungs were quantified by qPCR relative to murine *Gapdh* expression. Animals were separated according to the treatment (A) or according to the treatment and survival/non-survival during the course of experiment (B). Data are shown as mean ± SEM (3pRNA d-7 n=8, 3pRNA d-3 & ctrl RNA n=9, 3pRNA d-1 n=10, untreated n=11). Statistical significance was calculated by one-way ANOVA and Dunnett's multiple testing. * p<0.05, ** p<0.01, *** p<0.001, **** p<0.0001.

Likewise, immunohistochemical staining of SARS-CoV-2 nucleocapsid protein in lung tissue of untreated and ctrl RNA-treated animals showed widespread SARS-CoV-2 staining over the whole section analyzed with most staining localized in the alveolar region (**Figure 22A)**. Correspondingly, these sections were translated to high scores (**Figure**

22B). In contrast, lungs from mice treated with 3pRNA that required euthanasia during the experiment (3pRNA-treated non-survivor) revealed the partial inhibition of viral spread by RIG-I stimulation as indicated by the lower presence of SARS-CoV-2 staining throughout the tissue (**Figure 22A**). Lung sections of 3pRNA-treated mice surviving the infection (3pRNA-treated survivor) revealed the complete clearance of SARS-CoV-2 infection by the absence of visible staining. Despite the different individual outcome of survival, pre-treatment with 3pRNA one day prior to the viral challenge led to significantly lower scores (**Figure 22B).** Finally, scores weakly correlated with the results of the qPCR analysis (**Figure 22C**, r= 0.3479, p <0.05).

Collectively, a single dose of 3pRNA prophylaxis effectively suppressed the early viral replication in the upper respiratory tract which led to a lower manifestation of viral infection in the lungs, ameliorating the disease outcome even independently of the survival of the mouse.

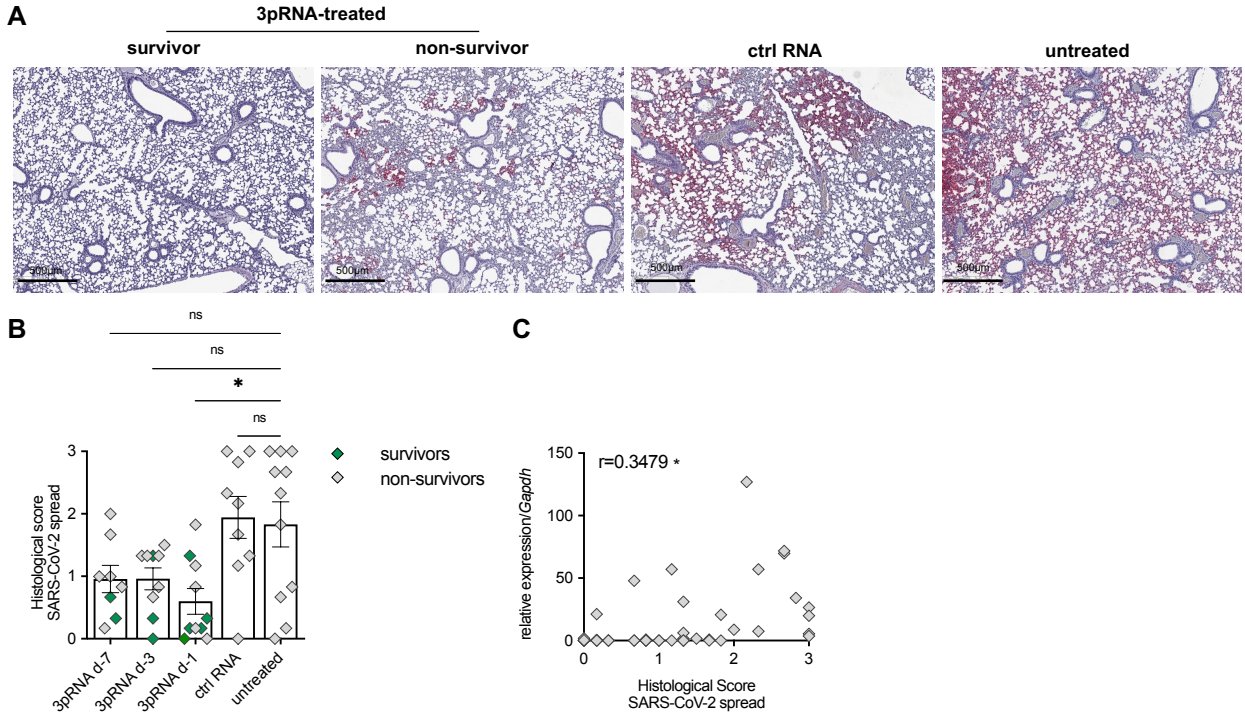

Figure 22: RIG-I prophylaxis inhibits viral spread into the lungs of SARS-CoV-2-infected mice at the time point of death demonstrated by immunohistochemical analysis. Lungs were collected for immunohistochemical analysis from SARS-CoV-2-infected K18-hACE2 mice upon 3pRNA prophylactic treatment as shown in **Figure 18** at the time point of death or on 13 dpi. (A) Representative pictures and (B) scoring of immunohistochemical staining of the SARS-CoV-2 nucleocapsid protein in lung sections. Data are shown as mean + SEM (3pRNA d-7 n=8, 3pRNA d-3 & ctrl RNA n=9, 3pRNA d-1 n=10, untreated n=11) and are pooled from two independent experiments. Statistical

significance was calculated by non-parametric Kruskal−Wallis test and Dunn's multiple testing. (C) Correlation between histological scores of SARS-CoV-2 spread (x-axis) and relative SARS-CoV-2 RNA expression values as seen in **Figure 21** (y-axis) in the lungs. A normal distribution of values was assumed and for statistical analysis the Pearson coefficient was calculated as indicated (n=47). * p<0.05, ** p<0.01, *** p<0.001, **** p<0.0001.

3.5.3. Prophylactic 3pRNA treatment reduces viral burden in the brain of SARS-CoV-2-infected K18-hACE2 mice at the time point of death

In contrast to the initial observation of considerable heterogeneity in the severity of viral burden in the brain of SARS-CoV-2-infected mice on day 4 post infection (**Figure 15C**), the majority (14/17) of non-surviving 3pRNA- treated animals showed high abundance of viral burden in the brain (**Figure 23A and Figure 23B**). Nevertheless, all surviving 3pRNA-treated animals presented negligible viral RNA levels (**Figure 23B**) indicating that they were completely protected from viral spread into the brain. Conjointly, this led to significantly reduced viral burden in the brain of mice treated with 3pRNA one day prior to the infection (**Figure 23A**). Thus, the clinical manifestation of viral infection in the brain might lead to a different survival outcome in SARS-CoV-2-infected 3pRNA-treated K18-hACE2 mice.

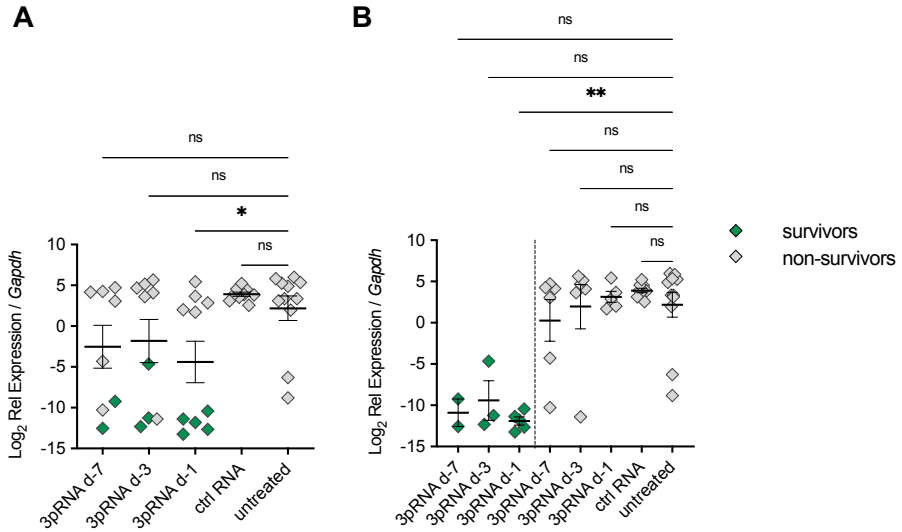

Figure 23: 3pRNA prophylaxis significantly reduces viral RNA gene expression levels in the brain of SARS-CoV-2-infected mice at the time point of death. RNA was isolated from the brain of SARS-CoV-2-infected mice upon 3pRNA prophylactic treatment as presented in **Figure 18** at the time point of death or on 13 dpi. SARS-CoV-2 expression in the brain was assessed by qPCR relative to murine *Gapdh* expression. (A) Animals were separated according to the treatment or (B) according to treatment and survival/non-survival during the course of experiment. Data are shown as mean ± SEM (3pRNA d-7

n=8, 3pRNA d-3 & ctrl RNA n=9, 3pRNA d-1 n=10, untreated n=11). Statistical significance was calculated by non-parametric Kruskal-Wallis test and Dunn's multiple testing. * p<0.05, ** p<0.01, *** p<0.001, **** p<0.0001.

Immunohistochemical SARS-COV-2 nucleocapsid staining of brain sections further revealed a broad distribution of viral infection throughout all brain areas except the cerebellum in non-surviving mice (**Figure 24A**). The majority (11/16) of non-surviving animals presented high scores that did not differ between 3pRNA-treated and untreated animals (**Figure 24B**). In contrast, all surviving 3pRNA-treated animals did not show any SARS-COV-2 nucleocapsid staining throughout the whole section and thus were translated to low scores. Again, scoring of the immunohistochemical staining of brain sections moderately correlated with the qPCR analysis even more closely than that of the lung tissues (**Figure 24C,** r = 0.5488, p <0.0001).

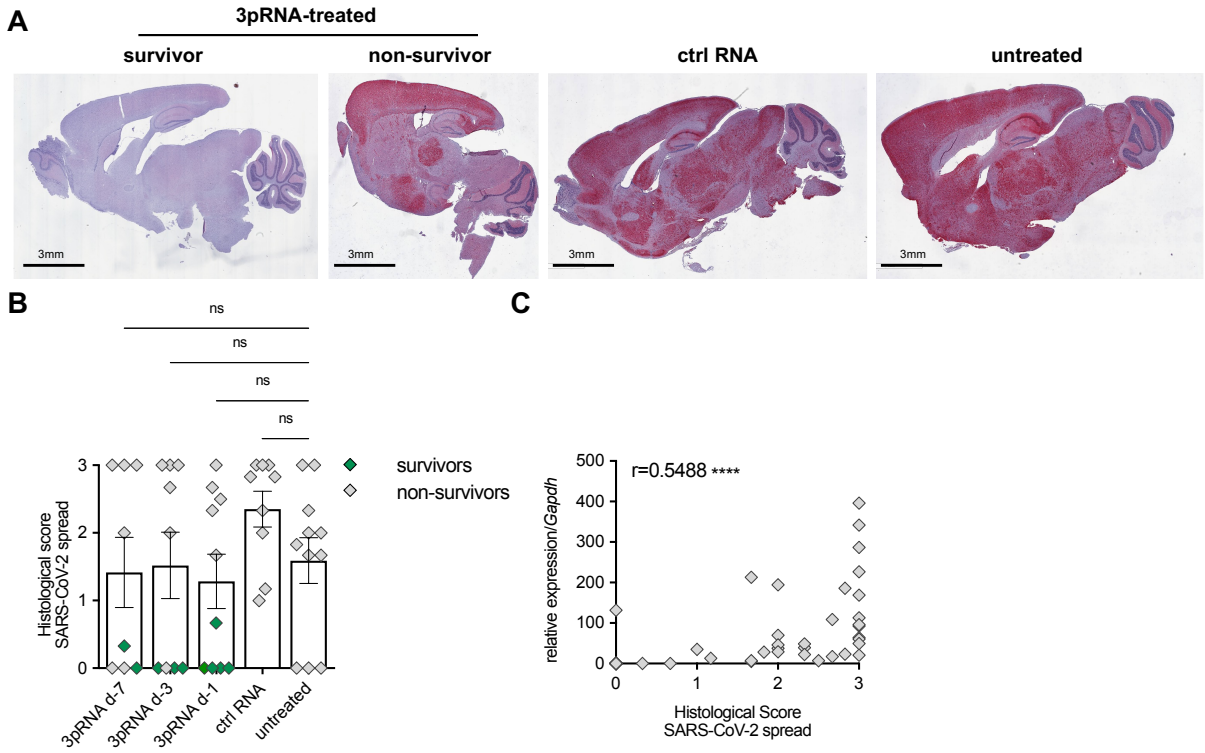

Figure 24: Incomplete penetrance of viral infection into the brain after prophylactic 3pRNA treatment of SARS-CoV-2-infected mice at the time point of death. Brains were collected for immunohistochemical analysis from SARS-CoV-2-infected K18-hACE2 mice upon 3pRNA prophylactic treatment as shown in **Figure 18** at the time point of death or on 13 dpi. (A) Representative pictures and (B) scoring of immunohistochemical staining of the SARS-CoV-2 nucleocapsid protein in brain sections. Data are shown as mean ± SEM (3pRNA d-7 n=8, 3pRNA d-3 & ctrl RNA n=9, 3pRNA d-1 n=10, untreated n=11) and are pooled from two independent experiments. Statistical significance was calculated by non-parametric one-way ANOVA (Kruskal−Wallis test) and Dunn's multiple

testing. (C) Correlation between histological scores of SARS-CoV-2 spread (x-axis) and relative SARS-CoV-2 RNA expression values (**Figure 23**) in the brain. A normal distribution of values was assumed and for statistical analysis the Pearson coefficient was calculated as indicated (n=47). * p<0.05, ** p<0.01, *** p<0.001, **** p<0.0001.

3.5.4. Correlation between viral burden in the lungs and brain and the time point of death in 3pRNA-pre-treated K18-hACE2 mice

The prophylactic treatment with 3pRNA prolonged the time until onset of disease in SARS-CoV-2-infected mice (**Figure 18**). However, some of them still developed signs of poor condition as described before (data not shown) leading to their euthanasia during the observation period. This led to the speculation that the underlying cause of this morbidity and mortality might be due to a late viral penetrance to the brain and that this distinguished them from surviving mice and from mice that succumb to the infection at early time points after infection. Therefore, the individual SARS-CoV-2transcript levels in the lungs and brain as presented in **Figure 21** and **Figure 23** were plotted against the time point of death independent of the treatment of the mice. Correlation revealed that the highest viral burden in the lungs was seen in mice that died early after infection (day 4 to day 5 post infection) and decreased the later the animal succumbed to the infection (**Figure 25A**). Likewise, mice that died early after infection (until day 8 post infection) also demonstrated high viral abundance in the brain (**Figure 25B**). In contrast, 2/3 animals that reached the endpoint criteria on day 9 and 11 post infection exhibited no to low viral abundance in both the lungs and the brain (**Figure 25A** and **Figure 25B**). As shown in **Figure 25C**, viral RNA expression in the lungs moderately correlated to those measured in the brain. Hence, despite being speculated, high viral titers in the brain did not separate survivors from non-surviving animals upon RIG-I treatment.

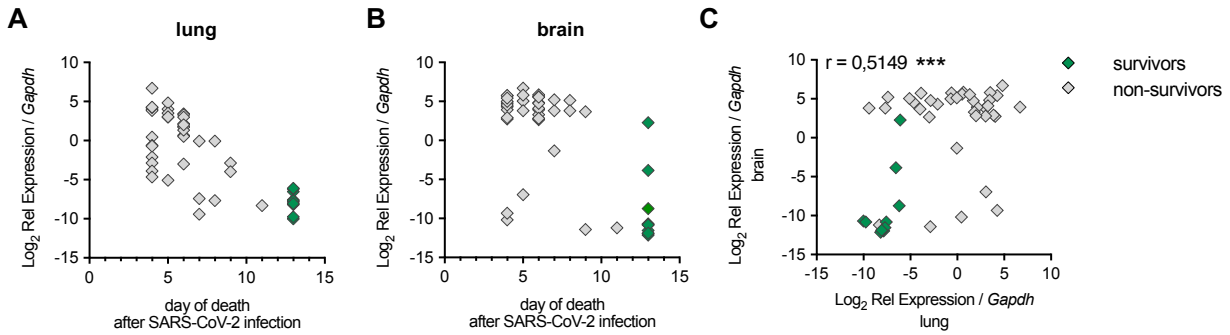

Figure 25: Correlation analysis between viral burden in the lungs and brain of SARS-CoV-2-infected mice at the time point of death. Graphs show the SARS-CoV-2 RNA expression values in the lungs (A) and brain (B) plotted against the time point of death of the individual mouse independent of their treatment (values are adapted from **Figure 21** and **Figure 23**). Data are shown as the mean ± SEM (survivors n=10, d4 n=12, d5=5, d6 n=12, d7 n=3, d8=2, d9=2, d11=1). (C) Correlation between relative SARS-CoV-2 RNA expression values in the lungs (x-axis) and relative SARS-CoV-2 RNA expression values in the brain (y-axis). A normal distribution of values was assumed and for statistical analysis the Pearson coefficient was calculated as indicated (n=47). * p<0.05, ** p<0.01, *** p<0.001, **** p<0.0001.

3.5.5. 3pRNA treatment provides superior protection from SARS-CoV-2 infection to type I interferons in K18-hACE mice

The potent protection of RIG-I against viruses primarily relies on the induction of type I IFNs. This raises the question whether RIG-I stimulation is superior to the administration of type I IFNs in protecting against SARS-CoV-2 infections when applied in *in vivo* models of infection. Therefore, K18-hACE2 mice were i.v. treated with a single dose of $2x10^5$ U universal recombinant IFNα(A/D) (IFNα) or 20 µg 3pRNA one day prior to the lethal SARS-CoV-2 infection with $5x10^4$ PFU (**Figure 26A**). The dose of $2x10^5$ U IFNα (877 ng) was translated from the endogenous serum levels of type I IFN induced upon i.v. injection with 20 µg of 3pRNA (**Figure 10D**).

IFNα treatment showed no level of protection against the lethal infection and led to the comparable survival of IFNα-treated animals to untreated animals (**Figure 26B**). As shown before (**Figure 18**), mice pre-treated with 3pRNA showed prolonged survival as indicated by the right shift of the Kaplan-Meier curve (**Figure 26B**). In contrast to our initial observations, only 1/7 3pRNA-treated mice (14%) survived the infection compared to 5/10 mice (50 %) treated with 3pRNA one day prior to the infection (**Figure 18C**). 3pRNA-treated animals showed high daily weight variabilities that were absent in the IFNα-treated and untreated group (**Figure 26C**). Additionally, serum of the surviving 3pRNA-treated

animal revealed the presence of significant anti-SARS-CoV-2 IgG antibody titers at the end of the observation period (**Figure 26D**).

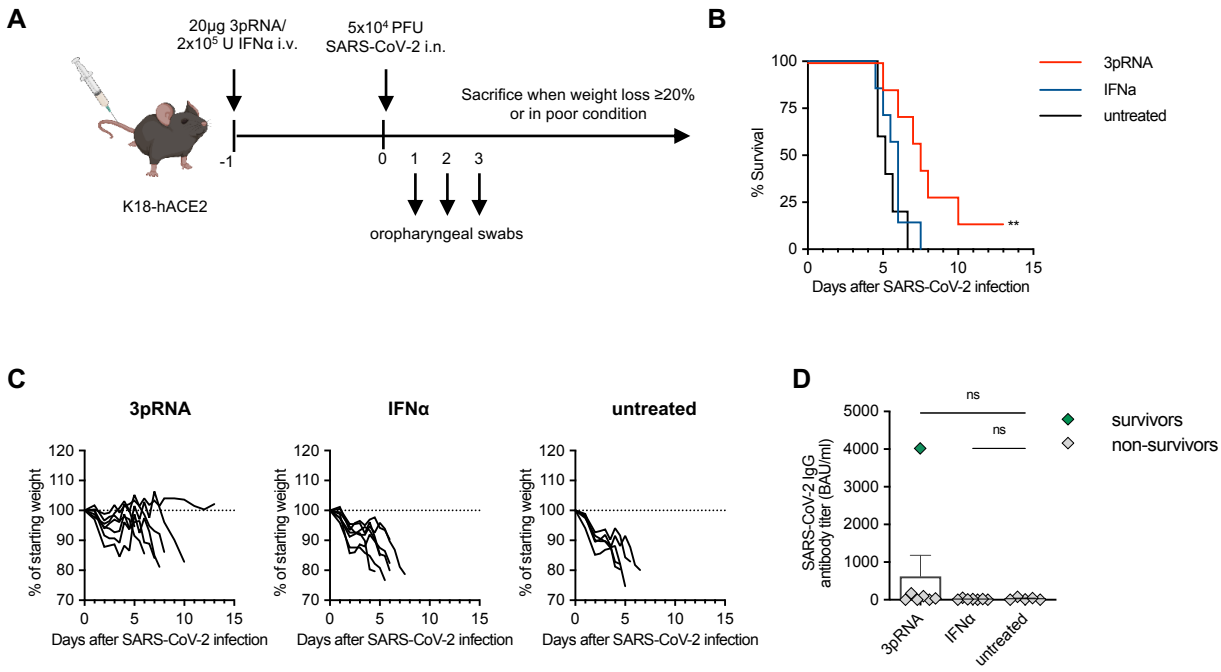

Figure 26: Prophylactic RIG-I ligand treatment is superior to type I IFNs in protecting K18-hACE2 mice from lethal SARS-CoV-2 infections. (A) Experimental setup. Transgenic K18-hACE mice were i.v. treated one day prior to a lethal i.n. SARS-CoV-2 infection (5x10^4 PFU) with a single dose of 20 µg 3pRNA complexed to *in vivo*-JetPEI or 2x10^5 U recombinant universal IFNα(A/D). Oropharyngeal swabs were collected on 1-3 dpi. Disease progression and weight was monitored daily until animals reached the endpoint criteria or day 13 post infection. (B) Kaplan-Meier survival curve of the SARS-CoV-2- infected mice. (C) Individual weight loss development curve of each SARS-CoV-2- infected mice. (D) Quantification of anti-SARS-CoV-2 specific IgG antibody titers in sera of SARS-CoV-2-infected animals. Data are shown as mean ± SEM (3pRNA and IFNα n=7, untreated n=5). Statistical significance was calculated by log-rank Mantel−Cox test (B) and non-parametric Kruskal−Wallis test with Dunn's multiple testing (D).** p<0.01.

3pRNA significantly reduced early viral replication in the upper respiratory tract as indicated by lower levels of SARS-CoV-2 viral antigens and SARS-CoV-2 transcript levels in oropharyngeal swab material taken on day 1 and day 2 post infection (**Figure 27**). For IFNα- treatment a trend towards viral inhibition was observed. This was not statistically significant which could be due to the small sample size used, suggesting that statistical significance might be reached with higher number of mice used for each treatment.

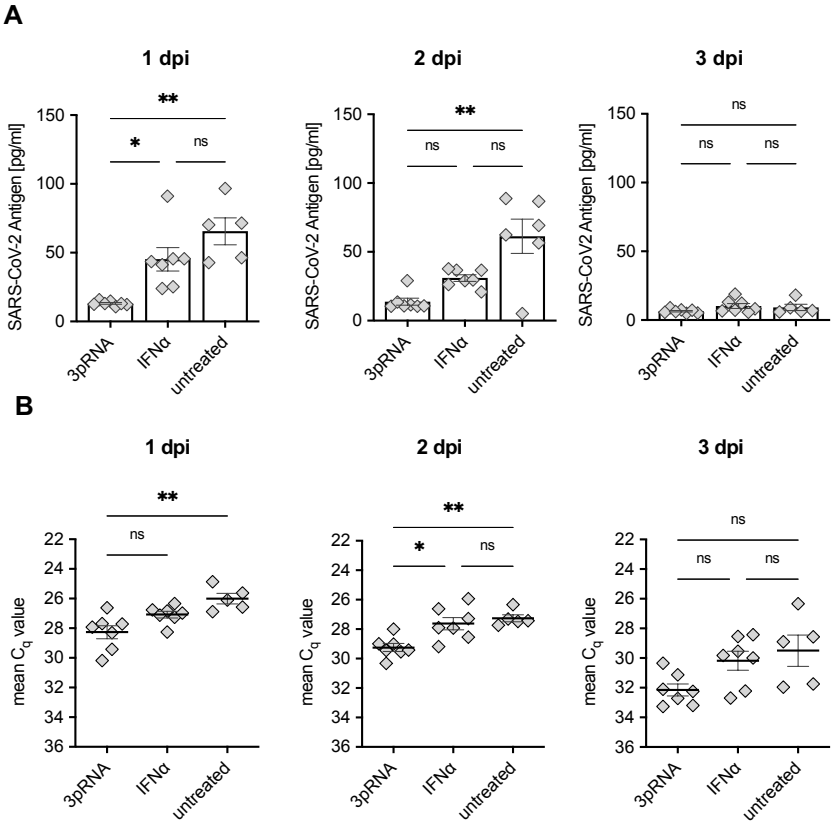

Figure 27: 3pRNA stimulation, but not IFNα treatment, inhibits early viral replication in the upper respiratory tract of SARS-CoV-2-infected K18-hACE2 mice. Oropharyngeal swabs were collected on 1-3 dpi from SARS-CoV-2-infected K18-hACE2 mice upon prophylactic 3pRNA or IFNα treatment as shown in **Figure 26**. (A) SARS-CoV-2 antigen ELISA and (B) expression of SARS-CoV-2 viral RNA qPCR was assessed in oropharyngeal swab material on 1-3 dpi. Data are shown as mean ± SEM (3pRNA and IFNα n=7, untreated n=5). Statistical significance was calculated by Kruskal−Wallis test and Dunn's multiple testing. * p<0.05, ** p<0.01, *** p<0.001, **** p<0.0001.

Gene expression analysis of the lungs of these animals at their individual time of death or on day 13 post infection revealed significant reduction in viral burden in the lungs of 3pRNA-treated animals, but not in IFNα- treated animals (**Figure 28A**). No differences in the viral RNA levels in the brain between the treatment groups (**Figure 28B**). The surviving 3pRNA-treated animal revealed no signs of infection by showing SARS-CoV-2 gene expression levels at the detection limit.

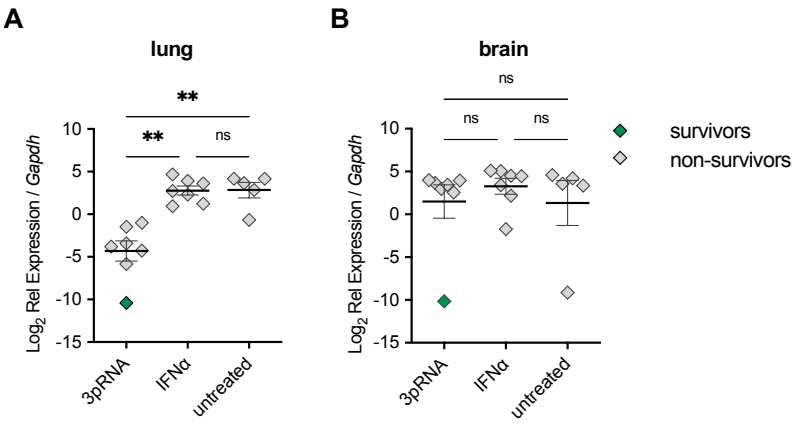

Figure 28: Respiratory protection against SARS-CoV-2 is not efficiently induced by IFNα treatment in SARS-CoV-2-infected K18-hACE2 mice. RNA of lungs and brain were isolated from SARS-CoV-2-infected K18-hACE2 mice upon prophylactic 3pRNA or IFNα treatment as shown in **Figure 26** at the time point of death or on 13 dpi. SARS-CoV-2 RNA expression in the lungs (A) and in the brain (B) was quantified by qPCR relative to *Gapdh* expression. Data are shown as mean ± SEM (3pRNA and IFNα n=7, untreated n=5). Statistical significance was calculated by one-way ANOVA and Dunnett's multiple testing (A) when lognormal distribution was assumed, or by non-parametric Kruskal−Wallis test and Dunn's multiple testing (B). * p<0.05, ** p<0.01, *** p<0.001, **** p<0.0001.

3.6. Therapeutic RIG-I stimulation partially protects mice from lethal SARS-CoV-2 infections

In the previous chapter, the prophylactic efficacy of 3pRNA in protecting mice against otherwise lethal SARS-CoV-2 infections has been demonstrated. Nonetheless, for clinical applications, it is most interesting to investigate whether the therapeutic treatment with RIG-I agonists confers reduced mortality on already established infection in the SARS-CoV-2 mouse model. This might be translated into an early treatment option for SARS-CoV-2-infected individuals at risk in developing severe COVID-19 disease. Accordingly, 3pRNA or ctrl RNA was i.v. injected into SARS-CoV-2- infected mice ($5x10^4$ PFU, i.n.) on day one post infection and repeated on day 4, 7 and 10 post infection (**Figure 29A**). Mice were monitored daily for weight loss and signs of disease and euthanasia criteria were as described before.

While untreated and ctrl RNA-treated animals did not recover from weight loss and uniformly required euthanasia within seven days after infection, the repetitive 3pRNA treatment increased the survival of SARS-CoV-2- infected mice from 0 % in the control groups to 20 % with 2/10 surviving animals in the therapeutic 3pRNA treatment group

(**Figure 29B** and **Figure 29C**). Mice that survived the infection recovered from weight loss and reached again their starting weight within the observation period (**Figure 29C)**. Furthermore, highly specific anti-SARS-CoV-2 antibodies were detected in the sera of the two surviving 3pRNA-treated animals and one non-surviving 3pRNA-treated animal that further showed neutralizing activities against SARS-CoV-2 spike protein (**Figure 29D** and **Figure 29E**). 7/8 non-surviving 3pRNa-treated and all ctrl RNA-treated and untreated animals did not establish any measurable antibody titers due to their early time of death.

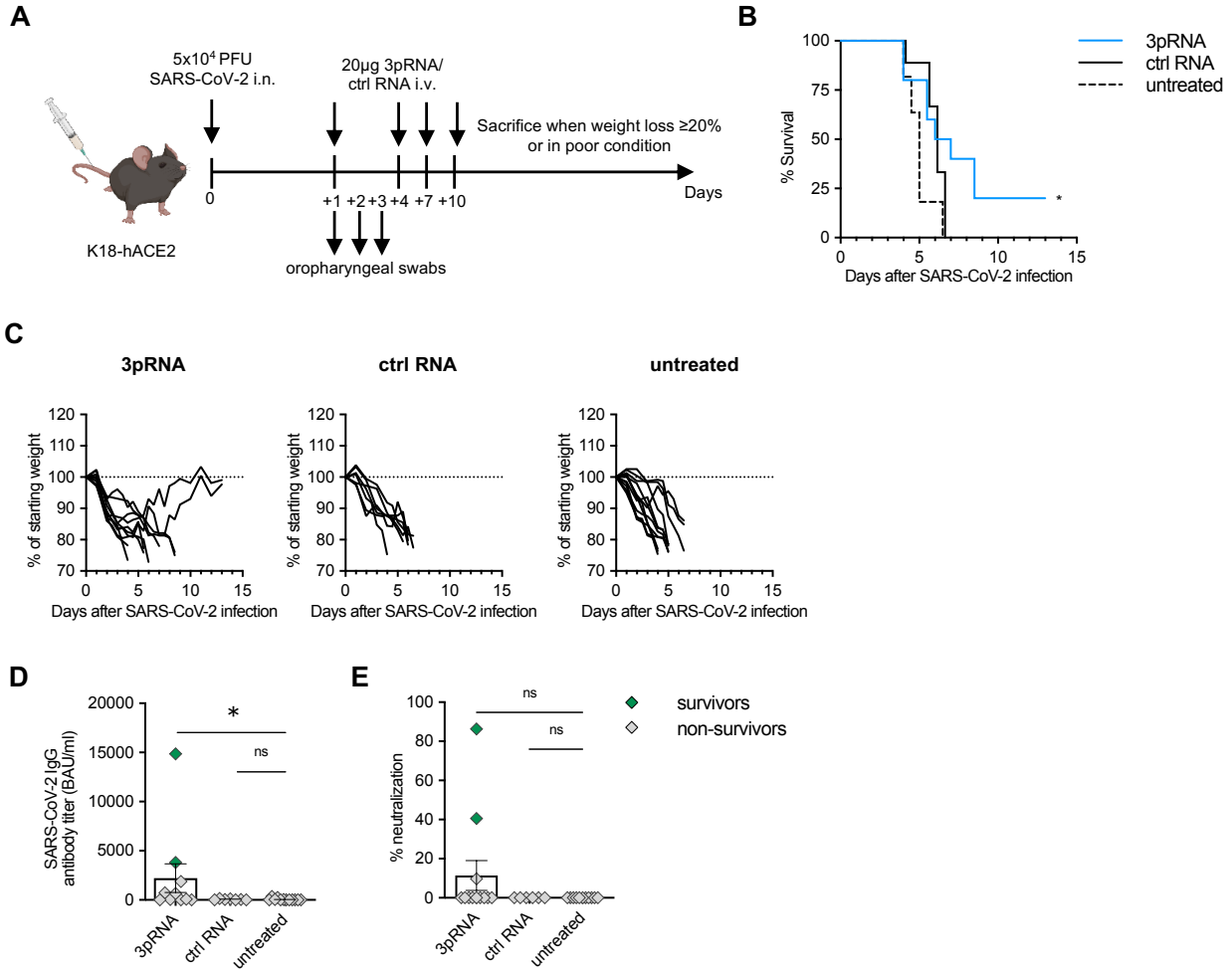

Figure 29: Therapeutic RIG-I ligand treatment confers intermediate level of protection against lethal SARS-CoV-2 infections in K18-hACE2 mice. (A) Experimental setup. Transgenic K18-hACE mice were i.n. infected with 5x10^4 PFU SARS-CoV-2. Starting on day 1 post infection, 20 µg 3pRNA or ctrl RNA complexed to *in vivo*-JetPEI was injected i.v. into the tail and repeated on 4, 7 and 10 dpi. Oropharyngeal swabs were collected on 1-3 dpi. Disease progression and weight were monitored daily until animals reached the endpoint criteria or day 13 post infection. (B) Kaplan-Meier survival curve and (C) individual weight loss development of the SARS-CoV-2- infected mice. (D) Quantification of anti-SARS-CoV-2 specific IgG antibody titers in sera and (E) percent of inhibition of SARS-CoV-2 S1/RBD-hACE2 interaction by sera collected from

SARS-CoV--2-infected animals at the time point of death or at the end of the observation period. of SARS-CoV-2-infected animals collected. Data are shown as mean ± SEM (3pRNA n=10, ctrl RNA n=7, untreated n=11) pooled from two independent experiments. Statistical significance was calculated by log-rank Mantel−Cox test (B) and non-parametric Kruskal−Wallis test with Dunn's multiple testing (D,E). * p<0.05, ** p<0.01, *** p<0.001, **** p<0.0001.

Oropharyngeal swab material was collected on day 1 to day 3 post infection to monitor viral replication upon therapeutic 3pRNA treatment. On day one post infection – prior to the first therapeutic treatment – comparable viral release and replication were detected in all three groups via both ELISA and qPCR, albeit showing relatively heterogenous individual values (**Figure 30**). On day two post infection, SARS-CoV-2 antigens were still detectable in the oropharyngeal swab material in all animals by both ELISA and qPCR, but did not show any differences between the groups either. By day three post infection, no detectable SARS-CoV-2 antigens was visible in the oropharyngeal swabs by ELISA, while viral transcription was still detected.

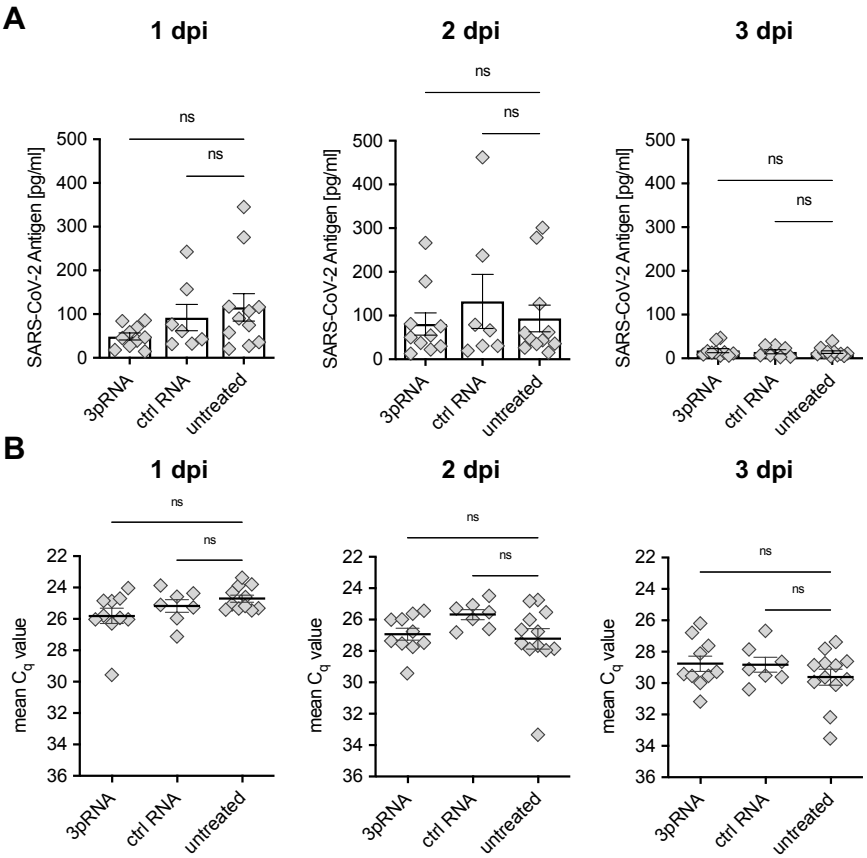

Figure 30: Therapeutic RIG-I ligand treatment does not restrict viral replication at early time points in the upper respiratory tract. Oropharyngeal swabs were collected on 1-3 dpi from SARS-CoV-2-infected K18-hACE2 mice upon therapeutic 3pRNA

treatment as shown in **Figure 29**. (A) SARS-CoV-2 antigen ELISA and (B) expression of SARS-CoV-2 viral RNA in oropharyngeal swab material on 1−3 dpi. Data are shown as mean ± SEM (3pRNA n=10, ctrl RNA n=7, untreated n=11) pooled from two independent experiments. Statistical significance was calculated by non-parametric Kruskal−Wallis test and Dunn's multiple testing. * p<0.05, ** p<0.01, *** p<0.001, **** p<0.0001.

Moreover, the lungs and brain were harvested at the individual time point of death or at the end of the observation period to quantify the viral burden by qPCR (**Figure 31**) and by SARS-CoV-2 immunohistochemical staining of lung and brain sections (**Figure 32**). Compared to untreated animals, the 3pRNA therapeutic treatment showed only a tendency towards the reduction of viral burden in the lungs (**Figure 31A**) and brain (**Figure 31B**) as measured by non-significant lower SARS-CoV-2 transcription. The two surviving 3pRNA-treated animals did not show detectable viral RNA in the lungs.

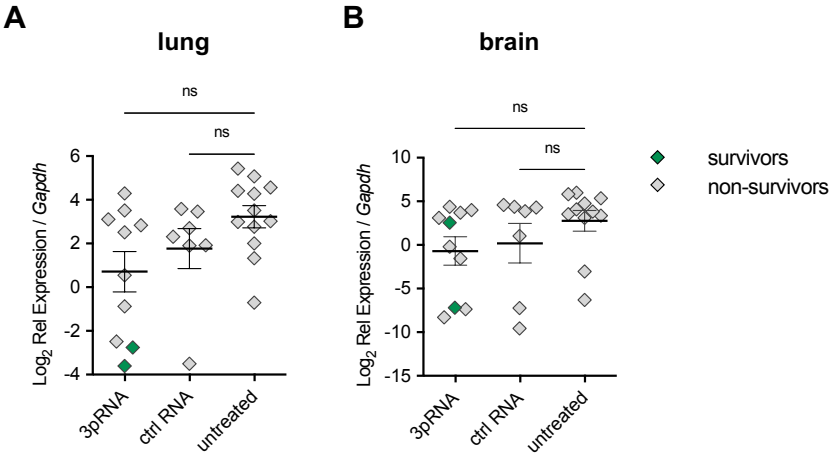

Figure 31: Therapeutic 3pRNA treatment shows a tendency towards reduced viral titers in the lungs and brain of SARS-CoV-2-infected mice at the time point of death. RNA of lungs and brain were isolated from SARS-CoV-2-infected K18-hACE2 mice upon therapeutic 3pRNA treatment as shown in **Figure 29** at the time point of death or on 13 dpi. SARS-CoV-2 viral RNA expression was quantified by qPCR relative to murine *Gapdh* in the lungs (A) and in the brain (B). Data are shown as mean ± SEM (3pRNA n=10, ctrl RNA n=7, untreated n=11) pooled from two independent experiments. Statistical significance was calculated by non-parametric Kruskal−Wallis test with Dunn's multiple testing (D,E). * p<0.05, ** p<0.01, *** p<0.001, **** p<0.0001.

In line with the gene expression analysis, immunohistochemical staining of SARS-CoV-2 nucleocapsid revealed the absence of viral infection in lung (**Figure 32A)** and brain tissue (**Figure 32B)** in the surviving animals, but demonstrating a strong staining in non-surviving treated, ctrl RNA-treated and untreated animals. This led to high scores in the lungs and brain (**Figure 32C** and **Figure 32D**) with moderately and strong correlation between the

qPCR results and the immunohistochemical staining in the lungs and brain, respectively (**Figure 32E** and **Figure 32F**).

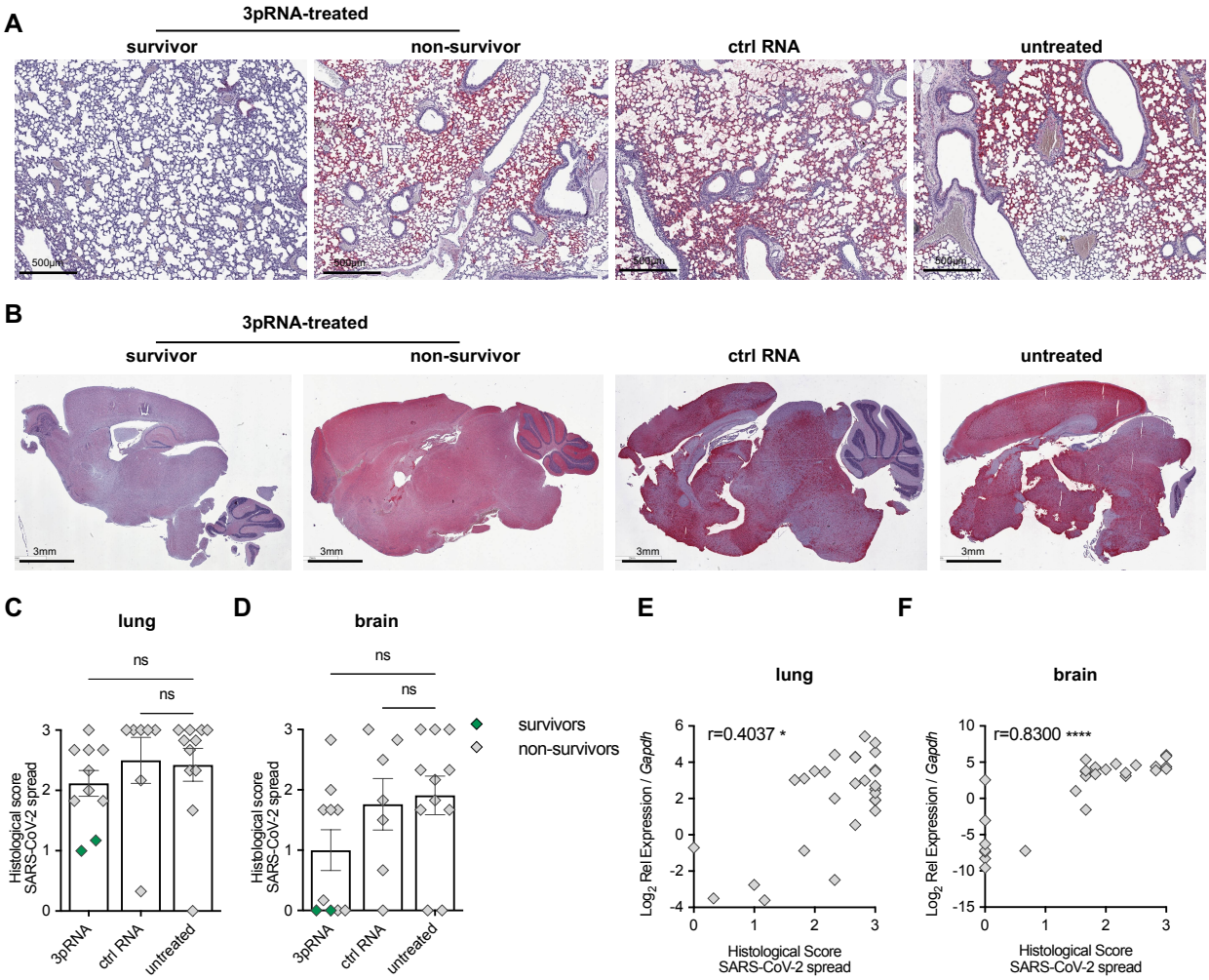

Figure 32: Immunohistochemical staining reveals high viral burden in the lungs and brain in SARS-CoV-2 mice upon therapeutic 3pRNA treatment. Lungs and brain were collected for immunohistochemical analysis from SARS-CoV-2-infected K18-hACE2 mice upon therapeutic 3pRNA treatment as shown in **Figure 29** at the time point of death or on 13 dpi. (A,B) Representative pictures and (C,D) scoring of immunohistochemical staining of the SARS-CoV-2 nucleocapsid protein in lung (A,C) and brain (B,D) sections. Data are shown as mean ± SEM (3pRNA n=10, ctrl RNA n=7, untreated n=11) pooled from two independent experiments. Statistical significance was calculated by non-parametric Kruskal−Wallis test with Dunn's multiple testing (C,D). Correlation of histological scores of SARS-CoV-2 spread (x-axis) and relative expression qPCR values of SARS-CoV-2 expression in the lungs (E) and brain (F) (see **Figure 31**). For statistical analysis, the Spearman coefficient was calculated as indicated (n=28). * p<0.05, ** p<0.01, *** p<0.001, **** p<0.0001.

4. Discussion

4.1. SARS-CoV-2 largely escapes immune recognition by cytosolic innate immune receptors

First of all, I investigated whether SARS-CoV-2 is sensed by RIG-I and MDA5 in immune cells. Several SARS-CoV-2 viral proteins have been shown to interfere with RLR signaling, IFN induction and IFN signaling (Beyer and Forero, 2021; Lei et al., 2020; Wang et al., 2020b) and effectively suppress the induction of type I IFN expression in SARS-CoV-2-infected cells albeit seen upon IAV or Sendai Virus infection (Kouwaki et al., 2021). Thus, to evaluate the full immunostimulatory potency of SARS-CoV-2 RNA without these viral RLR and IFN antagonists present, total RNA from SARS-CoV-2-infected VeroE6 cells was extracted to completely remove (viral) proteins. Transfection of total RNA from SARS-CoV-2- infected cells into human PBMCs (**Figure 6**) and murine dendritic cells (**Figure 7A**) resulted in lower IFNα protein secretion than other common respiratory viruses such as IAV and RSV. Others have shown that total RNA extracted 24 hrs after SARS-CoV-2 infection results in the significant upregulation of *IFNB* transcript levels (Kouwaki et al., 2021; Yin et al., 2021). However, these studies used higher RNA concentrations for transfection compared to our study, as well as qPCR as a readout which is generally more sensitive than cytokine quantitation by ELISA. Lastly, no total RNA isolated from cells infected with other viruses has been used for the transfection in these studies that would allow the direct comparison and the evaluation if the observed responses are high or low.

Additionally I found that recognition of total RNA from SARS-CoV-2-infected cells was dependent on MDA5 in murine dendritic cells (**Figure 7B**) which mirrors published results in human epithelial cells (Yin et al., 2021). Similarly, recognition of direct human epithelial cell infection by SARS-CoV-2 depends predominantly on MDA5 (Sampaio et al., 2021; Yin et al., 2021). On the other hand, RNAi-mediated knock-down of RIG-I and MDA5 in cells or RIG-I$^{-/-}$ and MDA5$^{-/-}$ cells have been shown to significantly abrogate cytokine induction upon SARS-CoV-2 infection suggesting that SARS-CoV-2 is sensed by both RIG-I and MDA5 (Kouwaki et al., 2021; Thorne et al., 2021a). Further *in vitro* and *in vivo* studies are needed to evaluate the exact role of RIG-I and MDA5 in SARS-CoV-2 immune sensing. Collectively, SARS-CoV-2 viral replication intermediates were sensed by MDA5, albeit type I IFN gene expression and protein levels were lower than those induced by IAV

and RSV RNA. The overall low innate response to SARS-CoV-2 provides an interesting subject of debate for the intervention with exogenous RLR ligands to induce a more effective anti-viral resistance and prolonged immune stimulation.

4.2. Systemic and local immune activation in the lungs after i.v. injection of *in vivo*-JetPEI-complexed 3pRNA

The present study aimed to establish anti-viral resistance against SARS-CoV-2 by the application of specific RIG-I agonists in mice. The complexation of RNA with cationic lipid- or polymer-derived carriers mediates effective RNA delivery into the cells as well as stabilization and the protection of RNA from nucleases abundantly present in the blood and skin (Kowalski et al., 2019). In this study, a short blunt-ended dsRNA with a 5' triphosphate (3pRNA) was complexed to *in vivo*-JetPEI, an optimized linear cationic polyethyleneimine (PEI) commonly used as *in vivo* transfection reagent for cytosolic delivery. This complexation has been used in several mouse models of respiratory virus infection (Chiang et al., 2015; Coch et al., 2017; Mao et al., 2022) and in a clinical phase I/II study for the intratumoral application of RIG-I agonists (NCT03739138) (Middleton et al., 2018).

The single i.v. treatment with 3pRNA, but not with ctrl RNA, led to the rapid production of type I IFNs as well as pro-inflammatory cytokines and chemokines into the sera of mice when analyzed 6 hrs after application (**Figure 10B**). In line, other studies have shown that type I IFN production reaches its maximum levels 2-5 hrs post i.v. injection of RIG-I agonists and rapidly declines afterwards (Linehan et al., 2018). Type I IFN production was dose-dependent since 20 µg 3pRNA led to higher IFNα levels in the sera 4 hrs after i.v. injection than 6.25 µg (**Figure 10D**). In line, higher doses of RIG-I agonists lead to more pronounced *Ifna* transcript induction in the spleen of mice 3 hrs after i.v. injection (Linehan et al., 2018). In contrast, CXCL10 production upon the injection with the low and high dose of 3pRNA was indistinguishable, suggesting a plateau level of induction (**Figure 10B** and **Figure 10D**). Gene expression analysis further revealed the significant upregulation of ISGs and cytokines in the lungs, spleen and liver at 6 hrs after i.v. injection with 6.25 µg 3pRNA (**Figure 11**). In line with this finding, studies targeting pancreatic cancer have reported that the systemic delivery of a RIG-I agonist complexed with lipid calcium phosphate nanoparticles predominantly targets the liver, spleen and lung, while only 2 %

of the particles reaches the tumor as measured by biodistribution assay with ^{177}Lu- labeled complexes (Das et al., 2019). Furthermore, fluorescently-labeled RIG-I agonist *in vivo*-JetPEI complexes are preferentially taken up by lung epithelial cells, macrophages and inflammatory monocytes in the lungs upon i.v. injection as shown by flow cytometry (Mao et al., 2022). Therefore, it is likely that the immune effects seen in our study results from the direct delivery of 3pRNA to the lungs, liver and spleen as well.

Flow cytometric analysis of total lung tissue further revealed an influx of NK cells, monocytes and neutrophils into the lungs and broad immune cell activation 6 hrs upon RIG-I agonist administration (**Figure 12** and **Figure 13**). Cell activation after RIG-I stimulation was quantified by the relative frequencies of distinct activation markers on the surface of the immune cells. Increased expression of CD69 on $CD4^+$ and $CD8^+$ T, B and NK cells (**Figure 12B**) as well as on monocytes and interstitial macrophages (**Figure 13**) uncovered the broad immune cell activation upon RIG-I stimulation. Moreover, optimal T cell activation and proliferation requires co-stimulatory signals by the interaction of CD28 on the T cell and CD80 or CD86 on the APC (Goral, 2011). Contrarily, PD1 and its ligand PDL-1 counteract T cell activation by sending co-inhibitory signals to the T cell leading to its exhaustion (Chen and Flies, 2013). Both CD86 and PDL-1 expression was increased on interstitial macrophages and monocytes upon RIG-I stimulation (**Figure 13**). Both proteins are known to be rapidly upregulated in an type I IFN-dependent manner (Sansom, 2000; Sharpe et al., 2007). Alveolar macrophages presented constitutive PDL-1 expression (**Figure 13**) that is consistent with previous studies as well (Sun et al., 2021). Similarly, in line with earlier reports, PD1 expression was induced on $CD4^+$ and $CD8^+$ T cells upon RIG-I stimulation (**Figure 12C**) (Sharpe et al., 2007). The upregulation of both co-stimulatory and co-inhibitory molecules underlines that RIG-I stimulation not only mediates shaping of the anti-viral adaptive immune response, but is involved in maintaining peripheral tolerance and inhibiting immune-mediated tissue damage during the anti-viral response (Sharpe et al., 2007).

Conclusively, the systemic injection of RIG-I agonists complexed to *in vivo*-JetPEI potently targets lung epithelial cells resulting in the establishment of anti-viral resistance. Furthermore, it also directly activates innate immune cells that enables the development of adaptive immunity. Hence, the induction of anti-viral resistance in the lungs is probably

established faster upon RIG-I agonist delivery than upon the natural viral infection that initially reaches only few lung cells and results in local inflammation.

4.3. K18-hACE2 transgenic mice as severe model for COVID-19 disease

In this study, the K18-hACE2 mouse model of SARS-CoV-2 infections was used. Consistently with the initial publication (McCray et al., 2007), transgenic K18-hACE2 mice presented with high expression levels of ACE2 in the lungs, intestines and colon, and intermediate levels in the brain (**Figure 14**). i.n. infection with $5x10^4$ PFU SARS-CoV-2 led to detectable levels of SARS-CoV-2 RNA and antigens in oropharyngeal swabs on day 1 and 2 post infection (**Figure 20**). The measurement of viral load in oropharyngeal swabs is shown to be indicative of active viral replication (Yinda et al., 2021). By day three post infection, viral antigens were no longer detectable suggesting that the infection had been cleared from the upper respiratory tract and had spread to the lower respiratory tract. Indeed, on day 4 post infection, high SARS-CoV-2 viral titers (**Figure 15**) and immunohistochemical staining of SARS-CoV-2 nucleocapsid throughout the tissue (**Figure 16**) were detected in the lungs of untreated SARS-CoV-2-infected animals.

Untreated SARS-CoV-2-infected mice rapidly developed severe signs of disease and showed significant weight loss (**Figure 18D**, **Figure 18E**) and 100 % of animals succumbed to infection within 4 to 6 days after infection (**Figure 18C**). This is in accordance with studies that have used similar inoculation doses (Winkler et al., 2020; Yinda et al., 2021; Zheng et al., 2021), with the notion that lethality of SARS-CoV-2 infection is dose-dependent. High doses (10^5 PFU) of SARS-CoV-2 lead to 100 % lethality in K18-hACE2 mice, while lethality rates of 50-85 % are seen upon the infection with 10^4 PFU SARS-CoV-2 (Yinda et al., 2021; Zheng et al., 2021). At low doses, stark differences in lethality have been observed: While mice infected with 10^3 PFU inoculum showed no signs of disease or lethality in one study (Zheng et al., 2021), 10^3 PFU SARS-CoV-2 inoculum resulted in 100 % lethality in a different study (Mao et al., 2022). Major drawback of this model is the ectopic expression of *ACE2* under the epithelial promoter that does not fully resemble the expression pattern of *ACE2* in humans (Hikmet et al., 2020) and its supraphysiological levels are likely responsible for the disease severity and lethality of this model. Therefore, the high lethality associated with the K18-hACE2 mouse model is in strong contrast to the infection fatality rate in humans that is estimated

to be 0.68-1.6 % (Ioannidis, 2021; Meyerowitz-Katz and Merone, 2020; Streeck et al., 2020).

Besides the high lethality associated with this model, untreated SARS-CoV-2-infected K18-hACE2 mice demonstrated high viral burden in lung tissue at day 4 post infection (**Figure 15**, **Figure 16**) and at the time point of their death (**Figure 21**, **Figure 22**) which is consistent with previous studies (Mao et al., 2022; Winkler et al., 2020; Yinda et al., 2021; Zheng et al., 2021). Moreover, SARS-CoV-2-infected K18-hACE2 mice develop histological aspects of ARDS, including immune cell infiltrates, edema, and lung consolidation. This results in impaired pulmonary function and substantially contributes to morbidity and mortality (Winkler et al., 2020; Yinda et al., 2021) which is consistent with severely SARS-CoV-2- infected patients (Grasselli et al., 2020; Tian et al., 2020; Xu et al., 2020). The majority of untreated mice (9/11) presented with high viral titers in the brain at the time point of death as well (**Figure 23**, **Figure 24**) providing a possible explanation for the occasionally observed motoric impairment in SARS-CoV-2-infected mice that required immediate euthanasia (data not shown). The presence of viral transcripts in the lungs significantly correlated with those detected in the brain (**Figure 25C**). Partial penetrance of viral infection to the brain is described in the K18-hACE2 mouse model as a probable cause of anosmia (Kumari et al., 2021; Winkler et al., 2020; Zheng et al., 2021) and is associated with lethality of this model (Kumari et al., 2021; Song et al., 2021). Likewise, human COVID-19 patients suffer from neurological symptoms and post-mortem studies have demonstrated the neuroinvasion into the central nervous system in patients that died with severe SARS-CoV-2 infection (Helms et al., 2020; Song et al., 2021; Spudich and Nath, 2022).

Since untreated SARS-CoV-2-infected K18-hACE2 mice succumbed to the infection early after the viral challenge, they were not able to establish an adaptive immune response (**Figure 19**). Furthermore, SARS-CoV-2-infected animals presented increased transcript levels of pro-inflammatory cytokines (*Cxcl10*, *Il6*, *Ccl2*) in the lungs and brain on day 4 post infection (**Figure 17**) that is in accordance with previous reports (Winkler et al., 2020). Likewise, hyperinflammation correlates with severe SARS-CoV-2 infections in patients (Blanco-Melo et al., 2020; Hadjadj et al., 2020; Zhou et al., 2020a). For instance, elevated levels of IL-6, IL-10, CCL2 and CXCL10 in sera is seen in severely infected COVID-19 patients (Blanco-Melo et al., 2020; Laing et al., 2020). However, immunomodulatory

agents such as the synthetic corticosteroid dexamethasone show only moderate effects in reducing mortality in hospitalized severely ill COVID-19 patients receiving oxygen therapy by suppressing the inflammatory response (Angus et al., 2020; RECOVERY Collaborative Group et al., 2021). While immunosuppression seems to be helpful in the late stage of infection in the presence of hyperinflammation, this intervention is potentially harmful during the early phase of disease in which innate and adaptive immunity are established. Supporting this hypothesis, the daily treatment with nonsteroidal anti-inflammatory drugs (NSAID, e.g. meloxicam, ibuprofen) of SARS-CoV-2-infected K18-hACE2 mice starting one day prior to infection has not shown any effect on the viral burden or weight loss of infected mice, but reduces the production of cytokines in the serum and impairs the development of neutralizing anti-SARS-CoV-2 antibodies (Chen et al., 2021), indicating that early NSAID treatments dampen the establishment of potent adaptive anti-viral immune response and may contribute to COVID-19 pathogenesis.
Collectively, the K18-hACE2 mouse model is the most stringent model so far to evaluate the therapeutic success of potential SARS-CoV-2 countermeasures due to the clear endpoint parameters of survival/lethality, high viral titers and cytokine production. Yet, careful evaluations must be made in the direct comparison of the therapeutic efficacy of anti-viral drugs tested in different studies.

4.4. Recombinant interferons for COVID-19 therapy

Key factor in the establishment of a robust anti-viral response against SARS-CoV-2 seems to be the early production of endogenous type I and type III IFNs that are antagonized by several nonstructural and accessory proteins of SARS-CoV-2 (Beyer and Forero, 2021; Blanco-Melo et al., 2020; Hadjadj et al., 2020; Lei et al., 2020; Zhang et al., 2020b). Susceptibility of SARS-CoV-2 to type I IFNs was evaluated *in vitro* by the exogenous administration of type I IFNs to target cells prior to SARS-CoV-2 infection. The lung epithelial cell line A549 expressed only low endogenous levels of ACE2 and TMPRSS2 (**Figure 8A**), the two target proteins of the SARS-CoV-2 spike protein required for viral entry (Rebendenne et al., 2021; Thorne et al., 2021a). Therefore, human ACE2 and TMPRSS2 were stably introduced in these cells via lentiviral transduction (**Figure 8A**) to allow for efficient SARS-CoV-2 infection (**Figure 9B**) as demonstrated before (Rebendenne et al., 2021). SARS-CoV-2 was highly susceptible to recombinant universal

IFNα pre-treatment *in vitro*, as determined by the significant reduction of viral transcript levels in the cells and of SARS-CoV-2 antigen levels in the supernatants (**Figure 9B** and **Figure 9C**). Consistent with these results, susceptibility of SARS-CoV-2 to the pre-treatment with type I IFNs and type III IFNs has been shown in epithelial cells *in vitro* (Lokugamage et al., 2020; Stanifer et al., 2020).

Systemic administration with $2x10^5$ U recombinant IFNα in K18-hAEC2 mice one day prior to the i.n. SARS-CoV-2 infection with $5x10^4$ PFU failed to provide protection from morbidity and lethality (**Figure 26**) and did not reduce viral burden in the lungs and brain (**Figure 28**). The dose of recombinant IFNα used for the systemic administration was translated from type I IFN production into sera of mice 4 hrs after 3pRNA injection (**Figure 10D**). In contrast, similar doses of IFNα have been shown to increase the survival rate of 40 % of untreated mice to 60 % survival in the same mouse model (Mao et al., 2022). However, it is important to mention that a 100-fold lower infectious dose of SARS-CoV-2 was used in this study. Likewise, i.n. administration of $2x10^5$U IFNα 3 hrs prior to the infection with $2.5x10^4$ PFU SARS-CoV-2 reduces mortality rates to 50 % (Humphries et al., 2021). IFNα pre-treatment resulted in lower viral burden in the upper respiratory tract on day one and two post infection, however this was not significant (**Figure 27**) indicating that the type I IFN used was functional and that the lack of protection observed in this study was attributed to the high virus inoculation dose compared to the Mao et al. study (Mao et al., 2022). One could also speculate that the anti-viral immune response induced by the IFNα treatment had already declined one day after the treatment, when the mice were infected. This is suggested by an *in vivo* study that demonstrates that higher doses of universal recombinant IFNα(A/D) are needed to provide protection from lethal EMCV infection in mice, the longer the time between the prophylactic i.v. injection of IFNα and the EMCV inoculation (Sim and Cerruti, 1987). While only 870 U recombinant IFNα is required to protect 50 % of mice from a lethal EMCV infection when given 6 hr prior to the virus challenge, $1.7x10^4$ U or $>1x10^5$ U recombinant IFNα is needed when given 24 hrs or 48 hrs prior to infection, respectively (Sim and Cerruti, 1987). This can be indicative for the protective effect of IFNα against SARS-CoV-2 infections as well. Furthermore, it is also important to note that PEGylated forms of human IFNα and IFNβ are used in the clinics that show increased serum half-life, reduced clearance and increased bioavailability compared to the non-PEGylated IFNs (Foster, 2004). Since no PEGylated

mouse IFNs are readily available, both studies (this study and (Mao et al., 2022)) have used the commercially available unmodified universal recombinant IFNα(A/D) that acts on both the human and murine IFNAR.

For SARS-CoV-2, early treatments with PEG-IFNα2, PEG-IFNβ or PEG-IFNλ accelerate the recovery of severely infected COVID-19 patients, but not of moderately ill patients, and are associated with a reduced viral burden and inflammation and in-hospital mortality (Alavi Darazam et al., 2021; Feld et al., 2021; Pandit et al., 2021; Wang et al., 2020a; Zhou et al., 2020c). However, the therapeutic window of IFN therapy against COVID-19 is considered to be relatively narrow since late treatments with IFNs delay the recovery of COVID-19 patients and increase mortality (Wang et al., 2020a), presumably due to an increased inflammation (Alavi Darazam et al., 2021; Sleijfer et al., 2005). Additionally, repeated administration of recombinant IFNs frequently (2-24 %, depending on the PEG-IFN used, dosage and dose frequency) leads to the development of neutralizing auto-antibodies against type I IFNs within 3-18 months after treatment start that may diminish their therapeutic efficacies (Giovannoni, 2002; Matsuda et al., 2012). In parallel, >10 % of patients with life-threatening COVID-19 infections are presented with neutralizing autoantibodies against type I IFNs even prior to the infection and render them unavailable for type I IFN therapy (Bastard et al., 2020; Zhang et al., 2020b). Therefore, the clinical usage of type I IFNs should be kept to a minimum, since the absence of neutralizing anti-type I IFN antibodies likely provides an important advantage for the induction of immune responses against future viral infections.

4.5. Clinical potential of RIG-I agonists as prophylaxis and treatment option against SARS-CoV-2 infections

In this study, the potency of RIG-I agonists to protect against SARS-CoV-2 infections was evaluated *in vitro* and *in vivo* in comparison to recombinant IFNα. In SARS-CoV-2 permissive A549* cells (A549 cells expressing ACE2 and TMPRSS2), prophylactic treatment with 3pRNA was superior to type I IFNs in inhibiting SARS-CoV-2 replication and release (**Figure 9B** and **Figure 9C**) and in enhancing IFN-inducible anti-viral cytokine and protein production *in vitro* in the absence (**Figure 3B**) and in the presence of SARS-CoV-2 infection (**Figure 9D**). Additionally, a single systemic 3pRNA prophylactic treatment conferred potent *in vivo* protection against a lethal SARS-CoV-2 challenge by

reducing the viral burden and inflammation in the lungs during the active course of infection (**Figure 15**, **Figure 16**, **Figure 17**) as well as by substantially decreasing morbidity and mortality of infected mice (**Figure 18C**). The greatest level of protection and reduction of viral titers in the lungs was achieved when RIG-I agonist was given one day prior to infection (**Figure 15**, **Figure 18C**, **Figure 21**). However, the single 3pRNA treatment seven days prior to infection resulted in a lower but clearly detectable protection from mortality as well, indicating a relatively long prophylactic treatment window (**Figure 18C**). Consistently, the prophylactic potency of RIG-I agonists against SARS-CoV-2 infections has been only recently demonstrated in the K18-hACE2 mouse model as well (Mao et al., 2022). In contrast to the 5' triphosphate 24 bp long blunt end dsRNA used in this study, a 5' triphosphate stem-loop duplex RNA of 14 bp length (SLR14) has been used in the Mao et al study (Linehan et al., 2018; Mao et al., 2022). Nevertheless, in K18-hACE2 mice SLR14 injected i.v. 16, 4 or 2 hrs prior to the i.n. infection with 10^3 PFU SARS-CoV-2 leads to 80-100 % survival of treated animals compared to 100 % lethality in untreated mice. Despite the usage of comparable doses of RIG-I agonists (15µg vs 20µg), it should be pointed out that the 100-fold lower virus inoculation dose as well as the different treatment regimen relative to the infection (16 hrs to 2 hrs vs 7 to 1 day prior infection) in the Mao study is likely accountable for the superior protection of their RIG-I agonist against lethality compared to the lethality reported in this study with 3pRNA (Mao et al., 2022) (**Figure 18C**). Similarly, RIG-I stimulation elicited the significant reduction of viral titers and inflammation in the lungs during the active course of infection (**Figure 15**, **Figure 17**) which is also reported by Mao et al (Mao et al., 2022).

Furthermore, surviving 3pRNA-treated SARS-CoV-2-infected animals were sacrificed at the end of the observation period (13 dpi) and showed no longer signs of active infection by low numbers of SARS-CoV-2 transcripts in the lungs and brain (**Figure 21**, **Figure 23**) and by the lack of SARS-CoV-2 nucleocapsid staining in lung and brain tissue (**Figure 22**, **Figure 24**). Furthermore, they developed a strong adaptive immune response, as indicated by high anti-SARS-CoV-2 specific neutralizing antibody titers (**Figure 19**). In contrast, untreated animals succumbed to infection prior to the establishment of adaptive immunity due to high viral burden in the lungs and brain (**Figure 21** to **Figure 24**). This demonstrated that 3pRNA prophylaxis ameliorates disease progression and provides treated mice the time to develop a SARS-CoV-2 specific neutralizing antibody response,

ultimately resulting in the effective clearance of viral infection. Moreover, the humoral response is reportedly dominant in mediating protection from SARS-CoV-2 re-infection upon vaccination or natural infection (Israelow et al., 2021).

The repetitive therapeutic treatment with 3pRNA on day one post infection also significantly reduced viral RNA levels in the lungs during the active course of infection (**Figure 15**), but with a survival rate of 20 % (**Figure 29**) this was less efficient in protecting SARS-CoV-2-infected mice against lethality than the single prophylactic treatment (25-50%, **Figure 18C**). This is in contrast to the single therapeutic treatment with SLR14 24 or 48 hrs after viral challenge that results in a survival rate of 40 % (Mao et al., 2022), albeit the 100-fold lower MOI as mentioned before. Besides, the i.n. infection of K18-hACE2 mice with $5x10^4$ PFU models a fatal course of COVID-19 disease with 100 % lethality, while the infection fatality rate in humans is estimated to be around 0.68-1.6 % (Ioannidis, 2021; Meyerowitz-Katz and Merone, 2020; Streeck et al., 2020). Furthermore, the high lethality in K18-hACE2 mouse model within 6 days after SARS-CoV-2 infection allows only a short therapeutic window for the treatment with RIG-I agonists, while in humans the time course of SARS-CoV-2 infection offers a longer window for therapeutic interventions. Hence, it is expected that the therapeutic effect provided by the RIG-I agonist treatment in the present study underestimates its potency against COVID-19 infections in humans.

Besides RNA-based RIG-I agonists, the cGAS-STING axis is crucially involved in the innate sensing of dsDNA in the cytosol that accumulates during viral infection or cellular stress and results in the induction of type I IFNs and ISGs as well (Decout et al., 2021). The prophylactic i.n. administration (6 hrs prior infection) or the therapeutic i.v. injection (4 hrs after infection) of the small molecule STING agonist diABZI potently has been shown to restrict lethal SARS-CoV-2 infections in K18-hACE2 mice with high survival rates of >80 % (Humphries et al., 2021; Li et al., 2021; Mao et al., 2022). In direct comparison, RIG-I and STING engagement leads to comparable high survival rates and are superior to the i.v. injection of universal IFNα (Mao et al., 2022). Noteworthy, local and systemic administration of different STING agonists are currently tested in several clinical studies for oncologic indications (Le Naour et al., 2020). Together with the preclinical data

obtained in the K18-hACE2 mice, the effectiveness of STING agonists could be readily tested in clinical studies for the treatment of COVID-19 patients.

Conclusively, it is likely that the activation of innate immune receptors resulting in IFN induction is superior to recombinant IFN itself in the context of viral infections. For instance, RIG-I stimulation leads to the activation of multiple downstream signaling pathways and offers the entire physiological spectrum of type I and III IFNs and even induces a broader anti-viral resistance than that induced upon type I IFN alone (Goulet et al., 2013; Linehan et al., 2018). While individuals with pre-existing neutralizing autoantibodies against selective (sub-) types of IFNα or IFNβ (Bastard et al., 2020; Zhang et al., 2020b) are considered unavailable for IFN therapy as stated before, the induction of multiple physiological subtypes of type I IFNs by RIG-I stimulation might offer a new treatment option and could provide a secondary layer of protection by the induction of type III IFNs and antiviral proteins. Additionally, PEGylation, differences in their amino acid sequence and glycosylation pattern may account for the high induction of anti-type I IFN autoantibodies upon recombinant IFN therapy compared to the production of physiological levels of endogenous IFNs upon innate immune sensor activation (Antonelli et al., 1991). Moreover, studies with immunocompromised *Rag*$^{-/-}$ mice have demonstrated that the single treatment with RIG-I agonists induces a potent innate anti-viral response against persistent SARS-CoV-2 infection in a type I IFN signaling dependent manner despite lacking adaptive immunity leading to the significant reduction of viral RNA in the lungs (Israelow et al., 2020; Mao et al., 2022). Accordingly, it can be speculated that RIG-I agonists may offer a promising new treatment option for patients with immune-compromised conditions to treat acute and persistent viral infections via a strong innate immune response regardless of the induction of adaptive immunity.

It has already been postulated that the B1.1.7 SARS-CoV-2 variant has increased resistance to type I IFN treatment *in vitro* (Thorne et al., 2021b). Despite showing varying efficacies, SLR14 has conferred broad protection against several SARS-CoV-2 variants of concern (B1.1.7, B.1.351, P.1, B.1.617.2, B.1.526) in the K18-hACE2 mouse model (Mao et al., 2022) indicating that RIG-I agonists represent a useful treatment option even against immune-evasive SARS-CoV-2 variants.

4.6. Considerations in the clinical administration of RIG-I agonists

Since RIG-I activation includes the induction of IFNs and pro-inflammatory cytokines, the administration of 3pRNA is likely accompanied with the development of adverse effects as seen upon IFN therapy. Typically, patients receiving IFNα treatment rapidly respond with flu-like symptoms such as fever, chills, myalgia and headache (Kirkwood et al., 2002; Sleijfer et al., 2005). Severity of symptoms is shown to be dose-dependent, albeit i.v. injections being less tolerable than local administrations (Sleijfer et al., 2005).

Mice presented neither weight loss nor other visible signs of unwanted side effects (e.g., ruffled fur, altered spontaneous behavior) upon the single systemic treatment with 20 µg 3pRNA (data not shown, **Figure 18B**). In previous work, repeated 3pRNA infections, even at higher doses (50 µg), are tolerable in mice as well, since no adverse effects nor desensitization have been observed (Coch et al., 2017; Poeck et al., 2008). While the side effects of systemic RIG-I agonist administration in humans are still largely unknown, the intratumoral application of 3pRNA results in mild (grade 1-2) fever and fatigue in patients (Middleton et al., 2018) (NCT03739138). However, it should be mentioned that the doses of local 3pRNA treatment used in this clinical study to induce cell-intrinsic cytotoxicity in the tumors are possibly unnecessarily high to induce anti-viral resistance. A single prophylactic treatment with 6.25 µg 3pRNA still completely protects mice from otherwise lethal IAV infections (Coch et al., 2017) enabling the speculation that lower doses of 3pRNA may also be sufficient to protect from lethal SARS-CoV-2 infections. Besides, 6.25 µg of 3pRNA induced only low levels of type I IFNs into sera of mice 6 hrs after application (**Figure 10A**) compared to 20 µg (**Figure 10D**), yet still resulted in the significant upregulation of anti-viral proteins in peripheral organs, including the lungs (**Figure 11**). This suggests that lower doses of 3pRNA might suffice for the establishment of anti-viral resistance against SARS-CoV-2 without the production of high levels of pro-inflammatory cytokines that might result in unwanted side effects.

It will be most important for further preclinical and clinical studies to find effective clinical doses of RIG-I agonists for anti-viral purposes while keeping undesirable adverse effects to a minimum. Exacerbated cytokine responses upon RIG-I stimulation may have detrimental effects on the host contributing to immune-mediated tissue damage and autoimmunity (Fajgenbaum and June, 2020; Tisoncik et al., 2012). As stated for the IFN therapy before, it can be assumed that early interventions with RIG-I agonists have

positive effects on the COVID-19 disease course by enhancing anti-viral activity, whereas late interventions in severely-infected hospitalized COVID-19 patients may lead to an even more pronounced inflammation substantially contributing to COVID-19 pathogenesis. Therefore, besides finding effective clinical doses of RIG-I agonist, the therapeutic treatment window needs to be carefully assessed in future clinical studies.

Additionally, higher risk for developing critical COVID-19 disease has been described for individuals with missense mutations in molecules involved in nucleic acid sensor signaling (*TLR3*, *UNC93B*, *IRF7*) or IFN signaling (*TYK2, OAS* and *IFNAR2*) (Pairo-Castineira et al., 2021; Zhang et al., 2020b) and for individuals with certain co-morbidities that are typically inflammatory in nature (Elezkurtaj et al., 2021; Wu and McGoogan, 2020). This indicates that pre-existing inflammation contributes to the severity of COVID-19 disease. Likewise, rarely abundant single-nucleotide polymorphisms in *DDX58* or *IFIH1*, the genes encoding for RIG-I and MDA5, are associated with an impaired or enhanced responsiveness to receptor activation and are linked to autoimmune and inflammatory diseases such as Systemic Lupus Erythematosus, Singleton-Merten Syndrome or Aicardi-Goutières Syndrome (Pothlichet et al., 2009; Yong and Luo, 2018b).

Nevertheless, at risk patients may also show an impaired or enhanced responsiveness to RIG-I administration which needs to be considered for finding effective doses of RIG-I agonists.

4.7. Outlook

This study provides new pre-clinical evidence for the potency and feasibility of RIG-I agonists as a new treatment option against SARS-CoV-2. Since RIG-I agonists have already been tested in phase I/II clinical studies for oncologic indications (NCT03739138, NCT0306502) (Middleton et al., 2018), clinical studies evaluating the prophylactic or therapeutic treatment efficacy of RIG-I agonists against COVID-19 may be rapidly initiated. Yet, careful clinical development is required to evaluate a suitable dose of RIG-I agonists for human patients that is effective against viral infection, but does not induce excessive systemic inflammation. Moreover, systemic application of RIG-I agonists limits its application so far to hospitalized patients. A possible way to reduce side effects and hence improve patient compliance could be the localized delivery, for example by the i.n. application of RIG-I agonists or by the inhalation of aerosolized RIG-I agonists. However,

local RNA delivery to the lungs still requires extensive optimizations in the formulation and dosing to enable efficient cellular uptake, bioavailability and pharmacokinetics, to stabilize the complexes against the natural barriers of the lungs (the presence of mucociliary clearance, alveolar fluids and nucleases) as well as to reduce considerable adverse effects while being protective (Anderson et al., 2020). Only recently, a new screening approach has been introduced that enables the optimization of lipid nanoparticles for the targeted mRNA delivery into the lungs via nebulized aerosols (Chang and Chan, 2021; Lokugamage et al., 2021). In a proof-of-principle experiment, the nebulized administration of a mRNA encoding for a broadly neutralizing antibody targeting IAV haemagglutinin by complexation with the optimized nanoparticles has shown to protect mice against otherwise lethal IAV infections (Lokugamage et al., 2021). While further research will be needed to evaluate if this approach can also be used for other RNA species and if it provides also effective delivery in the context of an ongoing viral infection, it may provide a very useful tool for efficient localized delivery of RIG-I agonists.

Additionally, the development of bifunctional dsRNA combining the RNA interference-mediated gene-silencing activity of siRNAs and the immunostimulatory activity of RIG-I could be used to further increase the anti-viral potency of immunostimulatory RNA. First proof-of-concept studies have demonstrated that siRNAs targeting HBV specific genes (Ebert et al., 2011) or the IAV nucleoprotein (Lin et al., 2012) combined with a 5’ triphosphate for agonistic RIG-I stimulation significantly inhibits viral replication *in vitro* and *in vivo* that have exceeded their single functions. It is plausible that the combination of the immunostimulatory capacity of RIG-I agonist as presented in this study, with a siRNA silencing an essential SARS-CoV-2 gene might further increase their therapeutic anti-viral potential against SARS-CoV-2. The highly conserved regions of ORF1 and 5’UTR, the RdRp and the viral helicase have already been identified as potential candidates for efficient siRNA silencing *in vitro* (Ambike et al., 2022; Idris et al., 2021; Tolksdorf et al., 2021).

While vaccines are the most powerful means of prophylaxis against SARS-CoV-2, RIG-I agonists may be of use for individuals for whom vaccinations are unavailable or ineffective due to a compromised adaptive immune system and could serve as a readily available treatment for novel viruses or strains that efficiently escape vaccine protection. So far, the *in vivo* evaluation of the protective function of RIG-I agonists has been mainly focused on

mouse models of IAV (Chiang et al., 2015; Coch et al., 2017; Goulet et al., 2013) and recently SARS-CoV-2 infections (present study) (Mao et al., 2022). In *in vitro* studies, the anti-viral activity of RIG-I agonists against a variety of viruses has been evaluated as well, including *filoviridae* (e.g. Ebola Virus), *poxviridae* (e.g. Vaccinia Virus), *rhabdoviridae* (e.g. Vesicular Stomatitis Virus), *Flaviviridae* (e.g. Dengue Virus) and *togaviridae* (Chikungunya Virus) (Chiang et al., 2015; Goulet et al., 2013; Olagnier et al., 2014; Spiropoulou et al., 2009). Further studies are required to explore the potency of RIG-I against to confer protection against these viruses *in vivo*. Altogether, the broad anti-viral protection provided by RIG-I may offer a suitable option to reduce the need for virus-specific treatments and inhibit the spread of newly emerging or re-emerging viruses in the future.

5. Summary

The recent outbreak of the COVID-19 pandemic highlights the need for novel prophylactic and therapeutic countermeasures against newly emerging viruses. Innate immune receptor agonists are considered to be a promising new approach to provide potent anti-viral protection. Activation of the cytosolic nucleic acid sensor RIG-I by selective short 5' triphosphate dsRNA resulted in the induction of pro-inflammatory cytokines and type I interferons, in the establishment of immediate antiviral resistance on a single-cell level in the lungs, and shaped both innate and adaptive immunity through the recruitment and activation of immune cells. While RIG-I agonists mediate strong anti-viral protection against Influenza A infections in mouse models, their potency has not been yet investigated in conferring protection against SARS-CoV-2. *In vitro*, the prophylactic treatment with RIG-I agonists inhibited SARS-CoV-2 viral replication and induced sustained expression of interferons and proinflammatory cytokines more potently than treatment with recombinant IFNα. Moreover, the effectiveness of RIG-I agonists against SARS-CoV-2 was tested *in vivo* in a mouse model of severe SARS-CoV-2 infection. A single prophylactic systemic administration of RIG-I agonist, but not recombinant IFNα, potently inhibited viral replication in the upper respiratory tract, lungs and brain and reduced local inflammation in the lungs. Furthermore, the single prophylactic treatment up to seven days prior to the infection conferred intermediate levels of protection from lethality, with the best protection being achieved when given one day prior to infection. Survival was associated with cleared viral infection in the lungs and brain and the generation of high titers of neutralizing IgG antibodies against SARS-CoV-2. In addition, repeated systemic therapeutic RIG-I agonist treatment also led to the partial protection against COVID-19 associated mortality and significantly suppressed viral replication in the lungs during the active course of infection. Collectively, this study provides new preclinical evidence that RIG-I agonists may serve as a new broadly-active and effective anti-viral treatment option against emerging and re-emerging viral infections in the future by the potent induction of innate immunity.

6. List of tables

7. List of figures

8. Appendix

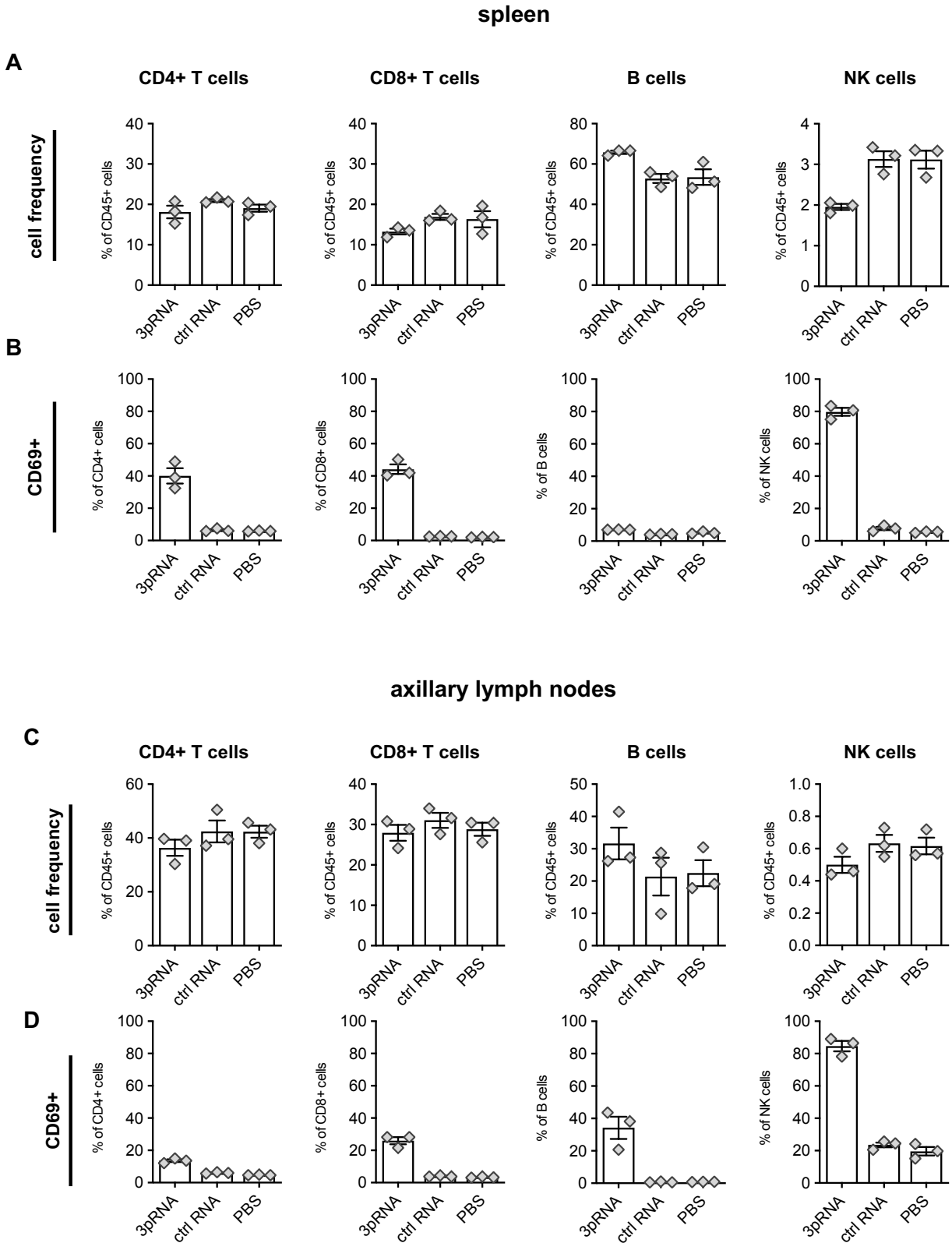
spleen
A
CD4+ T cells
CD8+ T cells
B cells
NK cells
cell frequency
% of CD45+ cells
B
CD69+
% of CD4+ cells
% of CD8+ cells
% of B cells
% of NK cells
3pRNA
ctrl RNA
PBS
axillary lymph nodes
C
D

Appendix Figure 1: Cell frequencies and activation of effector immune cells in the spleen and axillary lymph nodes upon 3pRNA stimulation. Spleen and axillary lymph nodes were collected for flow cytometry from mice 6 hrs upon 6.25 µg 3pRNA or ctrl RNA i.v. injection. (A+C) Frequencies of immune effector cell populations (CD4+ and CD8+ T cells, B cells, NK cells) in the spleen (A) and axillary lymph node (C) relative to all CD45+ cells. (B+D) Frequencies of CD69+ activated immune cells in the spleen (B) and axillary lymph node (D) relative to the parental cell population. Data are shown as mean ± SEM (n=3) and are representative of two independent experiments.

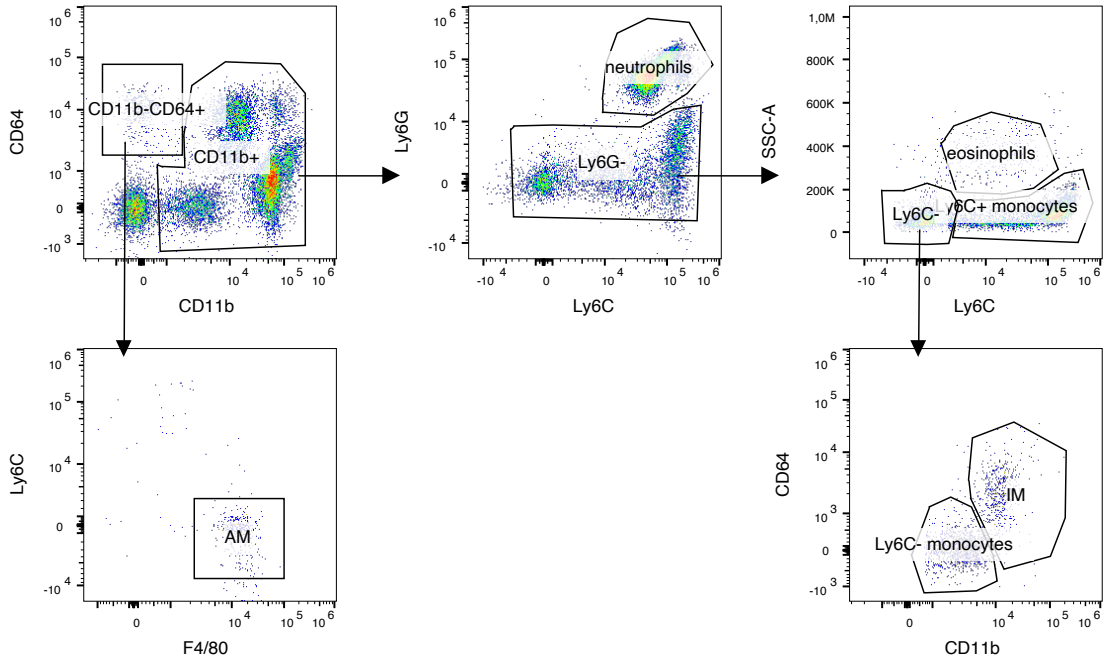

Appendix Figure 2: Gating strategy for myeloid cells of the lungs. Cells were first gated on live CD45+ single cells. Alveolar macrophages (AMs) were gated as CD11b-CD64+F4/80+Ly6C- cells, neutrophils as CD11b+Ly6C+Ly6G+ cells, eosinophils as CD11b+Ly6C+Ly6G-SSC^{hi} cells, Ly6C^{+} monocytes as CD11b+Ly6G-Ly6C+ cells, Ly6C^{-} monocytes as CD11b^{int}Ly6G-CD64-Ly6C- cells and interstitial macrophages (IMs) as CD11b^{hi}Ly6G-Ly6C-CD64+ cells. Shown is the gating strategy for one representative mouse.

9. References

Ablasser, A., Bauernfeind, F., Hartmann, G., Latz, E., Fitzgerald, K.A., and Hornung, V. (2009). RIG-I-dependent sensing of poly(dA:dT) through the induction of an RNA polymerase III–transcribed RNA intermediate. Nat. Immunol. *10*, 1065–1072.

Alavi Darazam, I., Shokouhi, S., Pourhoseingholi, M.A., Naghibi Irvani, S.S., Mokhtari, M., Shabani, M., Amirdosara, M., Torabinavid, P., Golmohammadi, M., Hashemi, S., et al. (2021). Role of interferon therapy in severe COVID-19: the COVIFERON randomized controlled trial. Sci. Rep. *11*, 8059.

Ambike, S., Cheng, C.-C., Feuerherd, M., Velkov, S., Baldassi, D., Afridi, S.Q., Porras-Gonzalez, D., Wei, X., Hagen, P., Kneidinger, N., et al. (2022). Targeting genomic SARS-CoV-2 RNA with siRNAs allows efficient inhibition of viral replication and spread. Nucleic Acids Res. *50*, 333–349.

Anderson, C.F., Grimmett, M.E., Domalewski, C.J., and Cui, H. (2020). Inhalable nanotherapeutics to improve treatment efficacy for common lung diseases. WIREs Nanomedicine and Nanobiotechnology *12*.

Angus, D.C., Derde, L., Al-Beidh, F., Annane, D., Arabi, Y., Beane, A., van Bentum-Puijk, W., Berry, L., Bhimani, Z., Bonten, M., et al. (2020). Effect of Hydrocortisone on Mortality and Organ Support in Patients With Severe COVID-19. JAMA *324*, 1317.

Antonelli, G., Currenti, M., Turriziani, O., and Dianzani, F. (1991). Neutralizing Antibodies to Interferon- : Relative Frequency in Patients Treated with Different Interferon Preparations. J. Infect. Dis. *163*, 882–885.

Bao, L., Deng, W., Huang, B., Gao, H., Liu, J., Ren, L., Wei, Q., Yu, P., Xu, Y., Qi, F., et al. (2020). The pathogenicity of SARS-CoV-2 in hACE2 transgenic mice. Nature *583*, 830–833.

Bartok, E., and Hartmann, G. (2020). Immune Sensing Mechanisms that Discriminate Self from Altered Self and Foreign Nucleic Acids. Immunity *53*, 54–77.

Bastard, P., Rosen, L.B., Zhang, Q., Michailidis, E., Hoffmann, H.-H., Zhang, Y., Dorgham, K., Philippot, Q., Rosain, J., Béziat, V., et al. (2020). Autoantibodies against type I IFNs in patients with life-threatening COVID-19. Science (80-.). *370*, eabd4585.

Bauer, S., Kirschning, C.J., Häcker, H., Redecke, V., Hausmann, S., Akira, S., Wagner, H., and Lipford, G.B. (2001). Human TLR9 confers responsiveness to bacterial DNA via species-specific CpG motif recognition. Proc. Natl. Acad. Sci. U. S. A. *98*, 9237–9242.

Beigel, J.H., Tomashek, K.M., Dodd, L.E., Mehta, A.K., Zingman, B.S., Kalil, A.C., Hohmann, E., Chu, H.Y., Luetkemeyer, A., Kline, S., et al. (2020). Remdesivir for the Treatment of Covid-19 — Final Report. N. Engl. J. Med. *383*, 1813–1826.

Berke, I.C., and Modis, Y. (2012). MDA5 cooperatively forms dimers and ATP-sensitive filaments upon binding double-stranded RNA. EMBO J. *31*, 1714–1726.

Le Bert, N., Clapham, H.E., Tan, A.T., Chia, W.N., Tham, C.Y.L., Lim, J.M., Kunasegaran, K., Tan, L.W.L., Dutertre, C.-A., Shankar, N., et al. (2021). Highly functional virus-specific cellular immune response in asymptomatic SARS-CoV-2 infection. J. Exp. Med. *218*.

Besch, R., Poeck, H., Hohenauer, T., Senft, D., Häcker, G., Berking, C., Hornung, V., Endres, S., Ruzicka, T., Rothenfusser, S., et al. (2009). Proapoptotic signaling induced by RIG-I and MDA-5 results in type I interferon-independent apoptosis in human melanoma cells. J. Clin. Invest. *119*, 2399–2411.

Beyer, D.K., and Forero, A. (2021). Mechanisms of Antiviral Immune Evasion of SARS-CoV-2. J. Mol. Biol. 167265.

Bikdeli, B., Madhavan, M. V., Jimenez, D., Chuich, T., Dreyfus, I., Driggin, E., Nigoghossian, C. Der, Ageno, W., Madjid, M., Guo, Y., et al. (2020). COVID-19 and Thrombotic or Thromboembolic Disease: Implications for Prevention, Antithrombotic Therapy, and Follow-Up. J. Am. Coll. Cardiol. *75*, 2950–2973.

Blanco-Melo, D., Nilsson-Payant, B.E., Liu, W.-C., Uhl, S., Hoagland, D., Møller, R., Jordan, T.X., Oishi, K., Panis, M., Sachs, D., et al. (2020). Imbalanced Host Response to SARS-CoV-2 Drives Development of COVID-19. Cell *181*, 1036-1045.e9.

Bolen, C.R., Ding, S., Robek, M.D., and Kleinstein, S.H. (2014). Dynamic expression profiling of type I and type III interferon-stimulated hepatocytes reveals a stable hierarchy of gene expression. Hepatology *59*, 1262–1272.

Bonilla, F.A., and Oettgen, H.C. (2010). Adaptive immunity. J. Allergy Clin. Immunol. *125*, S33–S40.

Bonville, C.A., Rosenberg, H.F., and Domachowske, J.B. (1999). Macrophage inflammatory protein-1α and RANTES are present in nasal secretions during ongoing upper respiratory tract infection. Pediatr. Allergy Immunol. *10*, 39–44.

Bradbury, C.A., and McQuilten, Z. (2022). Anticoagulation in COVID-19. Lancet *399*, 5–7.

Bruns, A.M., Leser, G.P., Lamb, R.A., and Horvath, C.M. (2014). The Innate Immune Sensor LGP2 Activates Antiviral Signaling by Regulating MDA5-RNA Interaction and Filament Assembly. Mol. Cell *55*, 771–781.

Cameron, M.J., Ran, L., Xu, L., Danesh, A., Bermejo-Martin, J.F., Cameron, C.M., Muller, M.P., Gold, W.L., Richardson, S.E., Poutanen, S.M., et al. (2007). Interferon-Mediated Immunopathological Events Are Associated with Atypical Innate and Adaptive Immune Responses in Patients with Severe Acute Respiratory Syndrome. J. Virol. *81*, 8692–8706.

Chang, R.Y.K., and Chan, H.-K. (2021). Lipid nanoparticles for the inhalation of mRNA. Nat. Biomed. Eng. *5*, 949–950.

Channappanavar, R., Fehr, A.R., Vijay, R., Mack, M., Zhao, J., Meyerholz, D.K., and Perlman, S. (2016). Dysregulated Type I Interferon and Inflammatory Monocyte-Macrophage Responses Cause Lethal Pneumonia in SARS-CoV-Infected Mice. Cell Host Microbe *19*, 181–193.

Channappanavar, R., Fehr, A.R., Zheng, J., Wohlford-Lenane, C., Abrahante, J.E., Mack, M., Sompallae, R., McCray, P.B., Meyerholz, D.K., and Perlman, S. (2019). IFN-I response timing relative to virus replication determines MERS coronavirus infection outcomes. J. Clin. Invest. *129*, 3625–3639.

Chaplin, D.D. (2010). Overview of the immune response. J. Allergy Clin. Immunol. *125*, S3–S23.

Chen, L., and Flies, D.B. (2013). Molecular mechanisms of T cell co-stimulation and co-inhibition. Nat. Rev. Immunol. *13*, 227–242.

Chen, J.S., Alfajaro, M.M., Chow, R.D., Wei, J., Filler, R.B., Eisenbarth, S.C., and Wilen, C.B. (2021). Nonsteroidal Anti-inflammatory Drugs Dampen the Cytokine and Antibody Response to SARS-CoV-2 Infection. J. Virol. *95*.

Chen, K., Xiao, F., Hu, D., Ge, W., Tian, M., Wang, W., Pan, P., Wu, K., and Wu, J. (2020). SARS-CoV-2 Nucleocapsid Protein Interacts with RIG-I and Represses RIG-Mediated IFN-β Production. Viruses *13*, 1–15.

Chen, Y., Cai, H., Pan, J., Xiang, N., Tien, P., Ahola, T., and Guo, D. (2009). Functional screen reveals SARS coronavirus nonstructural protein nsp14 as a novel cap N7 methyltransferase. Proc. Natl. Acad. Sci. *106*, 3484–3489.

Chiang, C., Beljanski, V., Yin, K., Olagnier, D., Ben Yebdri, F., Steel, C., Goulet, M.-L., DeFilippis, V.R., Streblow, D.N., Haddad, E.K., et al. (2015). Sequence-Specific Modifications Enhance the Broad-Spectrum Antiviral Response Activated by RIG-I Agonists. J. Virol. *89*, 8011–8025.

Chiu, Y.-H., MacMillan, J.B., and Chen, Z.J. (2009). RNA Polymerase III Detects Cytosolic DNA and Induces Type I Interferons through the RIG-I Pathway. Cell *138*, 576–591.

Coch, C., Stümpel, J.P., Lilien-Waldau, V., Wohlleber, D., Kümmerer, B.M., Bekeredjian-Ding, I., Kochs, G., Garbi, N., Herberhold, S., Schuberth-Wagner, C., et al. (2017). RIG-I Activation Protects and Rescues from Lethal Influenza Virus Infection and Bacterial Superinfection. Mol. Ther. *25*, 2093–2103.

Collie, S., Champion, J., Moultrie, H., Bekker, L.-G., and Gray, G. (2021). Effectiveness of BNT162b2 Vaccine against Omicron Variant in South Africa. N. Engl. J. Med.

Crotta, S., Davidson, S., Mahlakoiv, T., Desmet, C.J., Buckwalter, M.R., Albert, M.L., Staeheli, P., and Wack, A. (2013). Type I and Type III Interferons Drive Redundant Amplification Loops to Induce a Transcriptional Signature in Influenza-Infected Airway Epithelia. PLoS Pathog. *9*, e1003773.

Cui, J., Li, F., and Shi, Z.-L. (2019). Origin and evolution of pathogenic coronaviruses. Nat. Rev. Microbiol. *17*, 181–192.

Dagan, N., Barda, N., Kepten, E., Miron, O., Perchik, S., Katz, M.A., Hernán, M.A., Lipsitch, M., Reis, B., and Balicer, R.D. (2021). BNT162b2 mRNA Covid-19 Vaccine in a Nationwide Mass Vaccination Setting. N. Engl. J. Med. *384*, 1412–1423.

Dangl, J.L., and Jones, J.D.G. (2001). Plant pathogens and integrated defence responses to infection. Nature *411*, 826–833.

Das, M., Shen, L., Liu, Q., Goodwin, T.J., and Huang, L. (2019). Nanoparticle Delivery of RIG-I Agonist Enables Effective and Safe Adjuvant Therapy in Pancreatic Cancer. Mol. Ther. *27*, 507–517.

Daßler-Plenker, J., Paschen, A., Putschli, B., Rattay, S., Schmitz, S., Goldeck, M., Bartok, E., Hartmann, G., and Coch, C. (2019). Direct RIG-I activation in human NK cells induces TRAIL-dependent cytotoxicity toward autologous melanoma cells. Int. J. Cancer *144*, 1645–1656.

Davidson, S., McCabe, T.M., Crotta, S., Gad, H.H., Hessel, E.M., Beinke, S., Hartmann, R., and Wack, A. (2016). <scp>IFN</scp> λ is a potent anti-influenza therapeutic without the inflammatory side effects of <scp>IFN</scp> α treatment. EMBO Mol. Med. *8*, 1099–1112.

Dawson, T.C., Beck, M.A., Kuziel, W.A., Henderson, F., and Maeda, N. (2000). Contrasting Effects of CCR5 and CCR2 Deficiency in the Pulmonary Inflammatory Response to Influenza A Virus. Am. J. Pathol. *156*, 1951–1959.

Decout, A., Katz, J.D., Venkatraman, S., and Ablasser, A. (2021). The cGAS–STING pathway as a therapeutic target in inflammatory diseases. Nat. Rev. Immunol. *21*, 548–569.

Devarkar, S.C., Wang, C., Miller, M.T., Ramanathan, A., Jiang, F., Khan, A.G., Patel, S.S., and Marcotrigiano, J. (2016). Structural basis for m7G recognition and 2′-O-methyl discrimination in capped RNAs by the innate immune receptor RIG-I. Proc. Natl. Acad. Sci. *113*, 596–601.

Dixit, E., Boulant, S., Zhang, Y., Lee, A.S.Y., Odendall, C., Shum, B., Hacohen, N., Chen, Z.J., Whelan, S.P., Fransen, M., et al. (2010). Peroxisomes Are Signaling Platforms for Antiviral Innate Immunity. Cell *141*, 668–681.

Drosten, C., Günther, S., Preiser, W., van der Werf, S., Brodt, H.-R., Becker, S., Rabenau, H., Panning, M., Kolesnikova, L., Fouchier, R.A.M., et al. (2003). Identification of a Novel Coronavirus in Patients with Severe Acute Respiratory Syndrome. N. Engl. J. Med. *348*, 1967–1976.

Dunkelberger, J.R., and Song, W.-C. (2010). Complement and its role in innate and adaptive immune responses. Cell Res. *20*, 34–50.

Ebert, G., Poeck, H., Lucifora, J., Baschuk, N., Esser, K., Esposito, I., Hartmann, G., and Protzer, U. (2011). 5′ Triphosphorylated Small Interfering RNAs Control Replication of Hepatitis B Virus and Induce an Interferon Response in Human Liver Cells and Mice. Gastroenterology *141*, 696-706.e3.

Elezkurtaj, S., Greuel, S., Ihlow, J., Michaelis, E.G., Bischoff, P., Kunze, C.A., Sinn, B.V., Gerhold, M., Hauptmann, K., Ingold-Heppner, B., et al. (2021). Causes of death and comorbidities in hospitalized patients with COVID-19. Sci. Rep. *11*, 4263.

Elion, D.L., and Cook, R.S. (2018). Harnessing RIG-I and intrinsic immunity in the tumor microenvironment for therapeutic cancer treatment. Oncotarget *9*, 29007–29017.

Engel, C., Brügmann, G., Lambing, S., Mühlenbeck, L.H., Marx, S., Hagen, C., Horváth, D., Goldeck, M., Ludwig, J., Herzner, A.-M., et al. (2017). RIG-I Resists Hypoxia-Induced Immunosuppression and Dedifferentiation. Cancer Immunol. Res. *5*, 455–467.

Fajgenbaum, D.C., and June, C.H. (2020). Cytokine Storm. N. Engl. J. Med. *383*, 2255–2273.

Feld, J.J., Kandel, C., Biondi, M.J., Kozak, R.A., Zahoor, M.A., Lemieux, C., Borgia, S.M., Boggild, A.K., Powis, J., McCready, J., et al. (2021). Peginterferon lambda for the treatment of outpatients with COVID-19: a phase 2, placebo-controlled randomised trial. Lancet Respir. Med. *9*, 498–510.

Foster, G.R. (2004). Pegylated interferons: chemical and clinical differences. Aliment. Pharmacol. Ther. *20*, 825–830.

Galani, I.E., Triantafyllia, V., Eleminiadou, E.-E., Koltsida, O., Stavropoulos, A., Manioudaki, M., Thanos, D., Doyle, S.E., Kotenko, S. V., Thanopoulou, K., et al. (2017). Interferon-λ Mediates Non-redundant Front-Line Antiviral Protection against Influenza Virus Infection without Compromising Host Fitness. Immunity *46*, 875-890.e6.

Gheblawi, M., Wang, K., Viveiros, A., Nguyen, Q., Zhong, J.-C., Turner, A.J., Raizada, M.K., Grant, M.B., and Oudit, G.Y. (2020). Angiotensin-Converting Enzyme 2: SARS-CoV-2 Receptor and Regulator of the Renin-Angiotensin System. Circ. Res. *126*, 1456–1474.

Giovannoni, G. (2002). Neutralising antibodies to interferon beta during the treatment of multiple sclerosis. J. Neurol. Neurosurg. Psychiatry *73*, 465–469.

Goldeck, M., Tuschl, T., Hartmann, G., and Ludwig, J. (2014). Efficient Solid-Phase Synthesis of pppRNA by Using Product-Specific Labeling. Angew. Chemie Int. Ed. *53*, 4694–4698.

González-Navajas, J.M., Lee, J., David, M., and Raz, E. (2012). Immunomodulatory functions of type I interferons. Nat. Rev. Immunol. *12*, 125–135.

Goral, S. (2011). The three-signal hypothesis of lymphocyte activation/targets for immunosuppression. Dial. Transplant. *40*, 14–16.

Goubau, D., Schlee, M., Deddouche, S., Pruijssers, A.J., Goldeck, M., Schuberth, C., Veen, A.G. Van Der, Rehwinkel, J., Iskarpatyoti, J.A., Barchet, W., et al. (2015). Europe PMC Funders Group Antiviral immunity via RIG-I-mediated recognition of RNA bearing 5 ′ -diphosphates. *514*, 372–375.

Goulet, M.-L.L., Olagnier, D., Xu, Z., Paz, S., Belgnaoui, S.M., Lafferty, E.I., Janelle, V., Arguello, M., Paquet, M., Ghneim, K., et al. (2013). Systems Analysis of a RIG-I Agonist Inducing Broad Spectrum Inhibition of Virus Infectivity. PLoS Pathog. *9*, e1003298.

Grasselli, G., Tonetti, T., Protti, A., Langer, T., Girardis, M., Bellani, G., Laffey, J., Carrafiello, G., Carsana, L., Rizzuto, C., et al. (2020). Pathophysiology of COVID-19-associated acute respiratory distress syndrome: a multicentre prospective observational study. Lancet Respir. Med. *8*, 1201–1208.

Gupta, A., Madhavan, M. V., Sehgal, K., Nair, N., Mahajan, S., Sehrawat, T.S., Bikdeli, B., Ahluwalia, N., Ausiello, J.C., Wan, E.Y., et al. (2020). Extrapulmonary manifestations of COVID-19. Nat. Med. *26*, 1017–1032.

Haas, E.J., Angulo, F.J., McLaughlin, J.M., Anis, E., Singer, S.R., Khan, F., Brooks, N., Smaja, M., Mircus, G., Pan, K., et al. (2021). Impact and effectiveness of mRNA BNT162b2 vaccine against SARS-CoV-2 infections and COVID-19 cases, hospitalisations, and deaths following a nationwide vaccination campaign in Israel: an observational study using national surveillance data. Lancet *397*, 1819–1829.

Hadjadj, J., Yatim, N., Barnabei, L., Corneau, A., Boussier, J., Smith, N., Péré, H., Charbit, B., Bondet, V., Chenevier-Gobeaux, C., et al. (2020). Impaired type I interferon activity and inflammatory responses in severe COVID-19 patients. Science (80-.). *369*, 718–724.

Haeberle, H.A., Kuziel, W.A., Dieterich, H.-J., Casola, A., Gatalica, Z., and Garofalo, R.P. (2001). Inducible Expression of Inflammatory Chemokines in Respiratory Syncytial Virus-Infected Mice: Role of MIP-1α in Lung Pathology. J. Virol. *75*, 878–890.

Hartenian, E., Nandakumar, D., Lari, A., Ly, M., Tucker, J.M., and Glaunsinger, B.A. (2020). The molecular virology of coronaviruses. J. Biol. Chem. *295*, 12910–12934.

Helms, J., Kremer, S., Merdji, H., Clere-Jehl, R., Schenck, M., Kummerlen, C., Collange, O., Boulay, C., Fafi-Kremer, S., Ohana, M., et al. (2020). Neurologic Features in Severe SARS-CoV-2 Infection. N. Engl. J. Med. *382*, 2268–2270.

Hemmi, H., Takeuchi, O., Kawai, T., Kaisho, T., Sato, S., Sanjo, H., Matsumoto, M., Hoshino, K., Wagner, H., Takeda, K., et al. (2000). A Toll-like receptor recognizes bacterial DNA. Nature *408*, 740–745.

Henriquez, K.M., Hayney, M.S., Xie, Y., Zhang, Z., and Barrett, B. (2015). Association of interleukin-8 and neutrophils with nasal symptom severity during acute respiratory infection. J. Med. Virol. *87*, 330–337.

Hikmet, F., Méar, L., Edvinsson, Å., Micke, P., Uhlén, M., and Lindskog, C. (2020). The protein expression profile of ACE2 in human tissues. Mol. Syst. Biol. *16*.

Hoffmann, M., Kleine-Weber, H., Schroeder, S., Krüger, N., Herrler, T., Erichsen, S., Schiergens, T.S., Herrler, G., Wu, N.-H., Nitsche, A., et al. (2020). SARS-CoV-2 Cell Entry Depends on ACE2 and TMPRSS2 and Is Blocked by a Clinically Proven Protease Inhibitor. Cell *181*, 271-280.e8.

Hornung, V., Ellegast, J., Kim, S., Brzózka, K., Jung, A., Kato, H., Poeck, H., Akira, S., Conzelmann, K.-K., Schlee, M., et al. (2006). 5'-Triphosphate RNA is the ligand for RIG-I. Science *314*, 994–997.

Hou, F., Sun, L., Zheng, H., Skaug, B., Jiang, Q.-X., and Chen, Z.J. (2011). MAVS forms functional prion-like aggregates to activate and propagate antiviral innate immune response. Cell *146*, 448–461.

Huang, C., Wang, Y., Li, X., Ren, L., Zhao, J., Hu, Y., Zhang, L., Fan, G., Xu, J., Gu, X., et al. (2020). Clinical features of patients infected with 2019 novel coronavirus in Wuhan, China. Lancet *395*, 497–506.

Humphries, F., Shmuel-Galia, L., Jiang, Z., Wilson, R., Landis, P., Ng, S.-L., Parsi, K.M., Maehr, R., Cruz, J., Morales, A., et al. (2021). A diamidobenzimidazole STING agonist protects against SARS-CoV-2 infection. Sci. Immunol. *6*.

Hunter, C.A., and Jones, S.A. (2015). IL-6 as a keystone cytokine in health and disease. Nat. Immunol. *16*, 448–457.

Idris, A., Davis, A., Supramaniam, A., Acharya, D., Kelly, G., Tayyar, Y., West, N., Zhang, P., McMillan, C.L.D., Soemardy, C., et al. (2021). A SARS-CoV-2 targeted siRNA-nanoparticle therapy for COVID-19. Mol. Ther. *29*, 2219–2226.

Ioannidis, J.P.A. (2021). Infection fatality rate of COVID-19 inferred from seroprevalence data. Bull. World Health Organ. *99*, 19-33F.

Israelow, B., Song, E., Mao, T., Lu, P., Meir, A., Liu, F., Alfajaro, M.M., Wei, J., Dong, H., Homer, R.J., et al. (2020). Mouse model of SARS-CoV-2 reveals inflammatory role of type I interferon signaling. J. Exp. Med. *217*.

Israelow, B., Mao, T., Klein, J., Song, E., Menasche, B., Omer, S.B., and Iwasaki, A. (2021). Adaptive immune determinants of viral clearance and protection in mouse models of SARS-CoV-2. Sci. Immunol. *6*.

Janeway, C.A., and Medzhitov, R. (2002). Innate Immune Recognition. Annu. Rev. Immunol. *20*, 197–216.

Jayk Bernal, A., Gomes da Silva, M.M., Musungaie, D.B., Kovalchuk, E., Gonzalez, A., Delos Reyes, V., Martín-Quirós, A., Caraco, Y., Williams-Diaz, A., Brown, M.L., et al. (2021). Molnupiravir for Oral Treatment of Covid-19 in Nonhospitalized Patients. N. Engl. J. Med.

Jiang, F., Ramanathan, A., Miller, M.T., Tang, G.-Q., Gale, M., Patel, S.S., and Marcotrigiano, J. (2011). Structural basis of RNA recognition and activation by innate immune receptor RIG-I. Nature *479*, 423–427.

Jiang, X., Muthusamy, V., Fedorova, O., Kong, Y., Kim, D.J., Bosenberg, M., Pyle, A.M., and Iwasaki, A. (2019). Intratumoral delivery of RIG-I agonist SLR14 induces robust antitumor responses. J. Exp. Med. *216*, 2854–2868.

Jones, J.D.G., and Dangl, J.L. (2006). The plant immune system. Nature *444*, 323–329.

Junt, T., and Barchet, W. (2015). Translating nucleic acid-sensing pathways into therapies. Nat. Rev. Immunol. *15*, 529–544.

Kang, D., Gopalkrishnan, R. V, Lin, L., Randolph, A., Valerie, K., Pestka, S., and Fisher, P.B. (2004). Expression analysis and genomic characterization of human melanoma differentiation associated gene-5, mda-5: a novel type I interferon-responsive apoptosis-inducing gene. Oncogene *23*, 1789–1800.

Kato, H., Sato, S., Yoneyama, M., Yamamoto, M., Uematsu, S., Matsui, K., Tsujimura, T., Takeda, K., Fujita, T., Takeuchi, O., et al. (2005). Cell Type-Specific Involvement of RIG-I in Antiviral Response. Immunity *23*, 19–28.

Kato, H., Takeuchi, O., Sato, S., Yoneyama, M., Yamamoto, M., Matsui, K., Uematsu, S., Jung, A., Kawai, T., Ishii, K.J., et al. (2006). Differential roles of MDA5 and RIG-I helicases in the recognition of RNA viruses. Nature *441*, 101–105.

Kato, H., Takeuchi, O., Mikamo-Satoh, E., Hirai, R., Kawai, T., Matsushita, K., Hiiragi, A., Dermody, T.S., Fujita, T., and Akira, S. (2008). Length-dependent recognition of double-stranded ribonucleic acids by retinoic acid–inducible gene-I and melanoma differentiation–associated gene 5. J. Exp. Med. *205*, 1601–1610.

Kesheh, M.M., Hosseini, P., Soltani, S., and Zandi, M. (2021). An overview on the seven pathogenic human coronaviruses. Rev. Med. Virol.

Kirkwood, J.M., Bender, C., Agarwala, S., Tarhini, A., Shipe-Spotloe, J., Smelko, B., Donnelly, S., and Stover, L. (2002). Mechanisms and Management of Toxicities Associated With High-Dose Interferon Alfa-2b Therapy. J. Clin. Oncol. *20*, 3703–3718.

Klinkhammer, J., Schnepf, D., Ye, L., Schwaderlapp, M., Gad, H.H., Hartmann, R., Garcin, D., Mahlakõiv, T., and Staeheli, P. (2018). IFN-λ prevents influenza virus spread from the upper airways to the lungs and limits virus transmission. Elife *7*.

Koenig, P.-A., Das, H., Liu, H., Kümmerer, B.M., Gohr, F.N., Jenster, L.-M., Schiffelers, L.D.J., Tesfamariam, Y.M., Uchima, M., Wuerth, J.D., et al. (2021). Structure-guided

multivalent nanobodies block SARS-CoV-2 infection and suppress mutational escape. Science (80-.). *371*.

Kohli, A., Zhang, X., Yang, J., Russell, R.S., Donnelly, R.P., Sheikh, F., Sherman, A., Young, H., Imamichi, T., Lempicki, R.A., et al. (2012). Distinct and overlapping genomic profiles and antiviral effects of Interferon-λ and -α on HCV-infected and noninfected hepatoma cells. J. Viral Hepat. *19*, 843–853.

Kotenko, S. V., Gallagher, G., Baurin, V. V., Lewis-Antes, A., Shen, M., Shah, N.K., Langer, J.A., Sheikh, F., Dickensheets, H., and Donnelly, R.P. (2003). IFN-λs mediate antiviral protection through a distinct class II cytokine receptor complex. Nat. Immunol. *4*, 69–77.

Kouwaki, T., Nishimura, T., Wang, G., and Oshiumi, H. (2021). RIG-I-Like Receptor-Mediated Recognition of Viral Genomic RNA of Severe Acute Respiratory Syndrome Coronavirus-2 and Viral Escape From the Host Innate Immune Responses. Front. Immunol. *12*.

Kowalinski, E., Lunardi, T., McCarthy, A.A., Louber, J., Brunel, J., Grigorov, B., Gerlier, D., and Cusack, S. (2011). Structural Basis for the Activation of Innate Immune Pattern-Recognition Receptor RIG-I by Viral RNA. Cell *147*, 423–435.

Kowalski, P.S., Rudra, A., Miao, L., and Anderson, D.G. (2019). Delivering the Messenger: Advances in Technologies for Therapeutic mRNA Delivery. Mol. Ther. *27*, 710–728.

Kumar, S., Thambiraja, T.S., Karuppanan, K., and Subramaniam, G. (2021). Omicron and Delta variant of SARS-CoV-2: A comparative computational study of spike protein. J. Med. Virol.

Kumari, P., Rothan, H.A., Natekar, J.P., Stone, S., Pathak, H., Strate, P.G., Arora, K., Brinton, M.A., and Kumar, M. (2021). Neuroinvasion and Encephalitis Following Intranasal Inoculation of SARS-CoV-2 in K18-hACE2 Mice. Viruses *13*.

Laing, A.G., Lorenc, A., del Molino del Barrio, I., Das, A., Fish, M., Monin, L., Muñoz-Ruiz, M., McKenzie, D.R., Hayday, T.S., Francos-Quijorna, I., et al. (2020). A dynamic COVID-19 immune signature includes associations with poor prognosis. Nat. Med. *26*, 1623–1635.

Lazear, H.M., Nice, T.J., and Diamond, M.S. (2015). Interferon-λ: Immune Functions at Barrier Surfaces and Beyond. Immunity *43*, 15–28.

Lei, X., Dong, X., Ma, R., Wang, W., Xiao, X., Tian, Z., Wang, C., Wang, Y., Li, L., Ren, L., et al. (2020). Activation and evasion of type I interferon responses by SARS-CoV-2. Nat. Commun. *11*, 3810.

Li, M., Ferretti, M., Ying, B., Descamps, H., Lee, E., Dittmar, M., Lee, J.S., Whig, K., Kamalia, B., Dohnalová, L., et al. (2021). Pharmacological activation of STING blocks SARS-CoV-2 infection. Sci. Immunol. *6*.

Lin, L., Liu, Q., Berube, N., Detmer, S., and Zhou, Y. (2012). 5'-Triphosphate-Short Interfering RNA: Potent Inhibition of Influenza A Virus Infection by Gene Silencing and RIG-I Activation. J. Virol. *86*, 10359–10369.

Lindell, D.M., Lane, T.E., and Lukacs, N.W. (2008). CXCL10/CXCR3-mediated responses promote immunity to respiratory syncytial virus infection by augmenting dendritic cell and CD8 + T cell efficacy. Eur. J. Immunol. *38*, 2168–2179.

Linehan, M.M., Dickey, T.H., Molinari, E.S., Fitzgerald, M.E., Potapova, O., Iwasaki, A., and Pyle, A.M. (2018). A minimal RNA ligand for potent RIG-I activation in living mice. Sci. Adv. *4*.

Liu, G., Lee, J.-H., Parker, Z.M., Acharya, D., Chiang, J.J., van Gent, M., Riedl, W., Davis-Gardner, M.E., Wies, E., Chiang, C., et al. (2021). ISG15-dependent activation of the sensor MDA5 is antagonized by the SARS-CoV-2 papain-like protease to evade host innate immunity. Nat. Microbiol. *6*, 467–478.

Liu, J., Li, S., Liu, J., Liang, B., Wang, X., Wang, H., Li, W., Tong, Q., Yi, J., Zhao, L., et al. (2020). Longitudinal characteristics of lymphocyte responses and cytokine profiles in the peripheral blood of SARS-CoV-2 infected patients. EBioMedicine *55*, 102763.

Loetscher, M., Gerber, B., Loetscher, P., Jones, S.A., Piali, L., Clark-Lewis, I., Baggiolini, M., and Moser, B. (1996). Chemokine receptor specific for IP10 and mig: structure, function, and expression in activated T-lymphocytes. J. Exp. Med. *184*, 963–969.

Lokugamage, K.G., Hage, A., de Vries, M., Valero-Jimenez, A.M., Schindewolf, C., Dittmann, M., Rajsbaum, R., and Menachery, V.D. (2020). Type I Interferon Susceptibility Distinguishes SARS-CoV-2 from SARS-CoV. J. Virol. *94*.

Lokugamage, M.P., Vanover, D., Beyersdorf, J., Hatit, M.Z.C., Rotolo, L., Echeverri, E.S., Peck, H.E., Ni, H., Yoon, J.-K., Kim, Y., et al. (2021). Optimization of lipid nanoparticles for the delivery of nebulized therapeutic mRNA to the lungs. Nat. Biomed. Eng. *5*, 1059–1068.

Long, Q.-X., Liu, B.-Z., Deng, H.-J., Wu, G.-C., Deng, K., Chen, Y.-K., Liao, P., Qiu, J.-F., Lin, Y., Cai, X.-F., et al. (2020). Antibody responses to SARS-CoV-2 in patients with COVID-19. Nat. Med. *26*, 845–848.

Loo, Y.-M.Y.-M.Y.-M., Fornek, J., Crochet, N., Bajwa, G., Perwitasari, O., Martinez-Sobrido, L., Akira, S., Gill, M.A., Garcia-Sastre, A., Katze, M.G., et al. (2008). Distinct RIG-I and MDA5 Signaling by RNA Viruses in Innate Immunity. J. Virol. *82*, 335–345.

Lopez-Leon, S., Wegman-Ostrosky, T., Perelman, C., Sepulveda, R., Rebolledo, P.A., Cuapio, A., and Villapol, S. (2021). More than 50 long-term effects of COVID-19: a systematic review and meta-analysis. Sci. Rep. *11*, 16144.

Luo, D., Ding, S.C., Vela, A., Kohlway, A., Lindenbach, B.D., and Pyle, A.M. (2011). Structural Insights into RNA Recognition by RIG-I. Cell *147*, 409–422.

Mahase, E. (2021). Covid-19: Pfizer's paxlovid is 89% effective in patients at risk of serious illness, company reports. BMJ n2713.

Mao, T., Israelow, B., Lucas, C., Vogels, C.B.F., Gomez-Calvo, M.L., Fedorova, O., Breban, M.I., Menasche, B.L., Dong, H., Linehan, M., et al. (2022). A stem-loop RNA RIG-I agonist protects against acute and chronic SARS-CoV-2 infection in mice. J. Exp. Med. *219*.

Marcello, T., Grakoui, A., Barba–Spaeth, G., Machlin, E.S., Kotenko, S. V., Macdonald, M.R., and Rice, C.M. (2006). Interferons α and λ Inhibit Hepatitis C Virus Replication With

Distinct Signal Transduction and Gene Regulation Kinetics. Gastroenterology *131*, 1887–1898.

Marshak-Rothstein, A. (2006). Toll-like receptors in systemic autoimmune disease. Nat. Rev. Immunol. *6*, 823–835.

Matsuda, F., Torii, Y., Enomoto, H., Kuga, C., Aizawa, N., Iwata, Y., Saito, M., Imanishi, H., Shimomura, S., Nakamura, H., et al. (2012). Anti-interferon-α neutralizing antibody is associated with nonresponse to pegylated interferon-α plus ribavirin in chronic hepatitis C. J. Viral Hepat. *19*, 694–703.

McCray, P.B., Pewe, L., Wohlford-Lenane, C., Hickey, M., Manzel, L., Shi, L., Netland, J., Jia, H.P., Halabi, C., Sigmund, C.D., et al. (2007). Lethal Infection of K18-hACE2 Mice Infected with Severe Acute Respiratory Syndrome Coronavirus. J. Virol. *81*, 813–821.

Menachery, V.D., Debbink, K., and Baric, R.S. (2014). Coronavirus non-structural protein 16: Evasion, attenuation, and possible treatments. Virus Res. *194*, 191–199.

Meyerowitz-Katz, G., and Merone, L. (2020). A systematic review and meta-analysis of published research data on COVID-19 infection fatality rates. Int. J. Infect. Dis. *101*, 138–148.

Middleton, M.R., Wermke, M., Calvo, E., Chartash, E., Zhou, H., Zhao, X., Niewel, M., Dobrenkov, K., and Moreno, V. (2018). Phase I/II, multicenter, open-label study of intratumoral/intralesional administration of the retinoic acid–inducible gene I (RIG-I) activator MK-4621 in patients with advanced or recurrent tumors. Ann. Oncol. *29*, viii712.

Mistry, P., Barmania, F., Mellet, J., Peta, K., Strydom, A., Viljoen, I.M., James, W., Gordon, S., and Pepper, M.S. (2022). SARS-CoV-2 Variants, Vaccines, and Host Immunity. Front. Immunol. *12*.

Mulchandani, R., Lyngdoh, T., and Kakkar, A.K. (2021). Deciphering the COVID-19 cytokine storm: Systematic review and meta-analysis. Eur. J. Clin. Invest. *51*.

Muñoz-Fontela, C., Dowling, W.E., Funnell, S.G.P., Gsell, P.S., Riveros-Balta, A.X., Albrecht, R.A., Andersen, H., Baric, R.S., Carroll, M.W., Cavaleri, M., et al. (2020). Animal models for COVID-19. Nature *586*, 509–515.

Le Naour, J., Zitvogel, L., Galluzzi, L., Vacchelli, E., and Kroemer, G. (2020). Trial watch: STING agonists in cancer therapy. Oncoimmunology *9*.

Nyholm, S. V, and Graf, J. (2012). Knowing your friends: invertebrate innate immunity fosters beneficial bacterial symbioses. Nat. Rev. Microbiol. *10*, 815–827.

Oladunni, F.S., Park, J.G., Pino, P.A., Gonzalez, O., Akhter, A., Allué-Guardia, A., Olmo-Fontánez, A., Gautam, S., Garcia-Vilanova, A., Ye, C., et al. (2020). Lethality of SARS-CoV-2 infection in K18 human angiotensin-converting enzyme 2 transgenic mice. Nat. Commun. *11*.

Olagnier, D., Scholte, F.E.M., Chiang, C., Albulescu, I.C., Nichols, C., He, Z., Lin, R., Snijder, E.J., van Hemert, M.J., and Hiscott, J. (2014). Inhibition of Dengue and Chikungunya Virus Infections by RIG-I-Mediated Type I Interferon-Independent Stimulation of the Innate Antiviral Response. J. Virol. *88*, 4180–4194.

Pairo-Castineira, E., Clohisey, S., Klaric, L., Bretherick, A.D., Rawlik, K., Pasko, D., Walker, S., Parkinson, N., Fourman, M.H., Russell, C.D., et al. (2021). Genetic mechanisms of critical illness in COVID-19. Nature *591*, 92–98.

Pandit, A., Bhalani, N., Bhushan, B.L.S., Koradia, P., Gargiya, S., Bhomia, V., and Kansagra, K. (2021). Efficacy and safety of pegylated interferon alfa-2b in moderate COVID-19: A phase II, randomized, controlled, open-label study. Int. J. Infect. Dis. *105*, 516–521.

Paz, S., Sun, Q., Nakhaei, P., Romieu-Mourez, R., Goubau, D., Julkunen, I., Lin, R., and Hiscott, J. (2006). Induction of IRF-3 and IRF-7 phosphorylation following activation of the RIG-I pathway. Cell. Mol. Biol. (Noisy-Le-Grand). *52*, 17–28.

Peisley, A., Lin, C., Wu, B., Orme-Johnson, M., Liu, M., Walz, T., and Hur, S. (2011). Cooperative assembly and dynamic disassembly of MDA5 filaments for viral dsRNA recognition. Proc. Natl. Acad. Sci. *108*, 21010–21015.

Peisley, A., Jo, M.H., Lin, C., Wu, B., Orme-Johnson, M., Walz, T., Hohng, S., and Hur, S. (2012). Kinetic mechanism for viral dsRNA length discrimination by MDA5 filaments. Proc. Natl. Acad. Sci. *109*, E3340–E3349.

Perlman, S., and McCray, P.B. No Title.

Pichlmair, A., Schulz, O., Tan, C.P., Naslund, T.I., Liljestrom, P., Weber, F., and Reis e Sousa, C. (2006). RIG-I-Mediated Antiviral Responses to Single-Stranded RNA Bearing 5'-Phosphates. Science (80-.). *314*, 997–1001.

Pichlmair, A., Schulz, O., Tan, C.-P., Rehwinkel, J., Kato, H., Takeuchi, O., Akira, S., Way, M., Schiavo, G., and Reis e Sousa, C. (2009). Activation of MDA5 Requires Higher-Order RNA Structures Generated during Virus Infection. J. Virol. *83*, 10761–10769.

Poeck, H., Besch, R., Maihoefer, C., Renn, M., Tormo, D., Morskaya, S.S., Kirschnek, S., Gaffal, E., Landsberg, J., Hellmuth, J., et al. (2008). 5′-triphosphate-siRNA: turning gene silencing and Rig-I activation against melanoma. Nat. Med. *14*, 1256–1263.

Pothlichet, J., Burtey, A., Kubarenko, A. V., Caignard, G., Solhonne, B., Tangy, F., Ben-Ali, M., Quintana-Murci, L., Heinzmann, A., Chiche, J.-D., et al. (2009). Study of Human RIG-I Polymorphisms Identifies Two Variants with an Opposite Impact on the Antiviral Immune Response. PLoS One *4*, e7582.

Quicke, K.M., Kim, K.Y., Horvath, C.M., and Suthar, M.S. (2019). RNA Helicase LGP2 Negatively Regulates RIG-I Signaling by Preventing TRIM25-Mediated Caspase Activation and Recruitment Domain Ubiquitination. J. Interf. Cytokine Res. *39*, 669–683.

Rebendenne, A., Chaves Valadão, A.L., Tauziet, M., Maarifi, G., Bonaventure, B., McKellar, J., Planès, R., Nisole, S., Arnaud-Arnould, M., Moncorgé, O., et al. (2021). SARS-CoV-2 Triggers an MDA-5-Dependent Interferon Response Which Is Unable To Control Replication in Lung Epithelial Cells. J. Virol. *95*.

RECOVERY Collaborative Group, Horby, P., Lim, W.S., Emberson, J.R., Mafham, M., Bell, J.L., Linsell, L., Staplin, N., Brightling, C., Ustianowski, A., et al. (2021). Dexamethasone in Hospitalized Patients with Covid-19. N. Engl. J. Med. *384*, 693–704.

Rehwinkel, J., and Gack, M.U. (2020). RIG-I-like receptors: their regulation and roles in RNA sensing. Nat. Rev. Immunol. *20*, 537–551.

Renu, K., Prasanna, P.L., and Valsala Gopalakrishnan, A. (2020). Coronaviruses pathogenesis, comorbidities and multi-organ damage – A review. Life Sci. *255*, 117839.

Rodero, M.P., and Crow, Y.J. (2016). Type I interferon–mediated monogenic autoinflammation: The type I interferonopathies, a conceptual overview. J. Exp. Med. *213*, 2527–2538.

Rothenfusser, S., Goutagny, N., DiPerna, G., Gong, M., Monks, B.G., Schoenemeyer, A., Yamamoto, M., Akira, S., and Fitzgerald, K.A. (2005). The RNA helicase Lgp2 inhibits TLR-independent sensing of viral replication by retinoic acid-inducible gene-I. J. Immunol. *175*, 5260–5268.

Saban, M., Myers, V., and Wilf-Miron, R. (2022). Changes in infectivity, severity and vaccine effectiveness against delta COVID-19 variant ten months into the vaccination program: The Israeli case. Prev. Med. (Baltim). *154*, 106890.

Sah, P., Fitzpatrick, M.C., Zimmer, C.F., Abdollahi, E., Juden-Kelly, L., Moghadas, S.M., Singer, B.H., and Galvani, A.P. (2021). Asymptomatic SARS-CoV-2 infection: A systematic review and meta-analysis. Proc. Natl. Acad. Sci. *118*, e2109229118.

Saito, T., Hirai, R., Loo, Y.-M., Owen, D., Johnson, C.L., Sinha, S.C., Akira, S., Fujita, T., and Gale, M. (2007). Regulation of innate antiviral defenses through a shared repressor domain in RIG-I and LGP2. Proc. Natl. Acad. Sci. *104*, 582–587.

Sampaio, N.G., Chauveau, L., Hertzog, J., Bridgeman, A., Fowler, G., Moonen, J.P., Dupont, M., Russell, R.A., Noerenberg, M., and Rehwinkel, J. (2021). The RNA sensor MDA5 detects SARS-CoV-2 infection. Sci. Rep. *11*, 13638.

Sanchez-Ramirez, D.C., Normand, K., Zhaoyun, Y., and Torres-Castro, R. (2021). Long-Term Impact of COVID-19: A Systematic Review of the Literature and Meta-Analysis. Biomedicines *9*, 900.

Sansom, D.M. (2000). CD28, CTLA-4 and their ligands: who does what and to whom? Immunology *101*, 169–177.

Schlee, M., Roth, A., Hornung, V., Hagmann, C.A., Wimmenauer, V., Barchet, W., Coch, C., Janke, M., Mihailovic, A., Wardle, G., et al. (2009). Recognition of 5??? Triphosphate by RIG-I Helicase Requires Short Blunt Double-Stranded RNA as Contained in Panhandle of Negative-Strand Virus. Immunity *31*, 25–34.

Schneider, W.M., Chevillotte, M.D., and Rice, C.M. (2014). Interferon-stimulated genes: a complex web of host defenses. Annu. Rev. Immunol. *32*, 513–545.

Schuberth-Wagner, C., Ludwig, J., Bruder, A.K., Herzner, A.-M., Zillinger, T., Goldeck, M., Schmidt, T., Schmid-Burgk, J.L., Kerber, R., Wolter, S., et al. (2015). A Conserved Histidine in the RNA Sensor RIG-I Controls Immune Tolerance to N1-2′O-Methylated Self RNA. Immunity *43*, 41–51.

Seth, R.B., Sun, L., Ea, C.-K., and Chen, Z.J. (2005). Identification and Characterization of MAVS, a Mitochondrial Antiviral Signaling Protein that Activates NF-κB and IRF3. Cell *122*, 669–682.

Sharpe, A.H., Wherry, E.J., Ahmed, R., and Freeman, G.J. (2007). The function of programmed cell death 1 and its ligands in regulating autoimmunity and infection. Nat. Immunol. *8*, 239–245.

Shaw, R.J., Bradbury, C., Abrams, S.T., Wang, G., and Toh, C. (2021). COVID-19 and immunothrombosis: emerging understanding and clinical management. Br. J. Haematol. *194*, 518–529.

Sim, I.S., and Cerruti, R.L. (1987). Recombinant interferons alpha and gamma: comparative antiviral activity and synergistic interaction in encephalomyocarditis virus infection of mice. Antiviral Res. *8*, 209–221.

Sleijfer, S., Bannink, M., Gool, A.R., Kruit, W.H.J., and Stoter, G. (2005). Side Effects of Interferon-α Therapy. Pharm. World Sci. *27*, 423–431.

Snijder, E.J., Limpens, R.W.A.L., de Wilde, A.H., de Jong, A.W.M., Zevenhoven-Dobbe, J.C., Maier, H.J., Faas, F.F.G.A., Koster, A.J., and Bárcena, M. (2020). A unifying structural and functional model of the coronavirus replication organelle: Tracking down RNA synthesis. PLOS Biol. *18*, e3000715.

Song, E., Zhang, C., Israelow, B., Lu-Culligan, A., Prado, A.V., Skriabine, S., Lu, P., Weizman, O.-E., Liu, F., Dai, Y., et al. (2021). Neuroinvasion of SARS-CoV-2 in human and mouse brain. J. Exp. Med. *218*.

Spiropoulou, C.F., Ranjan, P., Pearce, M.B., Sealy, T.K., Albariño, C.G., Gangappa, S., Fujita, T., Rollin, P.E., Nichol, S.T., Ksiazek, T.G., et al. (2009). RIG-I activation inhibits ebolavirus replication. Virology *392*, 11–15.

Spudich, S., and Nath, A. (2022). Nervous system consequences of COVID-19. Science (80-.). *375*, 267–269.

Stacey, K.J., Young, G.R., Clark, F., Sester, D.P., Roberts, T.L., Naik, S., Sweet, M.J., and Hume, D.A. (2003). The Molecular Basis for the Lack of Immunostimulatory Activity of Vertebrate DNA. J. Immunol. *170*, 3614–3620.

Stanifer, M.L., Kee, C., Cortese, M., Zumaran, C.M., Triana, S., Mukenhirn, M., Kraeusslich, H.-G., Alexandrov, T., Bartenschlager, R., and Boulant, S. (2020). Critical Role of Type III Interferon in Controlling SARS-CoV-2 Infection in Human Intestinal Epithelial Cells. Cell Rep. *32*, 107863.

Stertz, S., Reichelt, M., Spiegel, M., Kuri, T., Martínez-Sobrido, L., García-Sastre, A., Weber, F., and Kochs, G. (2007). The intracellular sites of early replication and budding of SARS-coronavirus. Virology *361*, 304–315.

Streeck, H., Schulte, B., Kümmerer, B.M., Richter, E., Höller, T., Fuhrmann, C., Bartok, E., Dolscheid-Pommerich, R., Berger, M., Wessendorf, L., et al. (2020). Infection fatality rate of SARS-CoV2 in a super-spreading event in Germany. Nat. Commun. *11*, 5829.

Sun, F., Li, L., Xiao, Y., Gregory, A.D., Shapiro, S.D., Xiao, G., and Qu, Z. (2021). Alveolar Macrophages Inherently Express Programmed Death-1 Ligand 1 for Optimal Protective Immunity and Tolerance. J. Immunol. *207*, 110–114.

Sun, S.-H., Chen, Q., Gu, H.-J., Yang, G., Wang, Y.-X., Huang, X.-Y., Liu, S.-S., Zhang, N.-N., Li, X.-F., Xiong, R., et al. (2020). A Mouse Model of SARS-CoV-2 Infection and Pathogenesis. Cell Host Microbe *28*, 124-133.e4.

Takahasi, K., Kumeta, H., Tsuduki, N., Narita, R., Shigemoto, T., Hirai, R., Yoneyama, M., Horiuchi, M., Ogura, K., Fujita, T., et al. (2009). Solution Structures of Cytosolic RNA Sensor MDA5 and LGP2 C-terminal Domains. J. Biol. Chem. *284*, 17465–17474.

Thorne, L.G., Reuschl, A., Zuliani-Alvarez, L., Whelan, M.V.X., Turner, J., Noursadeghi, M., Jolly, C., and Towers, G.J. (2021a). SARS-CoV-2 sensing by RIG-I and MDA5 links epithelial infection to macrophage inflammation. EMBO J. *40*.

Thorne, L.G., Bouhaddou, M., Reuschl, A.-K., Zuliani-Alvarez, L., Polacco, B., Pelin, A., Batra, J., Whelan, M.V.X., Hosmillo, M., Fossati, A., et al. (2021b). Evolution of enhanced innate immune evasion by SARS-CoV-2. Nature.

Tian, S., Xiong, Y., Liu, H., Niu, L., Guo, J., Liao, M., and Xiao, S.-Y. (2020). Pathological study of the 2019 novel coronavirus disease (COVID-19) through postmortem core biopsies. Mod. Pathol. *33*, 1007–1014.

Tisoncik, J.R., Korth, M.J., Simmons, C.P., Farrar, J., Martin, T.R., and Katze, M.G. (2012). Into the Eye of the Cytokine Storm. Microbiol. Mol. Biol. Rev. *76*, 16–32.

Tolksdorf, B., Nie, C., Niemeyer, D., Röhrs, V., Berg, J., Lauster, D., Adler, J.M., Haag, R., Trimpert, J., Kaufer, B., et al. (2021). Inhibition of SARS-CoV-2 Replication by a Small Interfering RNA Targeting the Leader Sequence. Viruses *13*, 2030.

Uchikawa, E., Lethier, M., Malet, H., Brunel, J., Gerlier, D., and Cusack, S. (2016). Structural Analysis of dsRNA Binding to Anti-viral Pattern Recognition Receptors LGP2 and MDA5. Mol. Cell *62*, 586–602.

Vénéreau, E., Ceriotti, C., and Bianchi, M.E. (2015). DAMPs from Cell Death to New Life. Front. Immunol. *6*.

Venkataraman, T., Valdes, M., Elsby, R., Kakuta, S., Caceres, G., Saijo, S., Iwakura, Y., and Barber, G.N. (2007). Loss of DExD/H Box RNA Helicase LGP2 Manifests Disparate Antiviral Responses. J. Immunol. *178*, 6444–6455.

Vivier, E., Tomasello, E., Baratin, M., Walzer, T., and Ugolini, S. (2008). Functions of natural killer cells. Nat. Immunol. *9*, 503–510.

Wang, N., Zhan, Y., Zhu, L., Hou, Z., Liu, F., Song, P., Qiu, F., Wang, X., Zou, X., Wan, D., et al. (2020a). Retrospective Multicenter Cohort Study Shows Early Interferon Therapy Is Associated with Favorable Clinical Responses in COVID-19 Patients. Cell Host Microbe *28*, 455-464.e2.

Wang, Y., Ludwig, J., Schuberth, C., Goldeck, M., Schlee, M., Li, H., Juranek, S., Sheng, G., Micura, R., Tuschl, T., et al. (2010). Structural and functional insights into 5′-ppp RNA pattern recognition by the innate immune receptor RIG-I. Nat. Struct. Mol. Biol. *17*, 781–787.

Wang, Y., Grunewald, M., and Perlman, S. (2020b). Coronaviruses: An Updated Overview of Their Replication and Pathogenesis. pp. 1–29.

Ward, S.G., Bacon, K., and Westwick, J. (1998). Chemokines and T Lymphocytes. Immunity *9*, 1–11.

Weerd, N.A., and Nguyen, T. (2012). The interferons and their receptors—distribution and regulation. Immunol. Cell Biol. *90*, 483–491.

Wendisch, D., Dietrich, O., Mari, T., von Stillfried, S., Ibarra, I.L., Mittermaier, M., Mache, C., Chua, R.L., Knoll, R., Timm, S., et al. (2021). SARS-CoV-2 infection triggers profibrotic macrophage responses and lung fibrosis. Cell *184*, 6243-6261.e27.

Winkler, E.S., Bailey, A.L., Kafai, N.M., Nair, S., McCune, B.T., Yu, J., Fox, J.M., Chen, R.E., Earnest, J.T., Keeler, S.P., et al. (2020). SARS-CoV-2 infection of human ACE2-transgenic mice causes severe lung inflammation and impaired function. Nat. Immunol. *21*, 1327–1335.

Winkler, E.S., Chen, R.E., Alam, F., Yildiz, S., Case, J.B., Uccellini, M.B., Holtzman, M.J., Garcia-Sastre, A., Schotsaert, M., and Diamond, M.S. (2021). SARS-CoV-2 causes lung infection without severe disease in human ACE2 knock-in mice. J. Virol.

Wu, Z., and McGoogan, J.M. (2020). Characteristics of and Important Lessons From the Coronavirus Disease 2019 (COVID-19) Outbreak in China. JAMA *323*, 1239.

Wu, B., Peisley, A., Richards, C., Yao, H., Zeng, X., Lin, C., Chu, F., Walz, T., and Hur, S. (2013). Structural Basis for dsRNA Recognition, Filament Formation, and Antiviral Signal Activation by MDA5. Cell *152*, 276–289.

Xu, Z., Shi, L., Wang, Y., Zhang, J., Huang, L., Zhang, C., Liu, S., Zhao, P., Liu, H., Zhu, L., et al. (2020). Pathological findings of COVID-19 associated with acute respiratory distress syndrome. Lancet Respir. Med. *8*, 420–422.

Yin, X., Riva, L., Pu, Y., Martin-Sancho, L., Kanamune, J., Yamamoto, Y., Sakai, K., Gotoh, S., Miorin, L., De Jesus, P.D., et al. (2021). MDA5 Governs the Innate Immune Response to SARS-CoV-2 in Lung Epithelial Cells. Cell Rep. *34*, 108628.

Yinda, C.K., Port, J.R., Bushmaker, T., Offei Owusu, I., Purushotham, J.N., Avanzato, V.A., Fischer, R.J., Schulz, J.E., Holbrook, M.G., Hebner, M.J., et al. (2021). K18-hACE2 mice develop respiratory disease resembling severe COVID-19. PLOS Pathog. *17*, e1009195.

Yoneyama, M., Kikuchi, M., Natsukawa, T., Shinobu, N., Imaizumi, T., Miyagishi, M., Taira, K., Akira, S., and Fujita, T. (2004). The RNA helicase RIG-I has an essential function in double-stranded RNA-induced innate antiviral responses. Nat. Immunol. *5*, 730–737.

Yoneyama, M., Kikuchi, M., Matsumoto, K., Imaizumi, T., Miyagishi, M., Taira, K., Foy, E., Loo, Y.-M., Gale, M., Akira, S., et al. (2005). Shared and Unique Functions of the DExD/H-Box Helicases RIG-I, MDA5, and LGP2 in Antiviral Innate Immunity. J. Immunol. *175*, 2851–2858.

Yong, H.Y., and Luo, D. (2018a). RIG-I-Like Receptors as Novel Targets for Pan-Antivirals and Vaccine Adjuvants Against Emerging and Re-Emerging Viral Infections. Front. Immunol. *9*.

Yong, H.Y., and Luo, D. (2018b). RiG-i-Like Receptors as novel Targets for Pan-Antivirals and vaccine Adjuvants Against emerging and Re-emerging viral infections. *9*, 1–9.

Zaki, A.M., van Boheemen, S., Bestebroer, T.M., Osterhaus, A.D.M.E., and Fouchier, R.A.M. (2012). Isolation of a Novel Coronavirus from a Man with Pneumonia in Saudi Arabia. N. Engl. J. Med. *367*, 1814–1820.

Zhang, B., Zhou, X., Zhu, C., Song, Y., Feng, F., Qiu, Y., Feng, J., Jia, Q., Song, Q., Zhu, B., et al. (2020a). Immune Phenotyping Based on the Neutrophil-to-Lymphocyte Ratio and IgG Level Predicts Disease Severity and Outcome for Patients With COVID-19. Front. Mol. Biosci. *7*.

Zhang, Q., Bastard, P., Liu, Z., Le Pen, J., Moncada-Velez, M., Chen, J., Ogishi, M., Sabli, I.K.D., Hodeib, S., Korol, C., et al. (2020b). Inborn errors of type I IFN immunity in patients with life-threatening COVID-19. Science (80-.). *370*, eabd4570.

Zheng, J., Wong, L.Y.R., Li, K., Verma, A.K., Ortiz, M.E., Wohlford-Lenane, C., Leidinger, M.R., Knudson, C.M., Meyerholz, D.K., McCray, P.B., et al. (2021). COVID-19 treatments and pathogenesis including anosmia in K18-hACE2 mice. Nature *589*, 603–607.

Zhou, B., Thao, T.T.N., Hoffmann, D., Taddeo, A., Ebert, N., Labroussaa, F., Pohlmann, A., King, J., Steiner, S., Kelly, J.N., et al. (2021). SARS-CoV-2 spike D614G change enhances replication and transmission. Nature *592*, 122–127.

Zhou, F., Yu, T., Du, R., Fan, G., Liu, Y., Liu, Z., Xiang, J., Wang, Y., Song, B., Gu, X., et al. (2020a). Clinical course and risk factors for mortality of adult inpatients with COVID-19 in Wuhan, China: a retrospective cohort study. Lancet *395*, 1054–1062.

Zhou, P., Yang, X.-L., Wang, X.-G., Hu, B., Zhang, L., Zhang, W., Si, H.-R., Zhu, Y., Li, B., Huang, C.-L., et al. (2020b). A pneumonia outbreak associated with a new coronavirus of probable bat origin. Nature *579*, 270–273.

Zhou, Q., Chen, V., Shannon, C.P., Wei, X.-S., Xiang, X., Wang, X., Wang, Z.-H., Tebbutt, S.J., Kollmann, T.R., and Fish, E.N. (2020c). Interferon-α2b Treatment for COVID-19. Front. Immunol. *11*.

Zhou, Z., Hamming, O.J., Ank, N., Paludan, S.R., Nielsen, A.L., and Hartmann, R. (2007). Type III Interferon (IFN) Induces a Type I IFN-Like Response in a Restricted Subset of Cells through Signaling Pathways Involving both the Jak-STAT Pathway and the Mitogen-Activated Protein Kinases. J. Virol. *81*, 7749–7758.